8-12-2016

A New Framework Based on a Discrete Element Method to Model the Fracture Behavior for Brittle Polycrystalline Materials

Katerine Saleme Ruize

A new framework based on a discrete element method to model the fracture behavior for brittle polycrystalline materials

By

Katerine Saleme Ruiz

A Dissertation
Submitted to the Faculty of
Mississippi State University
in Partial Fulfillment of the Requirements
for the Degree of Doctor of Philosophy
in Computational Engineering
in the Bagley College of Engineering

Mississippi State, Mississippi

August 2016

A new framework based on a discrete element method to model the fracture behavior for brittle polycrystalline materials

By

Katerine Saleme Ruiz

Approved:

Tonya W. Stone
(Major Professor)

Ioana Banicescu
(Minor Professor)

John F. Peters
(Committee Member)

Hyeona Lim
(Committee Member)

Laura E. Walizer
(Committee Member)

Pasquale Cinnella
(Graduate Coordinator)

Jason M. Keith
Dean
Bagley College of Engineering

Name: Katerine Saleme Ruiz

Date of Degree: August 12, 2016

Institution: Mississippi State University

Major Field: Computational Engineering

Major Professor: Tonya W. Stone

Title of Study: A new framework based on a discrete element method to model the fracture behavior for brittle polycrystalline materials

Pages of Study: 153

Candidate for Degree of Doctor of Philosophy

This work aims to develop and implement a linear elastic grain-level micromechanical model based on the discrete element method using bonded contacts and an improved fracture criteria to capture both intergranular and transgranular microcrack initiation and evolution in polycrystalline ceramics materials. Gaining a better understanding of the underlying mechanics and micromechanics of the fracture process of brittle polycrystalline materials will aid in high performance material design. Continuum mechanics approaches cannot accurately simulate the crack propagation during fracture due to the discontinuous nature of the problem. In this work we distinguish between predominately intergranular failure (along the grain boundaries) versus predominately transgranular failure (across the grains) based on grain orientation and microstructural parameters to describe the contact interfaces and present the first approach at fracturing discrete elements. Specifically, the influence of grain boundary strength and stiffness on the fracture behavior of an idealized ceramic material is studied under three different loading conditions: uniaxial compression,

brazilian, and four-point bending. Digital representations of the sample microstructures for the test cases are composed of hexagonal, prismatic, honeycomb-packed grains represented by rigid, discrete elements. The principle of virtual work is used to develop a microscale fracture criteria for brittle polycrystalline materials for tensile, shear, torsional and rolling modes of intergranular motion. The interactions between discrete elements within each grain are governed by traction displacement relationships.

Key words: Polycrystalline ceramics, discrete element method, digital microstructure representation, fracture modeling, virtual work

DEDICATION

This dissertation is dedicated to my dad Pedro Salcedo, the most generous, honest and hard-working man I have known.

Dad you gave me the greatest gift anyone could give: you loved me and believed in me. Your memories are my heartbeats, I think of you all the time and I miss you so much... You stayed strong and never give up, I promise you I will do the same no matter what.

ACKNOWLEDGEMENTS

Firstly, I would like to express my sincere gratitude to my advisor Dr. Tonya W. Stone for her continuous support during my Ph.D study, for her guidance, patience, encouragement and for helping me grow stronger as a professional and as a person.

I would like to express my deepest gratitude to Dr. John F. Peters for his guidance, energetic knowledge transfer and steady willingness to discuss with me numerous aspects of my research and life.

I thank my committee for their insightful comments on this dissertation and professional advices. Special thanks to Dr. Wayne Hodo for his support during my internship at The U.S. Army Corps of Engineers Engineer Research and Development Center (USACE-ERDC). I thank the Center for Advanced Vehicular Systems, the Malcolm A. Portera High Performance Computing Center and USACE-ERDC for the financial support and the great scientific environment which contributed to the success of this dissertation.

I thank my family and the wonderful friends I have made here in Mississippi, for giving many amazing times, for loving me even when I was difficult to be loved and supporting me when I needed the most.

Finally, I would like to thank my husband Maurin for loving me for all that I am and all that I am not, and standing by my side through it all.

Muchas gracias!

TABLE OF CONTENTS

LIST OF TABLES

LIST OF FIGURES

CHAPTER 1

INTRODUCTION

1.1 Background

In this introductory chapter, an overview of brittle polycrystalline materials is presented. The fundamental equations relating stress, strain, and displacements to describe the mechanical response of solid body is briefly reviewed. Brittle fracture behavior and relevant fracture criterion are reviewed in detail herein. An overview on the current state of development of discrete element methods, specifically in the fracture of brittle materials is discussed. Lastly, the motivation and objectives of the proposed research is presented, followed by a description of the organization of the remaining chapters of the research study.

1.1.1 Brittle Polycrystalline Materials

Polycrystalline materials, such as metals and ceramics, are the most widely used group of structural materials in today's manufacturing industry [99]. Polycrystalline brittle materials manufactured from oxides, from refractory compounds of the carbide class, and from nitrates and silicides, are a large group of materials used extensively in modern technology, and their strength properties have been studied at length [19, 25, 72, 89, 105, 111]. A polycrystalline microstructure is composed of many irregular-shaped crystallites of diffe-

rent sizes and orientations, called *grains*, separated by interfaces, called *grain boundaries*, as shown in Figure 1.1. Grain boundaries are important elements associated with microstructural heterogeneity in polycrystalline materials. These boundaries strongly affect bulk properties, particularly mechanical properties controlled by deformation and fracture in polycrystalline materials. Both beneficial [34, 53] and detrimental [64, 85] effects of grain boundaries on mechanical properties have been observed. In polycrystalline materials, grain boundaries can aid in the resistance of crack propagation. It is well known that grain refinement, i.e. an increase in the density of grain boundaries with decreased grain size, can improve in the strength of polycrystals, as predicted by the Hall-Petch relationship [39]. However grain boundaries can also weaken the overall strength of the parent material due to reduced material properties and differences in interfacial properties. Because grain boundaries can be preferential sites for crack nucleation and propagation, intergranular fracture is often the primary origin of severe brittleness of polycrystalline materials [101]. Therefore the engineering properties of polycrystalline materials are determined as much by the connectivity and interaction among crystalline grains as by the strength of the grains[28].

A material is characterized as brittle if it experiences little to no plastic deformation when subjected to stresses that lead to fracture. Brittle materials absorb minimal energy prior to fracture and typically have a rather small fracture strain of less than 0.05. Therefore brittle materials generally have higher strength but lower toughness than their ductile counterparts. Having a better understanding of the mechanical behavior and failure mecha-

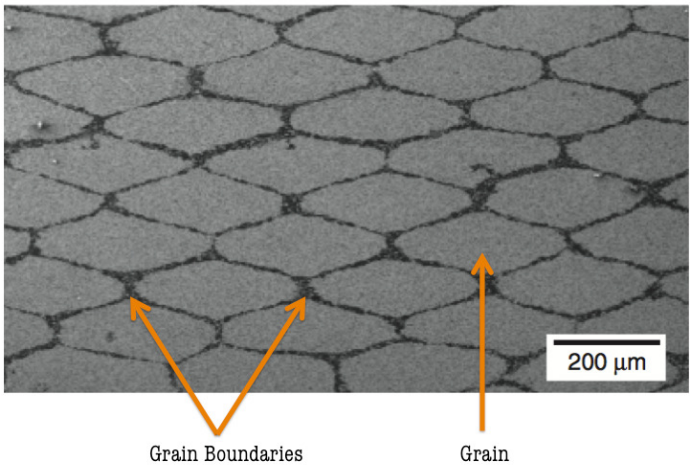

Figure 1.1

Illustration of the grain and grain boundaries in fibrous monolith architecture consisting of ZrB2-30%SiC cells (light) and graphite-15%ZrB2 cell boundaries (dark) produced using coextrusion processing. Reprinted from [111]

nisms in brittle polycrystalline materials and accurately predicting their fracture behavior will aid in the development of advanced structural materials [92].

1.1.2 Theory of Elasticity

The theory of elasticity is a branch of continuum mechanics related to elastic solids and is concerned with the determination of the stresses and displacements in a solid body as a result of external loads for which the body reverts to its original state upon removal of the load. When solving any problem in solid mechanics several factors are considered: [86]:

- The Newtonian equations of motion and the related concept of stress
- Geometry of the deformation and thus expression of strains in terms of gradients in displacements fields
- Relations between stress and strain that are characteristic of the material in question, the stress level, temperature and time scales of the problem considered

- Equations for conservation of mass of diffusing constituents
- The first law of thermodynamics, which relates changes in energy to work and heat supply

From the above considerations, three fundamental relations arise for providing a mathematical description of the deformation of a solid body:

- The *equilibrium equations* which relate stress to the applied tractions on loaded boundaries and also govern the relations among stress gradient within the material
- The *kinematic equations* which relate strain to displacement gradients
- The *constitutive equations* which relates stress (or stress increment) to strain (or strain increment)

In the current work, we consider only the case of linear elastic theory which models reversible behavior of a material that is subjected to small strains. In the majority of practical applications, the displacement of the solid is small, in which case the governing equations can be linearized. The fundamental relations are therefore presented in the context of the Small Displacement Theory of Elasticity in which the displacement components u, v, w, of the material particles are assumed to be much smaller (indeed, infinitesimally smaller) than any relevant dimension of the body. By using this approach, it can be assumed that the body's geometry and the constitutive properties of the material (such as stiffness) at each point of space are unchanged by the deformation. Rectangular Cartesian coordinates (x, y, z) are employed for defining the three dimensional (3D) space containing the body.

The linearized governing equations that arise from the three fundamental relations, Equilibrium, Kinematics, and Constitutive, are reviewed below. The effect of the mechanical properties of a material, such as its yield strength, Young's modulus, ultimate

strength, and fracture toughness on its susceptibility to failure modes are also predicted. These methodologies can be used to predict the response of these materials under loading.

1.1.2.1 Equilibrium: Stress Relations

Consider a body subjected to external forces on its surface. As a consequence of these external forces, internal forces are generated. If the body is cut along a plane perpendicular to the x axis, a continuous distribution of internal forces acts on the exposed surface to maintain equilibrium. If we consider the internal force $\vec{F}$ acting on an infinitesimally small area, the stresses at this point are given by

$$\sigma_{ij} = \lim_{\Delta A_i} \left(\frac{\Delta F_j}{\Delta A_i} \right) \tag{1.1}$$

Here σ_{ij} is a second rank tensor with nine different components, that results in three normal stresses and six shear stresses.

$$\sigma_{ij} = \begin{pmatrix} \sigma_{11} & \sigma_{12} & \sigma_{13} \\ \sigma_{21} & \sigma_{22} & \sigma_{23} \\ \sigma_{31} & \sigma_{32} & \sigma_{33} \end{pmatrix} = \begin{pmatrix} \sigma_{xx} & \sigma_{xy} & \sigma_{xz} \\ \sigma_{yx} & \sigma_{yy} & \sigma_{yz} \\ \sigma_{zx} & \sigma_{zy} & \sigma_{zz} \end{pmatrix} \tag{1.2}$$

If a parallel plane were passed through the body an infinitesimal distance away, a thin slice would result. If an additional two pairs of planes were passed normal to the first pair, an infinitesimal cube representing a point would be isolated from the body. The stresses acting at the point would be as shown in Figure 1.2. On a face whose normal is in the positive direction of a coordinate axis, the stress component is positive when it points to the positive direction of the axis. On a face whose normal is in the negative direction of a

coordinate axis, the stress component is positive when it points to the negative direction of the axis.

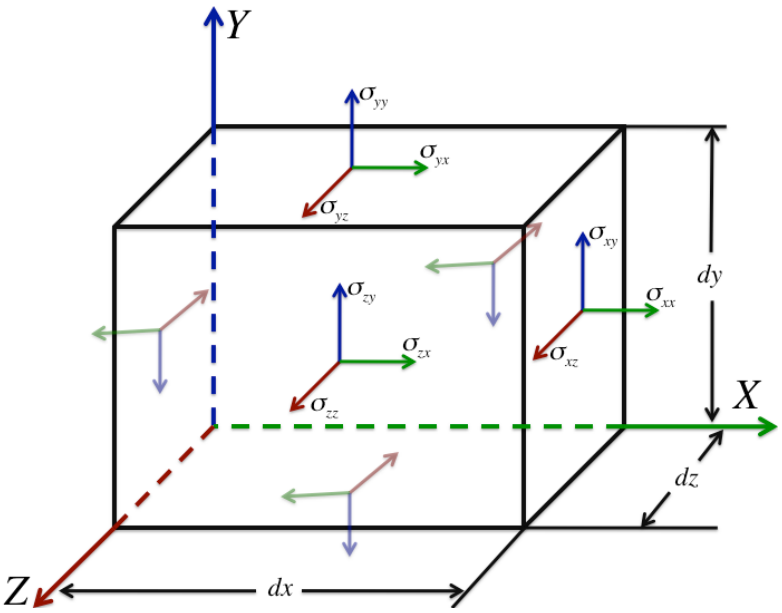

Figure 1.2

Stress element showing all nine component of a stress tensor

In general, the state of stress varies from point to point in a body. When a point is represented as an infinitesimal cube, the stress components will vary from one face to the other. This variation is given by the total differential,

$$d\sigma_{ij} = \frac{\partial \sigma_{ij}}{\partial x} dx + \frac{\partial \sigma_{ij}}{\partial y} dy + \frac{\partial \sigma_{ij}}{\partial z} dz \tag{1.3}$$

The internal forces and moments acting on the cube faces should satisfy the equations of equilibrium $\left(\sum F = 0\right)$:

$$\begin{aligned}
\frac{\partial \sigma_x}{\partial x} + \frac{\partial \tau_{yx}}{\partial y} + \frac{\partial \tau_{zx}}{\partial z} + F_x = 0, \\
\frac{\partial \tau_{xy}}{\partial x} + \frac{\partial \sigma_y}{\partial y} + \frac{\partial \tau_{zy}}{\partial z} + F_y = 0, \\
\frac{\partial \tau_{xz}}{\partial x} + \frac{\partial \tau_{yz}}{\partial y} + \frac{\partial \sigma_z}{\partial z} + F_z = 0,
\end{aligned} \tag{1.4}$$

and

$$\tau_{yz} = \tau_{zy}, \quad \tau_{zx} = \tau_{xz}, \quad \tau_{xy} = \tau_{yx},$$

where F_x, F_y and F_z are components of the body forces per unit volume. Summation of the moments results in $\sigma_{xy} = \sigma_{yx}$, $\sigma_{xz} = \sigma_{zx}$, $\sigma_{zy} = \sigma_{yz}$. Therefore only six independent stress components are needed to describe the state of stress of a material point because the stress tensor is symmetric.

1.1.2.2 Kinematics: Strain-Displacement Relations

Previously we have reviewed the stresses within a body subjected to external forces. Now we will examine the deformations caused by these forces and their intensity called strain. Deformations and strains are related to the changes in the size and shape of a body. When the relative position of any two points in a continuous body is changed the body is said to be deformed or strained. The analysis of strain is essentially a geometric problem and is unrelated to material properties.

The magnitude and direction of the displacement of a point in a body are denoted by u, v, and w in the x, y, and z directions in a rectangular coordinate system. The displacement of every point within the body constitutes the displacement field, $u = u(x, y, z)$, $v = v(x, y, z)$, and $w = w(x, y, z)$. Assuming small displacement theory, the strains pro-

duced due to these deformations are small compared to unity and their products (higher order terms) are neglected. The kinematic or strain-displacement equations describe how the strains - the stretching and distortion - within a loaded body relate to the body's displacements. If all points within the material experience the same displacement (u = constant), the structure moves as a rigid body but does not stretch or deform internally. For stretching to occur, points within the body must experience different displacements.

For a body in the 3D space, the strain state of a material particle is described by a total of six components (3 normal and 3 shear): $(\varepsilon_x, \varepsilon_y, \varepsilon_z, \gamma_{yz}, \gamma_{zx}, \gamma_{xy})$. The normal strains represent the unit elongation of a vector originally aligned with the x-axis, y-axis, or z-axis. The shear strain, ε, is the average of two rotational strains and is related to the engineering shear strain, γ, as $\varepsilon_{xy} = \frac{1}{2}\gamma_{xy}$. Thus, in small displacement theory, the strain-displacement relations may be written as,

$$\begin{aligned} &\varepsilon_x = \frac{\partial u}{\partial x}, \quad \varepsilon_y = \frac{\partial v}{\partial y}, \quad \varepsilon_z = \frac{\partial w}{\partial z} \\ &\gamma_{yz} = \frac{\partial w}{\partial y} + \frac{\partial v}{\partial z}, \quad \gamma_{zx} = \frac{\partial u}{\partial z} + \frac{\partial w}{\partial x}, \quad \gamma_{xy} = \frac{\partial v}{\partial x} + \frac{\partial u}{\partial y} \end{aligned} \tag{1.5}$$

1.1.2.3 Constitutive: Stress-Strain Relations

The previously reviewed concepts of stress and strain at a point involved no consideration of material type on behavior. To establish relationships between stress at a point and the corresponding strain at that point, material behavior considerations must be introduced. A linear elastic material exhibits stress components which are linear functions of the strain components. The material is elastic in that the removal of stress results in a return to the original shape, with no strain. Thus a state of zero stress always corresponds to a state of

zero strains. In the most general case, if we assume that the stresses are linearly related to the strains based on Hooke's Law, the stress-strain relationship (constitutive law) for an anisotropic, elastic homogeneous material can be written as,

$$\begin{pmatrix} \sigma_x \\ \sigma_y \\ \sigma_z \\ \tau_{yz} \\ \tau_{zx} \\ \tau_{xy} \end{pmatrix} = \begin{pmatrix} a_{11} & a_{12} & a_{13} & a_{14} & a_{15} & a_{16} \\ a_{21} & a_{22} & a_{23} & a_{24} & a_{25} & a_{26} \\ a_{31} & a_{32} & a_{33} & a_{34} & a_{35} & a_{36} \\ a_{41} & a_{42} & a_{43} & a_{44} & a_{45} & a_{46} \\ a_{51} & a_{52} & a_{53} & a_{54} & a_{55} & a_{56} \\ a_{61} & a_{62} & a_{63} & a_{64} & a_{65} & a_{66} \end{pmatrix} \begin{pmatrix} \varepsilon_x \\ \varepsilon_y \\ \varepsilon_z \\ \gamma_{yz} \\ \gamma_{zx} \\ \gamma_{xy} \end{pmatrix} \tag{1.6}$$

The coefficients of this equations are called elastic constants. Due to symmetry, there are only 21 independent elastic constants where,

$$a_{rs} = a_{sr}, \quad r, s = 1, ..., 6$$

The fundamental relations presented above are the mathematical descriptions of stress and strain. With the concepts of stress and strain established, the general types of mechanical behavior of solids can be described and thus quantitative treatments (possible by the use of the principle of virtual work) for particular problems of interest can be made. When a solid is subjected to an applied stress, it responds by deforming and if the stress exceeds the strength it responds by failing [96]. The types of mechanical behavior are defined by the modes of deformation and modes of failure and they are explained in the subsequent sections.

1.1.2.4 Principle of Virtual Work

In 3D, the mechanics of a body in equilibrium under prescribed body forces and boundary conditions is described by fifteen variables (three displacements, six strains, and six stresses) and a total of fifteen equations (six kinematic, three equilibrium, and six constitutive relations). The work of a force on a particle along a virtual displacement is known as the virtual work. The principle of virtual work for solving the above mentioned fifteen equations states that: *The virtual work done by the external forces of a mechanical system balances the virtual work done by the internal forces for any virtual displacements satisfying the essential (kinematic) boundary conditions* [74].

Consider a body composed of an infinite number of differential cubes subjected to internal stresses σ_{ij} and body forces $\vec{F}$ and continuous arbitrary displacements δu_i and consistent strains, ε_{ij}. Mathematically, the principle of virtual work is translated into:

$$\int_S \sigma_{ij} n_j \delta u_i dS + \int_V F_i \delta u_i dV = \int_V \sigma_{ij} \delta \varepsilon_{ij} dV \tag{1.7}$$

The principle of virtual work is one mathematical form in which a mechanical problem can be described. This form has the advantage that it directly gives the formulation needed for numerical computations such as the discrete element method. It gives a unified approach and understanding to apparently different engineering problems and it only involves the first order derivatives of the functions u_i and δu_i [74].

1.1.3 Brittle Fracture Behavior

Brittle fracture crosses the boundaries between material science, structural engineering, physics and chemistry. The term fracture mechanics refers to a vital specialization within

solid mechanics in which the presence of a crack is assumed, and quantitative relations need to be determined between the crack length, the material's inherent resistance to crack growth, and the stress at which the crack propagates at high speed to cause structural failure [87].

In brittle polycrystalline materials microstructure plays a significant role in dictating the modes of fracture and the macroscopic response. These phenomena are very sensitive to the polycrystalline microstructure [9, 4, 24], and therefore require a detailed investigation regarding the effect of microstructure on the fracture of brittle materials. Two main types of fracture are observed in the failure of brittle polycrystalline materials: intergranular, occurring along the grain boundaries as shown in Figure 1.3a) and transgranular, occurring through the grains as shown in Figure 1.3b), [101].

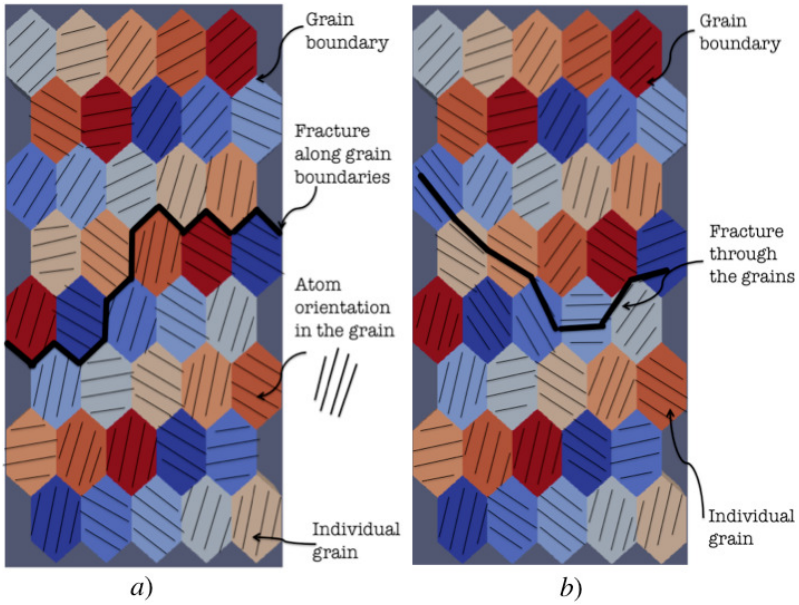

Figure 1.3

Schematic of a) Intergranular fracture and b) Transgranular fracture

Initial studies on brittle fracture can be traced back to Inglis [49] and Griffith [35]. Inglis initiated the concept of stress concentration at a void in a material and Griffith postulated that brittle failure in glass is a result of the growth of small cracks when the material is subjected to a large enough tensile stress [31]. The Griffith theory provides the basis for laws governing brittle fracture under triaxial stress conditions. Lajtai et. al. stated that the Griffith theory, or at least its basic premise that fracture starts from flaws, is fundamental to all investigations of brittle fracture, [98]. A sound fracture model should be established from knowledge of observed fracture behavior and based on both a stress and an energy criterion, [98].

The material microstructure plays a significant role in dictating the modes of fracture and the macroscopic response in brittle polycrystalline materials. Over the past few decades, considerable effort has been directed towards the micromechanics study of fracture that relates macroscale material properties, such as fracture toughness, to the underlying mechanisms, such as atomic bond breaking during crack propagations and grain effects that reduce strain energy through crack deflection and grain boundary motions [3, 15, 29, 30, 54, 108]. Fracture is a dissipative process in which elastic energy is dissipated to break bonds.

1.1.3.1 Griffith Energy-Balance Criterion

One approach used to predict model fracture initiation in brittle materials is the Griffith Criterion which states that the energy release rate, G, which is the elastic energy released per unit of crack advance must be equal or larger than the energy necessary to create new

surfaces (energy to break bonds = surface energy). The basic deformation mechanism in brittle materials is crack extension. Once nucleated, crack in brittle materials spread rapidly. The toughness of intrinsically brittle polycrystalline materials (such as metals like molybdenum and ceramics) increases systematically with increasing fraction of low-energy strong boundaries.

The energy approach states that crack extension (i.e., fracture) occurs when the energy available for crack growth is sufficient to overcome the resistance of the material [35]. The material resistance may include the surface energy, plastic work, or other types of energy dissipation associated with a propagating crack [6]. The total energy of the system, $U = U_M + U_S$, consists of two terms: U_M the mechanical energy composed of the strain potential energy stored in the elastic medium and the potential energy of the outer loading system; and U_S, the free energy expended in creating new crack surfaces.

The Griffith energy-balance criterion for predicting the fracture behavior of a body, firmly rooted in the laws of energy conservation, is given by the equilibrium requirements,

$$\frac{dU}{dc} = 0, \tag{1.8}$$

where dc is the virtual crack extension as shown in the schematic in Figure 1.4. A crack would extend or retract reversibly for small displacements from the equilibrium length, according to whether the left-hand side of Equation (1.8) is negative or positive.

The Griffith equilibrium equation can be rewritten in the form

$$\sigma_f = \sqrt{\frac{EG_c}{\pi c}}, \tag{1.9}$$

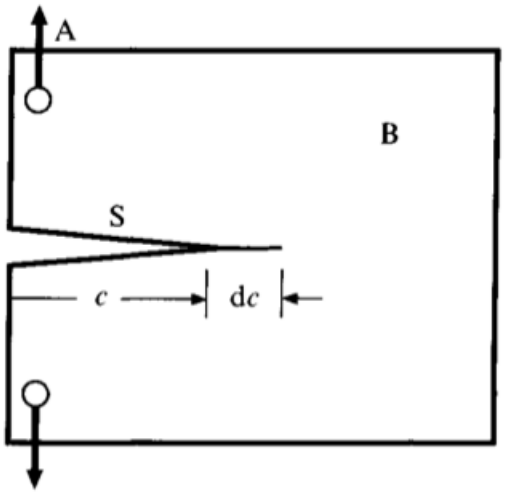

Figure 1.4

Static plane-crack system, showing incremental extension of crack length c through dc: B, elastic body; S, crack surface; A, applied loading, Reprinted from [61]

where G_c is the critical strain energy release rate and E is the Young's modulus. Equation (1.9) describes the interrelation between three important aspects of the fracture process:

- **the material** as evidenced in the critical strain energy release rate G_c
- **the stress level** σ_f
- **the size** c of the flaw

The value of c is chosen based on the smallest crack that could be easily detected.

The Griffith energy-balance approach provides meaningful insights to the fracture process. Analyses of crack tip stress field for material models other than purely linear elastic behavior were studied by Rice [71] who proposed the *J*-integral, a key innovative approach that can be used as an analytical tool to characterize the crack tip stress and strain field under both elastic and plastic stress and strain. An alternative but equivalent approach to the

Griffith approach, based on the stress state near the tip of a sharp crack, is more useful in engineering practice and is explained in the next section.

1.1.3.2 Stress Intensity Criterion

Near the tip of a crack in an elastic material, each stress component is proportional to a single constant, K_I, called *the stress intensity factor*. The I subscript is used to denote the crack opening mode: Mode I is normal opening mode, Mode II and III are shear sliding and tearing modes respectively. The different fracture modes produce different stress distributions in the material ahead of the crack tip, the intensity of which are governed by the stress intensity factors K_I, K_{II} and K_{III}. The stress intensity factors depend only on the applied loading and the crack geometry. The stress intensity factors are defined without recourse to any fracture criterion. Since the principle of superposition applies to linear stresses and displacements, the stress intensity factors for a given mode are additive. Also, because they uniquely characterize the level of loading in the region near the crack tip, the K parameters are intimately related to the conditions of crack extension [61].

If the material is assumed to fail locally at some critical combination of stress and strain, then it follows that the fracture occur at a critical stress intensity K_{IC}. The *critical normal stress criterion* states that failure occurs when $K_I = K_{IC}$ and thus consider failure to be solely by mode I loading of a crack. In this case, K_I is the driving force for fracture and K_{IC} is a measure of material resistance, called *Fracture Toughness*. These stress intensity factors are used in design and analysis for which a material can withstand crack tip stresses

up to K_{IC}, beyond which the crack propagates rapidly. The failure stress σ_f is then related to the crack length a and the fracture toughness K_{Ic} by

$$\sigma_f = \frac{K_{IC}}{\alpha\sqrt{\pi a}} \tag{1.10}$$

where α is a geometrical parameter equal to 1 for edge cracks and generally on the order of unity for other situations. The literature contains expressions for K_I for a large number of crack and loading geometries, and both numerical and experimental procedures exist for determining the stress intensity factor of specific geometries. Expressions for K_I for some geometries are given in Table 1.1.

Table 1.1

Stress intensity factors for several common geometries. Adapted from [87]

Type of Crack	Stress Intensity Factor, K_I
Center crack, length $2a$, in an infinite plate	$\sigma_\infty\sqrt{\pi a}$
Edge crack, length a, in a semi-infinite plate	$1.12\sigma_\infty\sqrt{\pi a}$
Center crack, length 2a in plate of width W	$\sigma_\infty\sqrt{W\tan\frac{\pi a}{W}}$

By comparing Equation (1.9) and Equation (1.10) and making $\alpha = 1$, the interrelation between the stress intensity and energy-release approaches can be noticed:

$$\sigma_f = \sqrt{\frac{EG_c}{\pi c}} = \frac{K_{IC}}{\sqrt{\pi a}} \rightarrow K_{IC}^2 = EG_c \tag{1.11}$$

Cracks can propagate under mixed modes of loading as well. While the critical normal stress criterion is accepted as the criterion for the crack path in an ideal elastic-brittle material, there is still controversy over the initial direction of crack growth from a crack tip

under mixed mode loading conditions. Palaniswamy and Knauss [76], postulated that the mixed mode crack extends in the non-coplanar direction of maximum strain energy release rate, when this quantity reaches a critical value [13]. To obtain the direction of maximum energy release rate, they calculated the energy release rate for a kinked crack in terms of the length of the kink, and then let the length of the kink tend to zero. Chao and Shetty [18, 20], considered this criterion and performed measurements of the elastic modulus with reasonably good agreement in two commercial ceramics by the three flexure methods (four-point bend, three-point bend and biaxial flexure) and by a compression method. However, more more work is needed in the area of mixed mode loading to translate from testing to the understanding of fracture mechanisms [31]. Specifically, it is imperative to find out how the effects of the various modes should be combined mathematically to calculate fracture toughness and investigate the mechanisms of crack growth.

1.1.4 Modeling Brittle Fracture

Many theories on brittle polycrystalline materials have been developed at various size scales from homogenized solids at the macroscale to grain-sized modeling at the microscale, as well as atomic interactions at the nanoscale. Failure in brittle polycrystalline materials is a function of microstructural features, such as grain size and orientation, and of the effective interatomic interactions, both within the grains and across grain boundaries, and it is critical to understand the failure mechanisms in brittle polycrystalline materials for improvements in their development and application.

Multiscale computational modeling has contributed significantly to this effort. At the macro-scale, fracture is well described in terms of continuum models. A linear elastic fracture approximation is appropriated for brittle materials, where cleavage occurs with no fracture energy consumed by plastic deformation. Likewise non-linear models apply well to ductile materials where a high density of dislocations generated at the crack tip inhibits crack propagation. With both approximations, the material is assumed to be isotropic and at equilibrium. Several continuum damage models based on homogenizing the cracked solid and finding its response by degrading the elasticity of the material have been developed [4, 9, 24, 29, 42]. Discrete models based on a phenomenological framework where the fracture characteristics of the material are embedded in a cohesive surface traction-displacement relation have also been developed [15, 30, 68, 104]. Models that treat discontinuities in finite elements [75], including modifications of the principle of virtual work statement [26], meshless methods [11], extended finite element methods [10, 92, 66], and atomistic modeling of fracture [2, 32, 38] have been developed to advance simulation efforts of both quasi-static and dynamic fracture events. For example, the Extended Finite Element Method (XFEM) was introduced by Belytschko as a means to enrich the finite element displacement function to include discontinuities, but XFEM still does not capture complicated branching crack patterns [11].

In typical brittle materials and especially at the scale of grains, fracture often exhibits a much more complex mix of fracture modes since dislocation nucleation and glide are restricted to a few planes. Varying degrees of plastic deformation may consume strain energy depending on the plane and direction of fracture. This complexity is missed with

continuum approximations even when including crystallographic effects through crystal plasticity models. Discrete element methods (DEM) address these issues because of their discrete nature, and it is easier to introduce discontinuities and capture those effects during fracture. Since brittle polycrystalline materials are composed of an enormous number of grains, and their properties and performance are determined not only by the characteristics of individual grains but also by the interaction between them, in this research work, a computational model is developed based on a discrete element method to simulate fracture in brittle polycrystalline materials.

1.1.5 Discrete Element Methods

There have been many developments in *DEM* since its formulation by Cundall [23] over forty years ago. Many researchers have used these methods to study a variety of solids, such as concrete [40], rocks [54], sea ice [43] and ceramics [94]. These methods comprise a set of computational modeling techniques for the simulation of the dynamic behavior of a collection of multiple, independent, rigid or deformable particles of arbitrary shape subjected to various loadings [12]. As particles move, they can interact by forming new contacts or by breaking existing contacts. The interactions give rise to changes in the contact status and in the contact interactions forces, which in turn influences the subsequent movement of particles [12]. The microscale parameters needed to describe the material contact behavior are stiffness and strength parameters for the particles and the bonded contacts.

Discrete element methods are specifically geared for simulations involving a large number of bodies. In DEM the emphasis is on the change of contact locations and conditions, which cannot be defined a priori and which need to be continuously updated as the solution progresses [12].

The term *DEM* is most commonly associated with the definition provided by Cundall [23] which refers to any computational modeling framework that

- allows finite displacements and rotations of discrete particles, including complete detachment,
- recognizes new contacts automatically as the solution progresses.

Building a model based on *DEM* requires generation of a simulation domain composed of independent particles, detection of contacts, computation of contact forces, simulation of loading history and post-processing the results. Figure 1.5 shows the main stages of a *DEM* model including the addition of the fracture check stage which is the main contribution of this research. There exists a large number of methods, which in one way or another belong to a broad class of *DEM*. These methods are often classified according to the manner they deal with the features shown in Figure 1.6. A detailed review on the modeling of bodies, the time integration schemes and the contact force laws developed for *DEM* can be found in [50, 84].

Many scientific advances have been made using *DEM* to better understand the behavior of brittle materials. In 1996, Kun and Herrmann [59] presented a two dimensional (2D) discrete element model of deformable, breakable granular solids made from polygonal cells connected with beams for the simulation of fragmentation processes. The model was constructed in three steps. First, the granular structure of the solid was implemented by

constructing Voronoi polygons representing the smallest particles interacting elastically with each other. The polygons were considered rigid bodies which do not break and do not deform. Second, the elastic behavior was determined by the introduction of repulsive forces between the overlapping polygons and the beam model which was governed by the Young's modulus and shear modulus of the beam. Finally, the fracture of the structure was governed by the von Mises plasticity criterion. Using this model, granular or polycrystalline material could be realistically simulated and the trajectory of each fragment could be determined, which is of practical importance.

Later in 2001, D'Addetta [3] extended the work of Kun and Herrmann to include cohesive frictional materials and performed 2D simulations of explosion of a disc-shaped solid, the impact of a projectile with a solid block and the collision of macroscopic bodies. The results of the 2D simulations were found to be in reasonable agreement with the experimental observations. In both studies a micro-parameter calibration was missing.

In 2003, Ibrahimbegovic [48] presented a discrete model of heterogeneous structures based on a Voronoi cell representation for modeling brittle fracture phenomena for both quasi-static and dynamic loading. In this work, two types of forces governed the global response: the *cohesive forces* which influenced both elastic response and initial rupture patterns and which employs the geometrically nonlinear beam model of Reissner, and the *contact forces* between interacting detached particles governed the fragmentation process.From this work constitutive models for fracture at the microscale and mesoscale were developed. In 2004, Munjiza [70] presented a detailed book about the combined finite-discrete element method, which was initially developed in early 1990 and is applicable

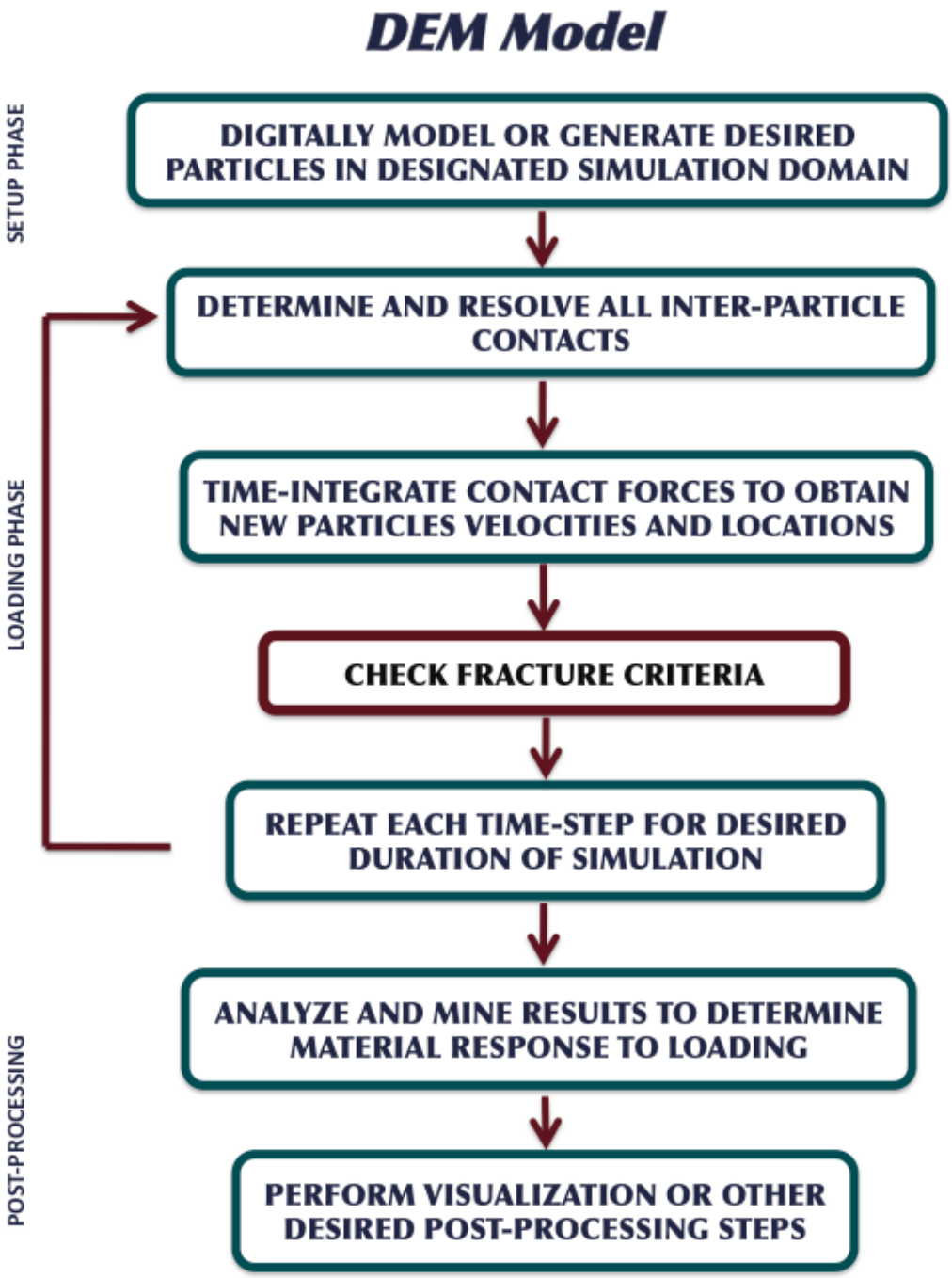

Figure 1.5

Main stages of a *DEM* model

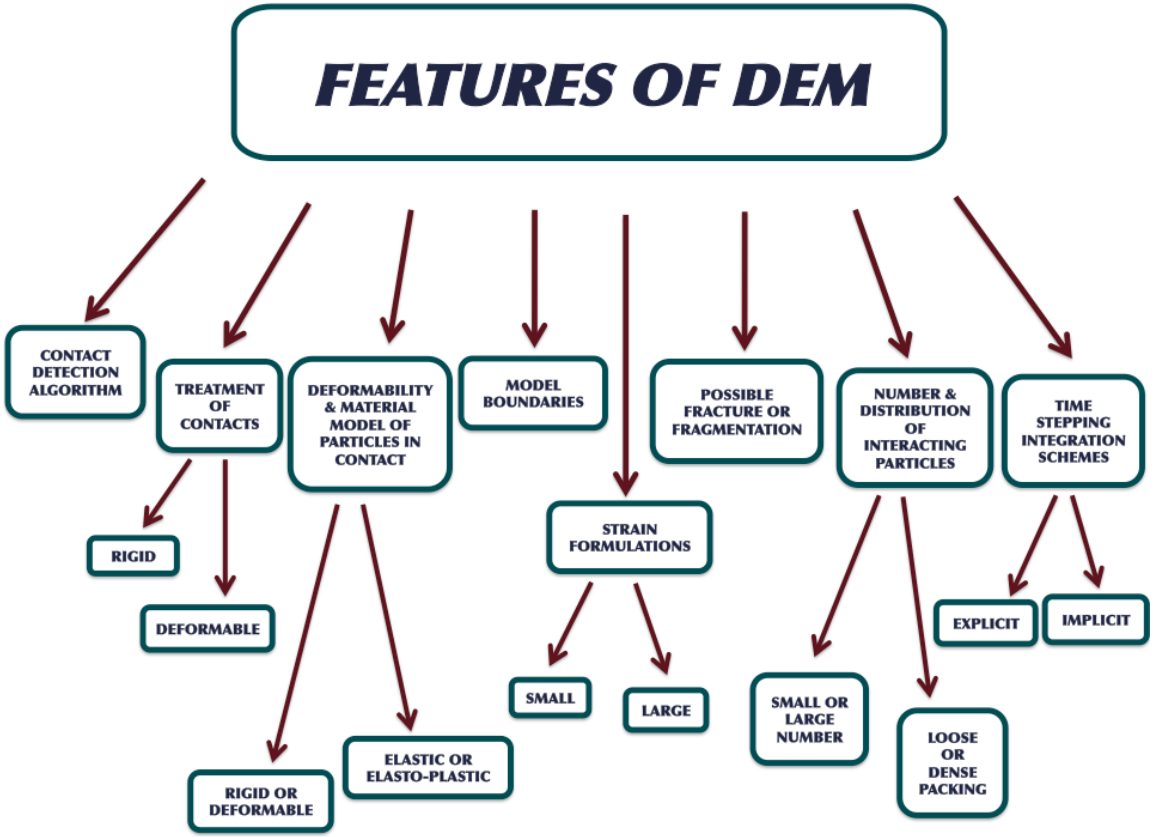

Figure 1.6

Features used for classifying discrete element methods

to several types of material damage problems such as failure, fracture and fragmentation. Klerck et. al [57] worked on modifications to an explicit discrete element/finite element code for a 2D model for discrete fracture in quasi-brittle materials under tensile and compressive stress fields which considered the Mohr-Coulomb failure criterion in compression and three independent anisotropic crack models in tension. Later that year, Potyondy and Cundall [82] proposed a model, called Bonded Particle Model (BPM), for rock represented by a dense packing of non-uniform sized circular or spherical particles bonded together at their contact points and whose behavior was simulated using DEM. Damage and its evolution were represented explicitly in the BPM as broken bonds; no empirical relations were needed to define damage or to quantify its effect on material behavior. The BPM reproduced qualitatively all of the mechanical mechanisms and phenomena that occur in rock, although adjustments and modifications could be necessary to obtain quantitative matches in specific cases.

Particle size controls model resolution but is not a free parameter. Instead particle size is related directly to the material fracture toughness which poses a severe limitation on the size of a region that can be represented with a BPM, because the present micro property characterization is such that the particle size must be chosen to be of the same order as the grain size. In 2006 Zhao et. al. [110] presented a particle simulation method to explicitly simulate the spontaneous crack initiation phenomenon in brittle materials. Solid materials were represented as circular particles bonded together through cementation in the particle assembly. Although particles had different shapes and sizes, they were assumed to be rigid. The strength of the material was simulated by using the strength of the bond at a contact

between two particles. To validate the particle simulation of spontaneous crack initiation phenomenon, a laboratory test was conducted using a model composed of gypsum. Even though the author mentioned that transgranular fracture can be simulated with their model, no specifics details are given on how this is performed. Yang et. al [106] presented results regarding the effects of microparameters on macroproperties of parallel-bonded PFC2D (a commercial discrete element code developed by Itasca Consulting Group) specimens and quantify their relationships; however those relationships are empirical in nature and modifications may be needed to model a specific material. In 2009, Tan et. al. [94] used DEM to model fracture in the machining process of polycrystalline SiC revealing the mechanical details of machining process at microscale. Microscopic material properties for particles and contacts were calibrated by comparing the results of numerical experiments such as unconfined compressive test, Brazilian test, three-point bending test and fracture toughness test with the equivalent experimental results.This was a 2D study using circular particles to represent the solid. Martin et. al [67], used DEM to study the evolution of cracks generated during sintering processes. They studied how constrained sintering between two parallel planes may lead a defect to grow into a crack and concluded that the presence of an initial defect is not a necessary condition to initiate cracks.

In 2010, Kazerani [54, 55] used a commercial discrete element code, called UDEC, which models material grains as polygonal random-shaped particles. The code was used to find a unique set of microparameters reproducing all material properties obtained from uniaxial/triaxial compression and tension simulations for Augig granite. In 2011, Bruchm$\ddot{u}$ller et. al. [14] presented a fragmentation model based on soft-sphere DEM for clusters of

spherical brittle particles. The model was only dependent on material parameters. A theoretically consistent description from the onset of fragmentation to the cloud formation after breakage was provided and model outcomes compared favorably to experimental results and other model predictions where very little deviation was encountered. In 2013, Le et. al. [62] propose a 2D DEM approach in fracture mechanics for brittle materials in which the material was modeled as an agglomerate of close-packed circular particles in contact. Crack propagation was indicated by suppression of contacts between particles by using the maximum circumferential tensile stress criterion. Le and collaborators continued that work by introducing a classical criterion of mixed mode crack propagation based on the value of the stress intensity factors, obtained by the analysis of two adjacent contacts near a crack tip [63]. Wolff et. al. [103] presented a DEM model with spherical particles to model the mechanical behavior under bending load of dense composite materials made from ceramic particles bonded together by polymeric layers. They considered the internal particulate structure of the material, including the particle size distribution, packing structure, and pore structure. Zhang [109] used the PFC2D code with bonded particle method to reproduce the fracture features, such as de-bonding, de-lamination and crack deflection, in ceramic laminates. André et. al. [7] developed a spherical discrete element model based on interaction given by 3D beam model, with a failure criterion based on an equivalent hydrostatic stress which was calibrated to fit experimental values of the macroscopic failure stress of silica glass, a perfectly brittle elastic material. The criterion produced more realistic crack patterns than traditional fracture mechanics when performing 2D simulations for studying complex crack phenomena such as the generation of hertzian cone cracks.

Researchers also tried combinations of DEM and others approaches such as the finite-discrete element method to model brittle rock [65], fracture process zone method to model quiasi-brittle materials [95], the impulse based finite-discrete element model to simulate fragmentation of brittle spheres [77], the extended finite element method to model cracks and coalescence in brittle materials [90] and most recently, in 2016 Yao et. al. [107] combined DEM with an extended rigid block spring method for modeling damage and failure in anisotropic cohesive brittle materials in which microstructure was represented using an anisotropic Voronoi diagram and the macroscopic behavior was controlled by the local deformation and failure properties of interfaces.

1.2 Motivation

A wide variety of polycrystalline materials are brittle, meaning that the cracks can form and propagate catastrophically with very little warning. Brittleness is a major problem with the reliable use of these materials in engineering applications. An unfortunate number of engineering disasters are related directly to this phenomenon, and engineers involved in structural design must be aware of the procedures now available to safeguard against brittle fracture. To overcome the limitations of the mechanical performance of brittle polycrystalline materials, it is necessary to gain a better understanding of the underlying mechanics and micromechanics of crack initiation and propagation of these materials [61].

In typical brittle materials, especially at the scale of grains, fracture often exhibits a complex mix of fracture modes. This complexity is missed with continuum approximations even when including crystallographic effects through crystal plasticity models. Failure in

these materials is a function of microstructural features, such as grain size and orientation, and of the effective interatomic interactions, both within the grains and across grain boundaries.

Realistic representations of polycrystalline materials, appropriate interaction laws and robust fracture solutions are currently missing from discrete models. In addition, despite all of the advances in the area of micromechanics, bridging between micro- and macro-scales still remains one of the most challenging goals [108]. Thus, the development of reliable computational tools that allow researchers to predict material behavior based on materials crystalline structure and understanding structure property relations at different length scales are of crucial importance.

1.3 Objectives and Scope

The main objective of this study is to investigate, numerically, the role of microstructural features, such as grain orientation and size in the deformation and failure of brittle polycrystalline materials. This work aims to develop, implement and validate a grain level micro-mechanical model based on the discrete element method with bonded contacts to assess inter-granular microcrack initiation and evolution in polycrystalline ceramics materials. Specifically, the influence of the grain boundary strength and stiffness on the fracture behavior of these materials was studied under various loading conditions. The focus of the work is to distinguish between predominately intergranular failure (through the grain boundaries) versus predominately transgranular failure (across grains) using simulations

based on microscale failure criteria for tensile, shear, torsion and rolling modes of intergranular motion.

The objectives are achieved through the development and implementation of a grain level micro-mechanical model based on DEM. The digital representation of the microstructure is composed of hexagonal, prismatic, honeycomb-packed grains of the same size and shape. The principle of virtual work is used to develop a fracture criteria for brittle polycrystalline materials and it is implemented into the discrete element model. At variance with other DEM methods, our DEM model actually breaks grains, not merely bonds between the grains.

1.4 Organization

This dissertation is composed of four chapters each of them headed by an introductory section. Chapter 1 contains detailed background and relevant literature regarding brittle polycrystalline materials and the discrete element method. Chapter 2 contains the description of the generation of uniform microstructures, and the development of a bonded particle model using the United States Army Corps of Engineers Engineer Research and Development Center (USACE-ERDC) in-house DEM software. Representative numerical examples are also presented in this chapter. In Chapter 3, a transgranular fracture model based on the DEM is presented. The fracture criterion is based on the continuous traction parameters which are described in terms of the discrete contact forces by using the principle of virtual work. Finally, concluding remarks and future works are presented in Chapter 4.

CHAPTER 2

INTERGRANULAR FRACTURE MODELING BASED ON DEM FOR BRITTLE POLYCRYSTALLINE MATERIALS

2.1 Introduction

Brittle polycrystalline materials, such as polycrystalline ceramics, are used in many applications due their extremely attractive properties, such as durability, high strength, high electrical and thermal resistance, and an ability to withstand the damaging effects of acids, oxygen, and other chemicals because of their chemical unreactivity. These materials are used in electrical and thermal insulators, high temperature crucibles for steel fabrication, elegant dinnerware, hip and other body parts replacements, car engine components (that combust fuel more cleanly), catalytic converters (which convert air pollution into less harmful gases) and many other applications. The list of applications of brittle polycrystalline materials is extensive but limited by their brittleness (the lack of any stress relief mechanisms at crack tips), which results in cracks growing to failure at significantly lower stresses than those necessary to initiate and propagate cracks in metals [31].

Crack propagation in polycrystalline materials is a complex process and involves a large number of microscopic events which are part of a generally intractable problem [61]. Crack propagation provides information about how cracks interact with the microstructure and may be either intergranular (along the grain boundary) or transgranular (through the

grains) [83]. The direction of the crack path depends on its fracture energy. In polycrystalline ceramics, a crack will change direction to follow a grain boundary or not depending on how much the crack must tilt or twist. The propensity of intergranular fracture also depends on the chemical composition and the changes in cohesion of the grain boundaries [21]. The fracture will continue through the grain instead of deviating along a grain boundary depending on whether the grain is in a favorable orientation for cleavage or not, because the cleavage energy of fracture through a grain depends on the crystallographic orientation [96].

Accurate modeling of failure of brittle polycrystalline materials is key to the design of microelectronic devices, machining of ceramics and ceramic composites, design of microelectromechanical systems and many other applications. Failure in brittle materials is not fully understood, but progress has been made in the characterization, visualization and modeling of the mechanics of brittle failure. However, many questions remain open for discussion, such as:

- How does the failure process occur in brittle materials subjected to multi-axial quasi-static and dynamic compressive loading?
- Can the failure process be quantified?
- How does the rate of deformation under dynamic compressive loading, friction at the grain boundaries, and the spatial distribution of flaws throughout the specimen affect the fragmentation of a brittle material?
- What effect does the friction at the grain boundaries have on the macroscopic strength?

Kraft at. al. in [58] presented a detailed description of the contributions made to answer the aforementioned questions. Many computational models have been developed that seem capable of describing the physics of the brittle failure process, but they usually neglect the

actual microstructure of brittle polycrystalline materials. Microstructure has been shown to play an important role in determining the evolution of microcracks (initiation, growth and coalescence) and in the failure strength of the material [30, 73, 108].

Since the microstructure of polycrystalline ceramics consist of crystal particles and pores, the ceramic bulk can be treated as an assemblage of discrete particles bonded together. Furthermore, the intergranular fracture of the ceramics can be naturally represented by separation of particles due to breakage of bonds. Brittle polycrystalline materials are composed of a large number of grains, their properties and performance are determined not only by the characteristic of each individual grain but also by the connectivity and interaction between them. Thus, a polycrystalline material is an assemblage of distinct grains variably bonded at grain boundaries and for which the DEM is uniquely suited.

In the current work, we expanded a basic discrete element model for non-cohesive spherical and cylindrical particles assemblies to include polyhedra-shaped bonded particles to better represent a brittle polycrystalline microstructure. The original model was developed at the United States Army Corps of Engineers Engineer Research and Development Center (USACE-ERDC) and is presented in several publications [17, 45, 46, 79, 80, 97]. This research work was partially sponsored by the ERDC's Military Engineering (M.E.) 6.1 Basic Research Program on High Performance Materials under the "Discrete Nano-Scale Mechanics and Simulation" project for ARO Contract # W911NF-11-D-0001-0123.

Herein a description is provided on generating the initial microstructure for a theoretical model based on *DEM* to simulate motion of equisized polyhedra particles, specifically hexagonal prisms, interacting in a 3D domain. An explanation of the main features in-

cluded in the development and implementation of the bonded hexagonal *DEM* model, such as geometry, contact laws, bonding, and contact detection algorithms is provided. Model failure is governed by the contact constitutive law. The model was implemented for a brittle, polycrystalline material consisting of two crystallographic orientations for the grains. The new formulation has the capability of capturing intergranular fracture within the particle model on the basis of bonding properties and forces acting on each discrete element. The contact detection is verified in a drop test case to observe motion of individual particles. The new formulation is implemented for several test simulation models of uniaxial compression, Brazilian test, and four-point bending to observe the effect of various loading conditions on the fracture behavior of the bulk material formed by an assembly of bonded particles and the stresses generated in the models.

2.2 Digital representation of the microstructure

The focus of this section is to obtain the geometry of the material microstructure. In the current work we are interested in the generation of synthetic uniform microstructures. From a statistical point of view, a microstructure can be classified as uniform if a single symmetrical peak is observed on a frequency histogram of the grain diameters, intercept lengths, or areas plotted on a logarithmic scale.

Morphological and crystallographic characteristics of microstructure, alongside other variables like loading conditions, particle geometry and grain-level constitutive properties, are among the most important attributes controlling behavioral prediction. Thus, the ability to digitally represent microstructures with high fidelity in computational models is vital to

their capability of making accurate property predictions [36]. Synthetic microstructures are a powerful tool for determining what aspects of the microstructure are important for a given property and they can play a critical role for testing and understanding computational tools for material behavior analysis and prediction. Computational tools capable of creating synthetic microstructure are spatial tessellation tools, physics-based growth models and geometric packing tools.

Discrete element models require detailed geometric information on individual particles. The representative shape for a particular body controls the accuracy of the geometrical modeling of each particle and thus controls the flexibility and scope of the simulations, the accuracy and the efficiency of the contact detection algorithm and the computation of the normal and tangential forces at each contact [41]. Flexible shape descriptors are needed that can represent a variety of arbitrary shapes with minimal data for initiating DEM simulations.

The grain geometry of a given microstructure can be obtained from digitalization of scanning electron microscopy images (SEM micrographs) or by means of geometrical algorithms. Both methods are based on the following steps to generate a synthetic microstructure for numerical simulations:

1. **Obtain statistical characterization from experimental data** to get a more complete representation of grain-level microstructures. Groeber presented a list of statistical descriptors in [36]. They are classified as morphological descriptors, such as grain volume and spatial orientation; crystallographic descriptors, such as microtexture function and orientation distribution function; and correlation descriptors, such as aspect ratios.
2. **Create the grains with a realistic distribution of grain size and shape**. The creation of a collection of idealized grains is performed and distributions of size and shape equivalent to those observed in the experimental data are required.

3. **Assemble the grains**. Arrangement and spatial location of the grains inside a representative volume are determined.

4. **Assign crystallographic orientation to the grains** to account for the micro texture. The crystallographic orientations are assigned to the grains in such a way that the crystallographic descriptors are statistically equivalent to the experimental data.

2.2.1 Digitalization of SEM micrographs

Microstructures can be digitally generated, for example, using DREAM.3D, an open source and modular software package that allows the user to re-construct, instantiate, quantify and visualize the microstructures digitally [37]. In the version 6.2.327 of DREAM.3D grains can be described as ellipsoids, super-ellipsoids or cube-octahedra and finite element meshes of the entire microstructure can be obtained for further analysis. Figure 2.1 shows a synthetic microstructure with its mesh composed of 30 equiaxed grains generated using DREAM.3D.

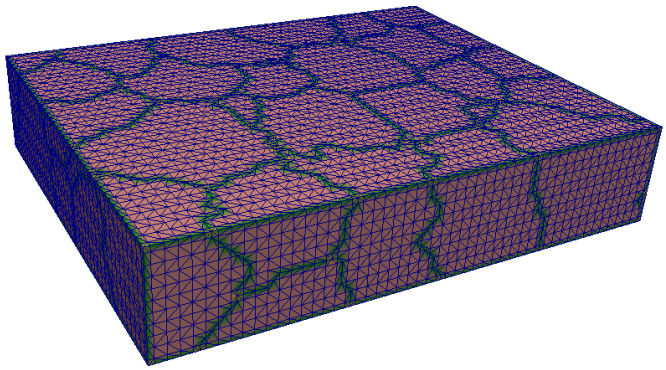

Figure 2.1

A sample mesh of a synthetic microstructure composed of 30 grains created using DREAM.3D

DREAM.3D does not have a shape class for packing hexagonal cells. Another disadvantage is that it does not give independent meshes for each grain which is needed for creating DEM input data. However, it can be used to extract statistical information regarding the size, shape, and orientation distribution of grains from electron backscatter diffraction (EBSD) stack of images. This information is then used to create the type of microstructure we are interested in.

Detailed guidance on how to digitally generate microstructures representative of brittle and biological layered materials, such as polycrystalline ceramics and nacre, is provided in the ERDC's interim report [88]. This report contributed to the development of the computational nanomaterials test-bed under the ERDC's project *Discrete Nano-Scale Mechanics and Simulations* and covers three main points: 1) Explanation of the microstructure generation process. 2) Description of the steps for generating and meshing microstructures using DREAM.3D. 3) Process for microstructure's visualization using PARAVIEW software.

2.2.2 Generation of a uniform synthetic microstructure

To computationally simulate a polycrystalline microstructure, a perfectly uniform synthetic microstructure is generated by using prismatic particles of equal size arranged in an hexagonal close packing (HCP) arrangement to achieve maximal possible efficiency while filling a 3D space. Here, efficiency means both minimization of the void space and easy to implement. A close packing of hexagonal prisms, known as hexagonal prismatic honeycomb lattice was implemented. Each grain is represented by a convex hexagonal prism,

composed of six rectangular sides of length r and two hexagonal bases separated by a thickness t as shown in Figure 2.2. Each hexagonal prism has a total of 8 flat faces, 12 vertices (corners), and 18 straight edges. The result of filling a 3D space with grains is a regular lattice, whereby each lattice point represents the center of a grain.

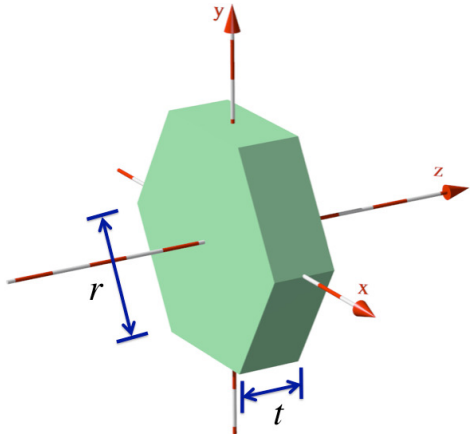

Figure 2.2

A single grain represented by a hexagonal prism, with side length r and thickness t

In the current study, polycrystalline silicon carbide (3C-SiC and 6H-SiC) are used as a model materials. Figure 2.3 shows fine grains of 3C-SiC.

The HCP lattice is created one plane at a time with only two plane types (A and B) needing to be defined, as shown in Figure 2.4. For each plane, two different row types (Row 1 and Row 2) are created. Table 2.1 summarizes the xyz coordinates for each lattice point (associated with the grain center) that fill a 3D box with dimensions $a \times b \times c$. The coordinates are described for each row and corresponding plane, where r is the length

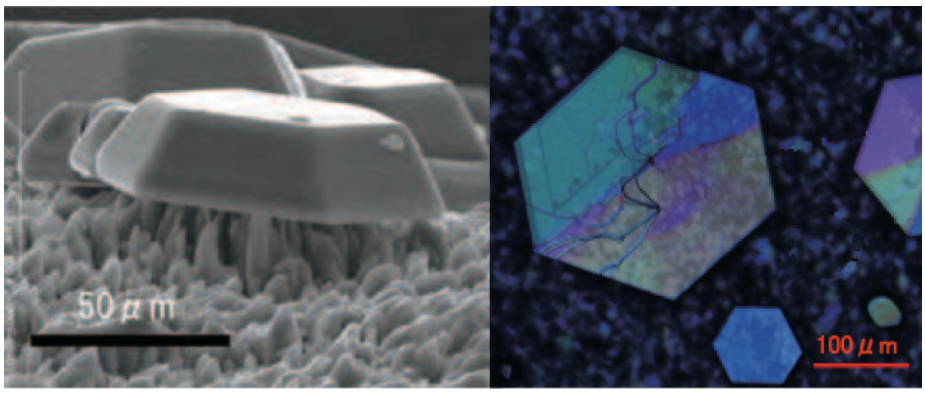

Figure 2.3

Side view (scanning electron microscopy image) and top view (optical microscopy image) of fine particles on the polycrystalline 3C-SiC source plate [72]

of each side, t is the thickness and the quantity h is given by $h = \frac{3r}{2}$. The natural numbers i, j and k are the indexes of each lattice point and are in the range:

$$1 \leq i \leq \left\lfloor \frac{2a}{\sqrt{3}r} \right\rfloor - 2, \qquad 1 \leq j \leq \left\lfloor \frac{\frac{2}{3}(b + \frac{r}{2})}{r} \right\rfloor - 1, \qquad and \qquad 1 \leq k \leq \left\lfloor \frac{c + \frac{t}{2}}{t} \right\rfloor - 1.$$

Given the center of each grain, (c_x, c_y, c_z), the coordinates (v_x, v_y, v_z) of the 12 vertices of each grain are calculated as described in Table 2.2, where n is a natural number in the range $1 \leq n \leq 6$.

The side length $\overline{r}$ can be $\leq r$. For the case where $\overline{r} < r$, grains are placed in the box in such a way that space for the grain boundary is provided, as demonstrated in Figure 2.5. Details on how the coordinates for both the lattice points and vertices for each grain where determined are presented in Appendix A and follow the general idea described in [51].

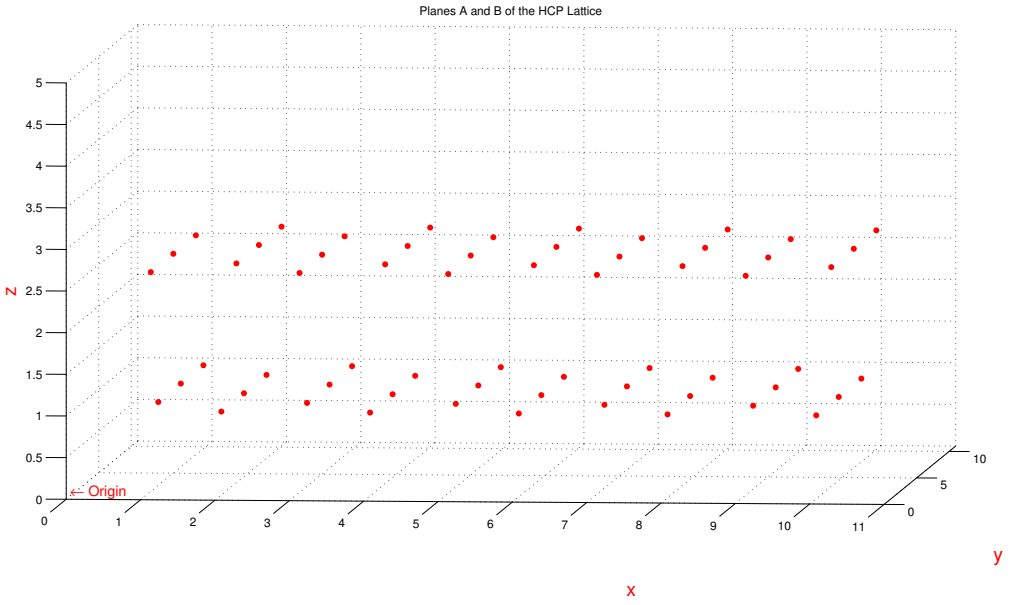

Figure 2.4

Example of a HCP lattice consisting of two plane types A and B that fills a $12\times12\times4$ box

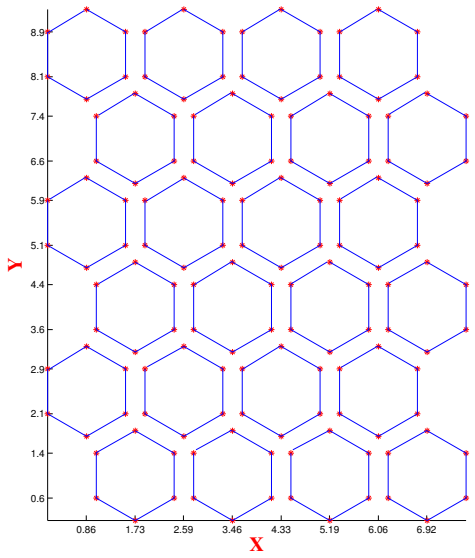

Figure 2.5

A $9.5 \times 7.5 \times 1$ box filled with grains with side's length $\overline{r} = 0.75$

Table 2.1

The xyz coordinates of lattice points

Plane	Row	c_x	c_y	c_z
A	1	$\sqrt{3}ir$	$r+(j-1)h$	$\frac{t}{2}+(k-1)t$
A	2	$\frac{\sqrt{3}}{2}(2i-1)r$	$r+(j-1)h$	$\frac{t}{2}+(k-1)t$
B	1	$\sqrt{3}ir$	$r+jh$	$\frac{t}{2}+kt$
B	2	$\frac{\sqrt{3}}{2}(2i-1)r$	$r+jh$	$\frac{t}{2}+kt$

Table 2.2

The xyz coordinates of grain's vertices

Face	v_x	v_y	v_z
Front	$\overline{r}\cos(60(n-1))+c_x$	$\overline{r}\sin(60(n-1))+c_y$	$-t+c_z$
Back	$\overline{r}\cos(60(n-1))+c_x$	$\overline{r}\sin(60(n-1))+c_y$	$t+c_z$

Using the lattice as a template, the 3D space can be filled with hexagonal prisms (representing grains) by placing grain centers at lattice points, as shown in the example in Figure 2.6. The planes are placed in a simple pattern of A-B-A-B-A...

2.2.2.1 Crystallographic orientation of grains

Identification of cleavage planes is crucial for understanding the fracture behavior of brittle materials. Introduction of the crystallographic information in material models that aims accurate modeling of the fracture behavior is also important.

As described in Section 2.2 a uniform synthetic microstructure representative of our model material was constructed from a single layer of equisized hexagonal prism-shaped

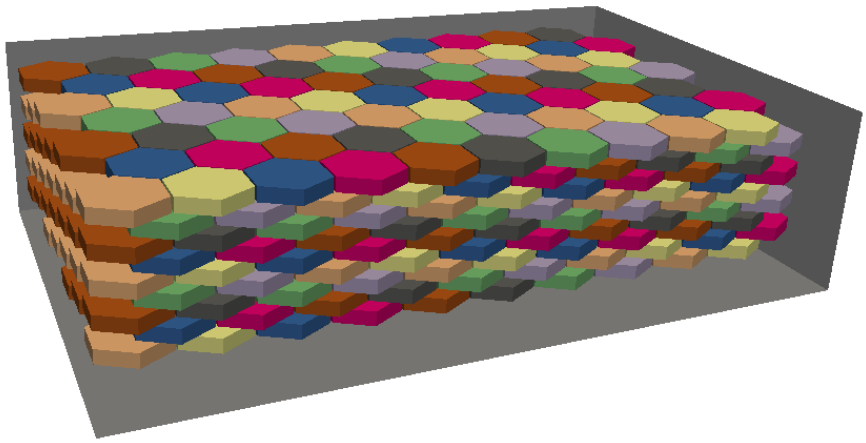

Figure 2.6

A 3D box filled with hexagonal prisms (representing grains) packed using a HCP lattice

particles, each particle representing a single grain in the microstructure. The grains were arranged in a HCP arrangement.

For HCP silicon carbide (our model material) the $< 10\bar{1}0 >$ and $< 11\bar{2}0 >$ directions were identified as the hardest and softest directions on the basal plane, respectively [5, 60] (See Figure 2.7).

Crystallographic orientation for each grain was assigned randomly in a DEM simulation. The orientation of the crystals were randomly assigned at $0°$, $60°$ or $120°$ with respect to the $< 10\bar{1}0 >$ or $< 11\bar{2}0 >$ directions, since these orientations correspond to active slip systems in Si-C.

When simulating transgranular fracture (explained in Chapter 3) each grain was divided into slabs depending on its crystallographic orientation. Each slab is also a polyhedral

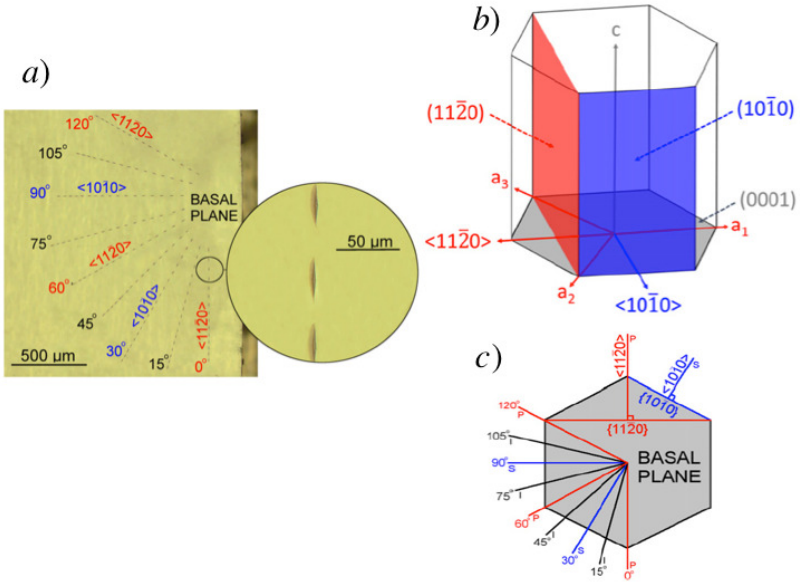

Figure 2.7

a) Radial indentation pattern on 6H-SiC. b) HCP unit cell. c) Basal plane (c-plane) with primary (P), intermediate (I) and secondary (S) directions [60]

DEM particle. For the case of the $< 11\bar{2}0 >$ direction, three slabs are created and each of one is either a rectangular prism or an isosceles triangular prism, as shown in Figure 2.8. For the case of the $< 10\bar{1}0 >$ direction, two slabs are created they have similar geometry as shown in Figure 2.9.

2.3 DEM model development

The *ERDC-DEM* code is a public-domain code for simulating the interaction of rigid particles and is based on the numerical solution of *Newton's second law* of motion using a Velocity Verlet algorithm [46, 17, 80]. There is no pre-defined material model in DEM. It only includes contact search algorithms and contact laws. The contact search is performed in two stages. First, a coarse search is performed to identify potentially contacting parti-

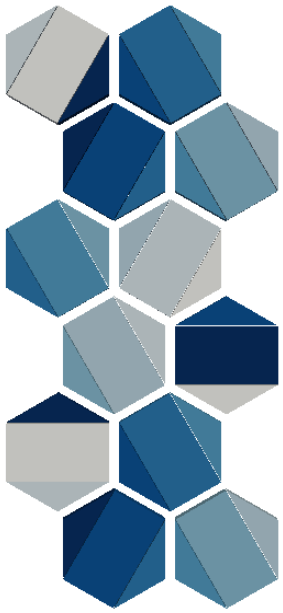

Figure 2.8

Grains divided into three slabs oriented at $0°$, $60°$ or $120°$ with respect to the $< 11\bar{2}0 >$ direction

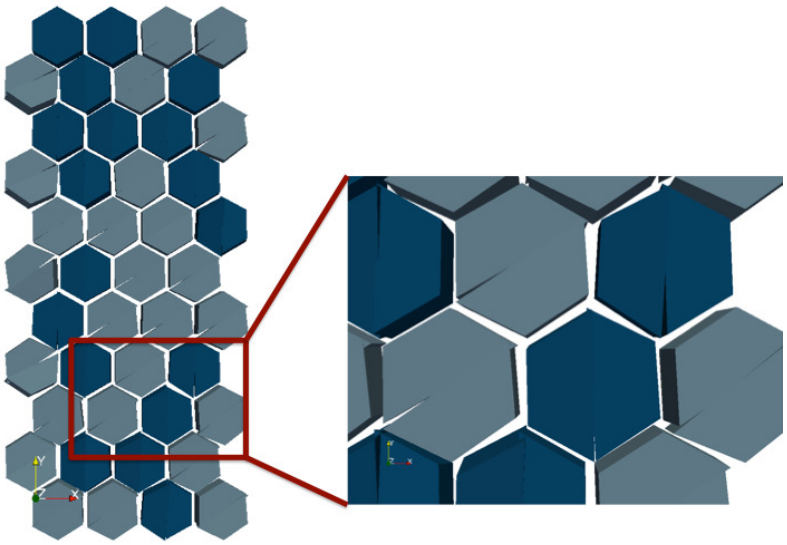

Figure 2.9

Grains divided into two slabs oriented at $60°$ or $120°$ with respect to the $< 10\bar{1}0 >$ direction

cles; then a fine search is performed to determine which pairs of particles are actually in contact [97].

The contact law implemented in the *ERDC-DEM* code is a *binary Coulombic contact law* with *Hooke's law* used to compute the contact force. This is a classical formulation for modeling soils, but the force scheme is modified to better accommodate the behavior of brittle polycrystalline materials. Currently, the contact is a Kelvin model, represented by a purely viscous damper and a purely elastic spring connected in parallel as shown in Figure 2.10 .

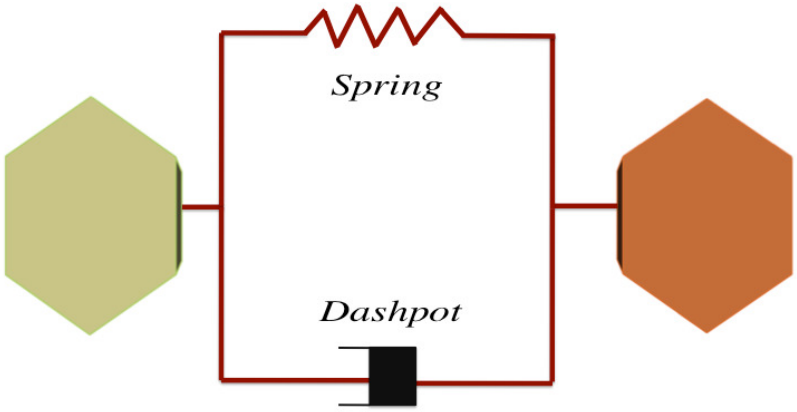

Figure 2.10

Kelvin model schematic representation

The *ERDC-DEM* code only uses the viscous part for unload-reload mode. The fact that the unload modulus is greater than the loading modulus dissipates energy for the primary

loading. However, once unloading begins some other damping is needed to eliminate high-frequency oscillations, i.e., the viscous part is used to maintain the system's stability state [78]. The contact forces between two particles are determined from the overlap and relative movements of the particle pair according to a specified force-displacement law. There are seven degrees of freedom that DEM can consider: Compression, Tension, Shear, Torsion, Bending, Rolling and Sliding.

2.3.1 Contact detection

The efficient detection of contacts in a discrete element simulation is of crucial importance for predicting the motion and interaction between particles which yields to the successful simulation of the mechanical behavior of different types of materials. Contact searches can involve 50% to as much as 80% of the total computational time of a simulation regardless of the particle's shape. When modeling brittle polycrystalline materials, most DEM models use disks or spherical elements [94, 109, 110, 16, 93, 62, 105, 47, 89, 33, 103, 69] because those particle contacts can be easily detected (only the radius is required to describe the geometry of the particle) and computer memory and processing time are minimal compared with detection of contacts between non-spherical particles. However the rotation and rolling of spherical particles do not reflect the behavior of real grains, therefore *DEM* simulations using non-spherical particles to represent grains can more accurately capture this behavior. Complex geometries, such as polygons and polyhedra can be problematic because detecting contacts, bonding particles together, and calculating forces and torque

for edge-edge, edge-corner, and corner-corner contacts can be complicated and computationally expensive [27, 100].

When dealing with convex polyhedra there are several methods for detecting contacts. Barbosa proposed a method that first identifies the faces of each polyhedron that are visible from the centroid of the other and gives the highest probability of contact to the face that can be seen best [8]. Then, starting with the faces with highest probability and their respective corners, all corner-to-face contacts are checked. If contacts are detected, the checks continue with the next visible faces, in order of decreasing probability, until no more contacts are detected. Next, the possibility of edge-to-edge contacts is examined. An edge-to-edge contact can only occur if both edges are visible from each other's centroid. The disadvantage with this method is that too many combinations need to be tested for the simple case of two contacting cubes. Cundall proposed a different approach based on the idea of a "common-plane" bisecting the space between two convex polyhedra [22]. Instead of testing for contact between the polyhedra directly, he proposed to determine a common-plane, then test each body separately for contact with it. The geometrical algorithm devised by Cundall to locate and move the common-plane consists of maximizing the gap between the common-plane and the closest corners of each body. Once a common-plane has been defined, only corner-to-plane tests need to be carried out to detect contacts between two bodies, since face and edge contacts are recognized by counting the number of corner-to-plane contacts.

The contact detection approach adopted and implemented in our discrete element model is defined for dilated polyhedral particles. This technique, proposed by Hopkins [44, 45],

is also suitable for non-convex polyhedra shapes that are based on the dilation process from mathematical morphology. An arbitrary polyhedron shape is dilated by placing the center of a sphere of fixed radius at every point on the surface. The dilated vertices become spheres, and the edges become cylinders. The sharpness of the vertices and edges can be adjusted by varying the dilation radius. For simplicity, in this work only the vertices and edges of each particle are dilated. After dilation, each particle has 14 spheres, 36 cylinders and 24 flat triangular facets. Figure 2.11 shows the desired grain's shape with a triangular mesh to be used for the contact search as well as its dilated vertices and dilated edges.

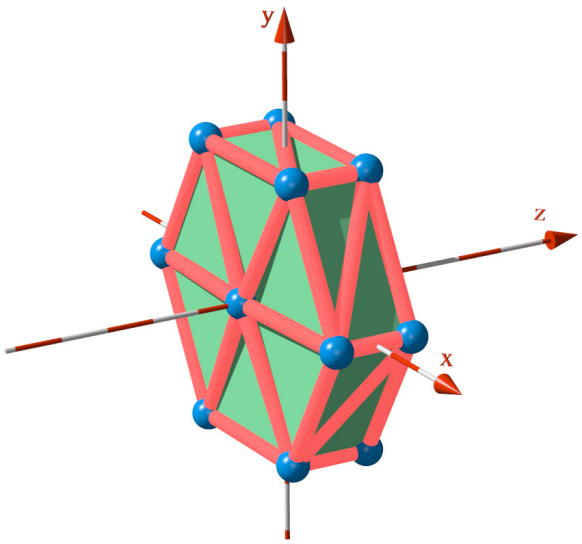

Figure 2.11

A single grain represented by a hexagonal prismatic shaped particle with spheres for the vertices, cylinders for the edges, and triangular facets for the surfaces

Defining a contact between two dilated polyhedral particles requires determining which spheres, cylinders and triangular faces, called *primitive* particles, are in contact. Contact

between two dilated polyhedral particles can be grouped into four categories: vertex on vertex, vertex on facet, vertex on edge, and edge on edge (as illustrated in Figure 2.12), which can be translated as sphere on sphere, sphere on flat triangular surface, sphere on cylinder, and cylinder on cylinder. Two primitives particles only interact if they penetrate each other.

The contact detection process is divided into two stages: a coarse detection stage followed by a fine detection stage. In both stages, the simulation space is discretized into cells of equal size. Then, a cell-based search is performed which is $O(n)$ and requires that all cells must be larger than the diameter of the largest particle in the system. The practical cost of the simple cell method scales as O(m*n), where n is the number of particles and m is the average number of particles in a cell, making the theoretical cost of $O(n)m$ become large with a large variation among particles sizes. To overcome this disadvantage, Walizer and Peters [97] proposed a bounding box search algorithm which essentially tries to make $m = 1$ even if there is a large difference among particle sizes. Without the initial coarse search to localize the contacts, an all-on-all search would be required which is $O(n^2)$ operation, for a system with n particles.

The *coarse search* is performed to detect which particles might be in contact by using either a basic or bounding box algorithm depending on the distribution of particle size. The *basic search* algorithm is simple to implement and requires that all cells be larger than the diameter of the largest particle in the system. Performance of the basic search algorithm degrades when particles in the simulated system are not of similar size. Details on the basic search algorithm are provided in Appendix B. The *bounding box search* algorithm

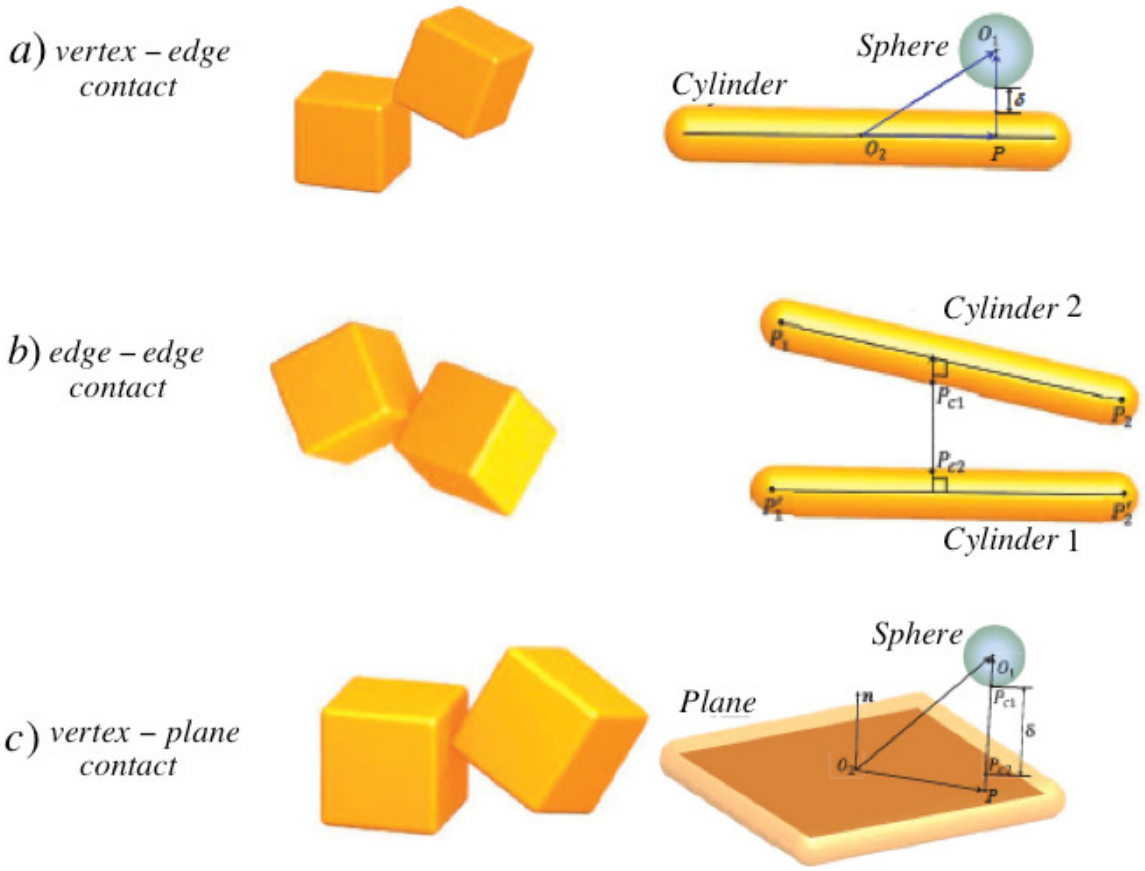

Figure 2.12

Contact detection of two dilated polyhedron particles in a) vertex-edge contact, b) edge-edge contact and c) vertex-plane contact [52]

is an extension of the basic search algorithm except the cell size is based on the diameters of the smallest particle, rather than the largest particle. Therefore, for systems in which particle sizes are non-uniform, performance is not degraded as it would be in the basic search algorithm [97]. Details on the bounding box algorithm are provided in Appendix B.

The *fine search* is performed to find pairs of particles, identified in the previous stage, that are actually in contact and to determine the degree of contact, i.e., the distance of penetration or closure. The algorithm loops over each pair of particles listed in the coarse search stage and proceeds according to the types of particles participating in the contact. There are a total of four contact cases considered in this research, composed of a combination of facets, sphere or cylinders. details on how each case is treated can be found in [45]. The **sphere-sphere** contact penetration is computed in terms of the distance, D, between the centers of the the radii of the two spheres, R_{S1} and R_{S2}:

$$penetration = R_{S1} + R_{S2} - D$$

The **sphere-facet** contact penetration is computed in terms of the distance, D, between the center of a sphere to the plane containing the three nodes of the triangular facet and the radii of the sphere R_{S1}:

$$penetration = R_{S1} - D$$

The **sphere-cylinder** contact penetration is computed in terms of the distance, D, between the center of the sphere and the principal axis of the cylinder:

$$penetration = R_S + R_C - D$$

where R_S and R_C are the radii of the sphere and the cylinder respectively.

The **cylinder-cylinder** contact penetration is computed in terms of the closest approach, D, between the two the principal axes of the cylinders:

$$penetration = R_{C1} + R_{C2} - D$$

where R_{C1} and R_{C2} are the radii of the two cylinders.

For non-bonded contact, if penetration is greater than 0, then contacts is made. For bonded contacts, if $|penetration| \leq bonding\_distance$ or $penetration \geq 0$, then contact is made.

2.3.2 Contact force law

After particle contacts are identified, the contact forces are computed and integrated to determine particle motions. The normal and shear components of the contact force are calculated from a modified Hooke's model with parallel viscous damping and a Coulomb friction cap on the tangential force. This spring-slider force scheme is intended for repulsive forces only and is meant for the modeling of granular materials (shown in Figure 2.13 below). Therefore damping of the system is achieved using an alternative energy dissipation method. This is accomplished by applying a multiplier (reciprocal of the coefficient of restitution) to increase the spring stiffness during the unload portion of the contact cycle. When applied to every contact instance, the system is effectively damped at the particle-particle level. The contact forces and moments are computed from the relative particle motion, material properties, and the existing contact force.

The microscale parameters that must be defined within DEM to adequately calculate the particle motion due to frictional resistance at the contacts are the translational and ro-

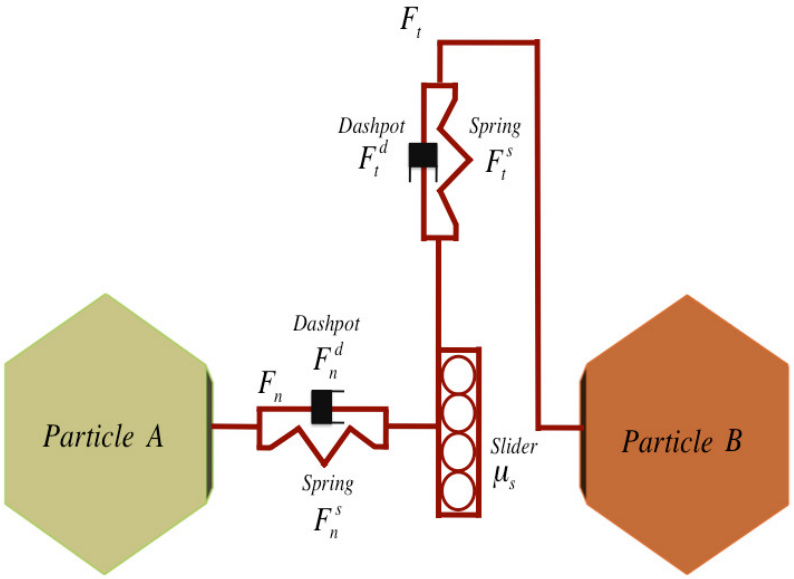

Figure 2.13

Particle contact interaction Model

tational stiffness parameters for each contact type (determined by the particle's material pair). The stiffness parameters describe the resistance to deformation in response to an applied force. Translational stiffness parameters represent the ratio of the corresponding component of the applied force on the body to the corresponding deformation. Rotational stiffness parameters represent the ratio of the corresponding component of the applied moment to the angle of rotation. In the International System of Units, translational stiffness is typically measured in newtons per meter (N/m) and rotational stiffness is typically mea-

sured in newton-meters per radian (Nm/rad). Shi and Polycarpou [91], and the references therein, present approaches for measuring and modeling contact stiffness at the mesoscale.

$$\textit{Translational Stiffness Parameters} \begin{cases} K_n & \textit{normal spring stiffness} \\ K_s & \textit{shear spring stiffness} \end{cases} \tag{2.1}$$

$$\textit{Rotational Stiffness Parameters} \begin{cases} K_r & \textit{rotational stiffness} \\ K_t & \textit{torsional stiffness} \end{cases} \tag{2.2}$$

The contact force $\vec{F}$ and the contact moment $\vec{M}$ are calculated as:

$$\begin{aligned} \vec{F} &= \vec{F}_n^s + \vec{F}_t^s + \vec{F}_n^d + \vec{F}_t^d \\ \vec{M} &= \vec{M}_r + \vec{M}_t + \vec{M}_r^d + \vec{M}_t^d \end{aligned} \tag{2.3}$$

where $\vec{F}_n^s$ and $\vec{F}_t^s$ are the normal and tangential components of the contact force, $\vec{F}_n^d$ and $\vec{F}_t^d$ are the normal and tangential components of the damping force, M_r and M_t are the rolling and torsional moments, and $\vec{M}_r^d$ and $\vec{M}_t^d$ are the damping moments for rotational and torsional modes respectively.

The normal ($\vec{F}_n^s$) and shear ($\vec{F}_t^s$) components of the contact force are computed in terms of the relative displacement ($\vec{U}_r$) as:

$$\vec{F}_n^s = -K_n \vec{U}_n$$

$$\vec{F}_t^s = \begin{cases} -(K_s \vec{U}_s) & \|\vec{F}_t^s\| < \|\vec{F}_n^s\|\mu_s \\ \vec{F}_t^s \left(\dfrac{\vec{F}_{fs}}{\|\vec{F}_t^s\|} \right) & \|\vec{F}_t^s\| \geq \|\vec{F}_n^s\|\mu_s, \|\vec{F}_t^s\| \neq 0 \end{cases} \tag{2.4}$$

where U_n is the projection vector of relative displacement, $\vec{U}_r$, on normal vector, $\vec{n}$, between the particles centers, $U_s = U_r - U_n\vec{n}$ is the projection vector of the relative displacement on shear vector, $\vec{s}$, and μ_s is the sliding friction coefficient. The relative displacement $\vec{U}_r$ is computed in terms of the translational (V) and rotational (V_t) velocities of particles A and B as:

$$\vec{U}_r = \Delta t((V_B + V_{tB}) - (V_A + V_{tA}))$$

And the Coulomb frictional forces are computed as:

$$\begin{aligned} \vec{F}_{fr} &= \vec{F}_{ft} = -\vec{F}_n\mu_r \\ \vec{F}_{fs} &= -\vec{F}_n\mu_s \end{aligned} \tag{2.5}$$

where μ_r is the rolling coefficient of friction and μ_s is the sliding coefficient of friction.

Within the DEM code the force is composed of the state variable contact force and a damping force. The latter depends on the current velocity but it is not included as part of the contact state. The normal and tangential components of the damping force are computed as:

$$\begin{aligned} \vec{F}_n^d &= 0.1\sqrt{C_{res}K_n m_{crit}}\frac{\|U_n\|}{\Delta t} \\ \vec{F}_t^d &= 0.1\sqrt{K_s m_{crit}}\frac{\|U_s\|}{\Delta t} \end{aligned} \tag{2.6}$$

where C_{res} is the coefficient of restitution and m_{crit} is the critical mass for damping computation.

The rolling resistance (M_r) and torsional resistance (M_t) components of the moments are computed in terms of the relative angular velocity ($\Delta\omega$) as:

$$M_r = K_r \Delta\omega_r \Delta t + \vec{M}_r^d$$
$$M_t = K_t \Delta\omega_t \Delta t + \vec{M}_t^d \tag{2.7}$$

where ω_t is the normal component of the relative angular velocity between two particles in contact, and $\Delta\omega_r = \Delta\omega - \Delta\omega_t$ is the shear component of the relative angular velocity. $\vec{M}_r^d$ and $\vec{M}_t^d$ are the damping moments for rotational and torsional modes respectively, they are computed as:

$$\vec{M}_r^d = 0.1\sqrt{K_r I_{crit}}\Delta\omega_r$$
$$\vec{M}_t^d = 0.1\sqrt{K_r I_{crit}}\Delta\omega_t \tag{2.8}$$

where I_{crit} is computed from the moment of inertia tensor of each particle.

Therefore, each kinematic variable ($U_n, U_s, \omega_r, \omega_t$) has a conjugated variable (F_n, F_s, M_r, M_t). The contact state is saved for use in the next time step and the combined contact force and damping force are summed into each contacting particle to get total momentum balance.

2.3.3 Bonded contacts

To model bonded contacts, our DEM adopts a simplified description of the Bonded Particle Model (BPM) proposed by Potyondy and Cundall [82]. This model mimics the behavior of a collection of grains joining by bonded contacts by assuming that the Coulomb contact and the bonding act in parallel as illustrated in Figure 2.14. The deformations are

common for both spring contacts and bonding, and the forces are additive. However, a fully parallel model requires force-state variables to be stored separately for contact and bonding, requiring an excessively large amount of memory. The problem is resolved by using a quasi-parallel model. The normal force is fully parallel because the normal penetration is an absolute quantity and therefore the contact force is not a state variable. The shear force and moment quantities are based on incremental relationships and thus require the force as a state variable. Details can be found in [81].

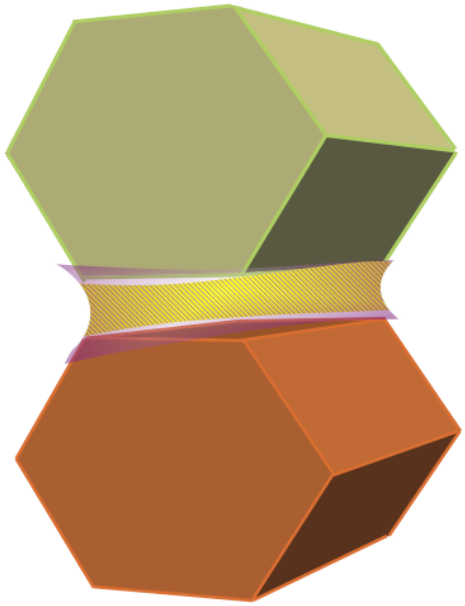

Figure 2.14

Two bonded polyhedra-shaped discrete elements

The required parameters to define the bonded contacts are

$$\begin{aligned} k_{bn}: &\quad \textit{continuum bond normal stiffness} \\ k_{bs}: &\quad \textit{continuum bond shear stiffness} \end{aligned} \tag{2.9}$$

From these bond parameters, the spring normal stiffness (K_{bn}) and the spring shear stiffness (K_{bs}) are defined as:

$$\begin{aligned} K_{bn} &= k_{bn} A_b \\ K_{bs} &= k_{bs} A_b \end{aligned} \tag{2.10}$$

where $A_b = \pi r^2$ is the effective bond area based on the dilation radius of the smallest contacting particle.

Similarly, the spring rotational stiffness (K_{br}) and the spring torsional stiffness (K_{bt}) are defined as

$$\begin{aligned} K_{br} &= k_{bs} J_b \\ K_{bt} &= k_{bn} I_b \end{aligned} \tag{2.11}$$

where $I_b = 0.25\pi r^4$ is the area moment of inertia and $J_b = 2I_b$ is the polar moment of inertia.

Therefore, the normal (F_{bn}) and the shear (F_{bs}) forces due to bonding are computed from the scaled stiffness values 2.10 as:

$$\begin{aligned} F_{bn} &= K_{bn} \Delta v_n \Delta t \\ F_{bs} &= K_{bs} \Delta v_s \Delta t \end{aligned} \tag{2.12}$$

Similarly, the rolling resistance moment (M_{br}) and the torsional resistant moment (M_{bt}) are defined as:

$$M_{br} = K_{br}\Delta\omega_r\Delta t$$

$$M_{bt} = K_{bt}\Delta\omega_t\Delta t \tag{2.13}$$

In contrast to the compression-only criteria for cohesionless materials, bonded contacts can carry a tensile load up to a tension limit. The parameters for defining the yield criteria for the bonds are:

$$t_{bn}: \quad \textit{bond normal strength}$$

$$t_{bs}: \quad \textit{bond shear strength} \tag{2.14}$$

Thus, the normal, shear, rolling and torsional limits of failure are computes respectively as:

$$F_{bn\_limit} = t_{bn}A_b$$

$$F_{bs\_limit} = t_{bs}A_b$$

$$M_{r\_limit} = t_{bn}\left(\frac{I}{r}\right)$$

$$M_{t\_limit} = t_{bs}\left(\frac{J}{r}\right) \tag{2.15}$$

Failure occurs when the total force and total moment due to any of the contact modes exceeds these limits for a combined yield criterion. Bond failure due to tension, shear

bending and torsion occurs when the corresponding bonding force exceeds the particle-to-particle corresponding strength

$$
\begin{aligned}
F_{bn} &> F_{bn\_limit} \\
F_{bs} &> F_{bs\_limit} \\
M_{br} &= M_{r\_limit} + F_{fr} \\
M_{bt} &= M_{t\_limit} + F_{ft}
\end{aligned}
\tag{2.16}
$$

The bond is considered brittle and is broken if the limit load is exceeded for any mode of contact. In the case of loss of bonding, the contact behaves a a simple Coulomb contact for the duration of the simulation. The properties of the bulk material will change as expected in a material with damage as the bonds are being broken.

Part of the DEM model preparation is the bond initialization stage which is performed after an assembly of particles has been generated and compacted up to a point in which particles are in contact. During the particle placement process the bonding parameter values are initialized to zero. During the bond initialization stage particles will be bonded together if their contact radii overlap. Bonds are formed between particles which are not necessarily in direct contact. At the end of the particle placement process an initial stress-free state is obtained by resetting all physical overlaps to zero and residual forces and moments are also reset to zero as well as the velocities to zero out the kinetic energy. This stress-free state is attained by storing, as a custom contact property, any physical overlap that exists between two particles during the bond initialization stage. This " initial" overlap is then subtracted from each subsequent determination of overlap at each contact, resulting

in a static assembly of bonded particles with zero overlap and no contact force at the start of each loading simulation. Resetting the overlaps is an important process to avoid prematurely broken bonds from expansion due to spurious residual stresses during particle placement. If overlaps are not reset, when bonds are broken the contact overlaps may produce exaggerated contact forces leading to non-physical behavior. After bonds have been applied the material model is completed and ready for computational testing.

2.4 Discrete Element Stress

An equivalent Cauchy stress tensor is computed for each discrete element as proposed by André [7] and Peters [79]:

$$\bar{\sigma}_i = \frac{1}{2V_i}\left[\frac{1}{2}\sum_j \vec{d}_{ij} \otimes \vec{f}_{ij} + \vec{f}_{ij} \otimes \vec{d}_{ij}\right] \tag{2.17}$$

where $\otimes$ is the tensor product, $\bar{\sigma}_i$ is the equivalent Cauchy stress tensor of the discrete element i, V_i is the volume of the discrete element i, $\vec{f}_{ij}$ is the total contact force exerted on the discrete element i by the discrete element j and $\vec{d}_{ij}$ is the moment arm vector between the centroid of the discrete element i and each contact point with the discrete element j.

Using the Cauchy stress tensor, the 2D invariants p and q are also computed for each particle:

$$\begin{aligned} p &= \frac{\sigma_{xx} + \sigma_{yy}}{2} \\ q &= \sqrt{\frac{1}{4}\left(\sigma_{xx} - \sigma_{yy}\right)^2 + \sigma_{xy}^2} \\ \theta &= \frac{1}{2}\tan^{-1}\left(\frac{2\sigma_{xy}}{\sigma_{xx} - \sigma_{yy}}\right) \end{aligned} \tag{2.18}$$

2.5 DEM simulations

The implementation of the contact-bonding force law, hexagonal prismatic particle DEM model was implemented in the initial ERDC DEM code. The code was used to perform several testing under different loading conditions. Multiple simulations using the same particle size and packing with an increased size in simulation box were performed. To verify that the contact detection procedure works properly a simple drop test simulation was performed and the particle-particle and particle-surface interactions observed.

This research aims to model the fracture behavior of brittle polycrystalline materials. There are a number of accepted tests for determining the elastic moduli, strength, fracture toughness of brittle polycrystalline materials, as well as measuring the crack growth rate as a function of the stress intensity factor. For a detailed list of these tests, see [31, 96]. The implementation of the contact-bonding law was tested with three different model configurations (uniaxial compression, Brazilian test, and four-point bending test) were loaded until fracture to observe the breakage of bonds and resulting fracture morphology in the microstructure (see Figure 2.15). The parameters used in the initial setup for the simulation tests are included in Table 2.3. The bonding parameters used in the bonded particle models for the three simulation tests are provided in Table 2.4.

Different software tools are available to visualize the microstructure. We chose two visualization software tools: PARAVIEW [56] and POV-RAY [1]. The former is an open-source, multi-platform data analysis and visualization application developed by *Kitware* which is very flexible but difficult to customize. The latter is a high-quality ray-tracing soft-

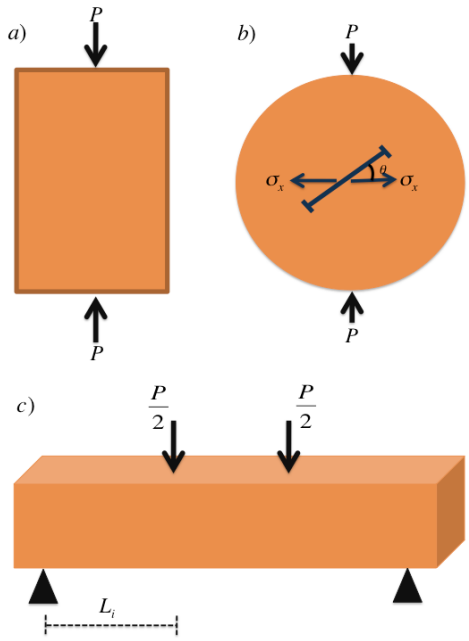

Figure 2.15

Simulation Tests: a) Uniaxial compression test. b) Brazilian test and c) Four point bending test

Table 2.3

DEM contact parameters used for the simulation tests

Input Parameters	Values
Time step increment	0.001
Particle size	
Particle specific gravity	3.10
Gap for initial contact	0.02
Particle - particle normal spring stiffness constant, K_n	5000
Particle - particle shear spring stiffness constant, K_s	2000
Particle - particle rolling stiffness constant, K_r	0.0
Particle - particle torsional stiffness constant, K_t	0.0
Particle - particle inverse of coefficient of restitution, C_{res}	2.0
Particle - particle Coulomb sliding friction coefficient, μ_s	0.0
Particle - particle Coulomb rolling friction coefficient, μ_r	0.5
Particle - wall normal spring stiffness constant, K_n	10000
Particle - wall shear spring stiffness constant, K_s	2000
Particle - wall rolling stiffness constant, K_r	0.0
Particle - wall torsional stiffness constant, K_t	0.0
Particle - wall inverse of coefficient of restitution, C_{res}	10.0
Particle - wall Coulomb sliding friction coefficient, μ_s	0.0
Particle -wall Coulomb rolling friction coefficient, μ_r	0.0

Table 2.4

DEM bonding parameters used in the drop and uniaxial compression simulation tests

Bonding Input Parameters	Values
Bond normal stiffness, K_{bn}	5000
Bond shear stiffness, K_{bs}	2000
Bond normal “tensile” strength, t_{bn}	20000
Bond shear strength, t_{bs}	10000

ware tool for creating nearly any data portrayal that can be imagined. We used PARAVIEW for initial visualizations of our data, and then used POV-RAY for special visualizations.

2.5.1 Drop test on unbonded particles

The drop test is used to verify that contacts between particles and surfaces are correctly detected. The drop test model consists of 168 close packed hexagonal prismatic particles not bonded of randomly assigned crystallographic orientation. The blue colored particles have crystallographic orientation at 60° with respect to the $\{10\bar{1}0\}$ plane, and the gray colored particles have crystallographic orientation at 120° with respect to the $\{10\bar{1}0\}$ plane. DEM and bonding input parameters used in this simulation test are defined in Tables **??** and **??** respectively. After generating the particles, and completing the DEM simulation, the results were visualized using PARAVIEW. Starting from their initial positions at a height of 50 mm, as shown in Figure 2.16a), the particles were affected only by gravitational forces and start immediately fell towards the ground floor, as shown in Figure 2.16b). Once the particles came into contact with each other, they started to repel each other, as visible in Figure 2.16c). Contacts are indicated by the small red spheres visible in the simulation results. As contacts were broken, the red spheres disappear. The particles bounced up and down until all particles finally settled due to the dissipated energies through the collisions as shown in Figure 2.16d) and Figure 2.16e).

2.5.2 Uniaxial compression test

For the uniaxial compression test, a single plane model consisting of 44 hexagonal prismatic particles, resulting in model specimen size $5\,mm \times 10\,mm \times 2\,mm$ was generated

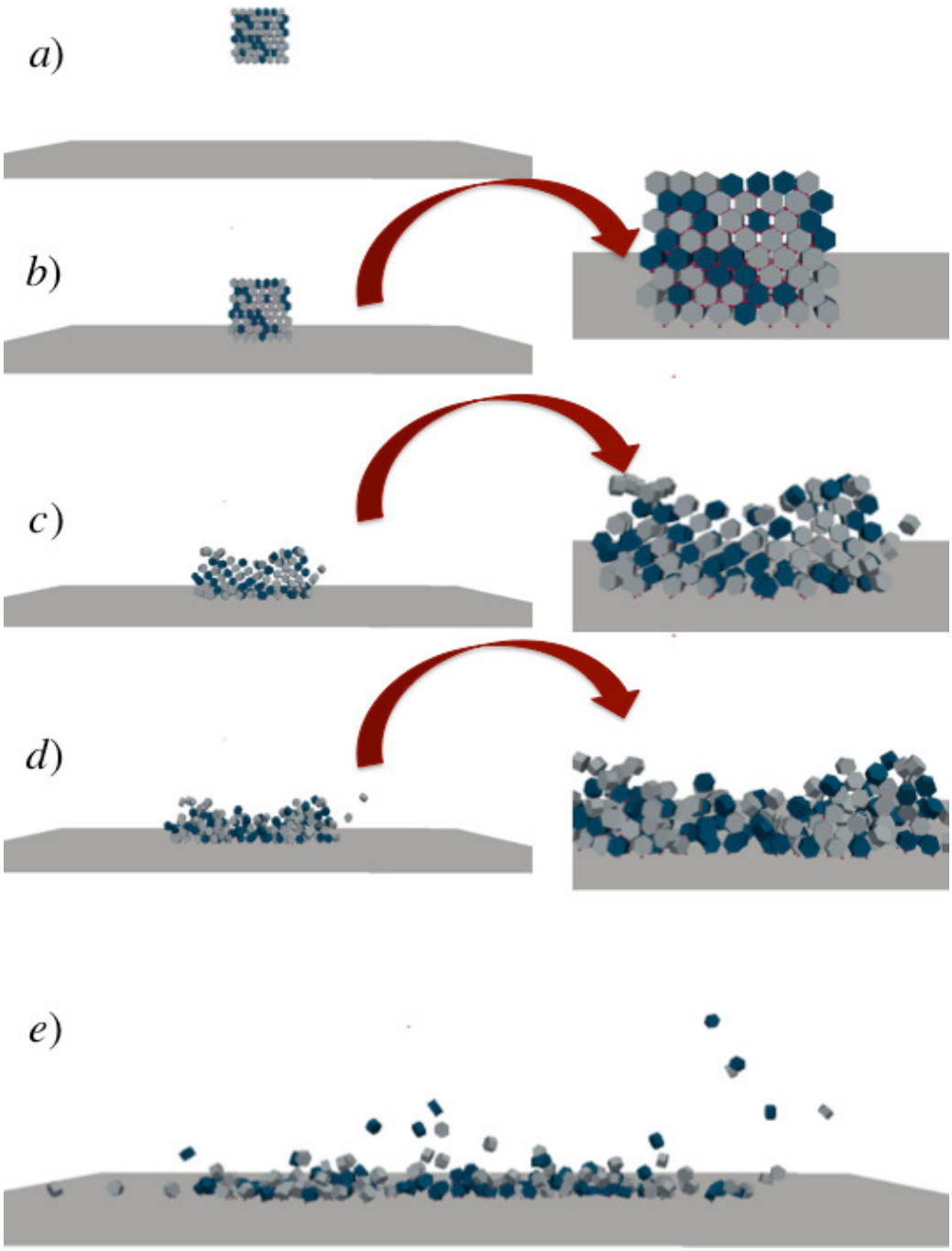

Figure 2.16

Drop Test consisting of 168 polyhedra at a) Initial configuration, b) after 296 time steps/seconds, c) after 350 time steps/seconds, d) after 400 time steps/seconds and e) after 500 time steps/seconds

as described in Section 2.2.2. The parameters used in the initial DEM simulation are included in Table **??**. Loading velocity of $50\ mm/s$ was applied on the four wall surfaces using DEM rigid elements to compress the particles until initial contact was achieved as shown in Figure 2.17. After the initial contact model was generated, only upper and bottom walls were loaded to perform the uniaxial compression simulation test. Loading velocity of $0.001mm/s$ was applied on the two wall surfaces using DEM rigid elements to compress the particles as shown in Figure 2.18. The bonding forces were activated and dynamic equilibrium was performed until the energy of the system was minimized. A dilation radii of $0.05\ mm$ was used for detection of contacts.

The uniaxial compression DEM simulation consists of 4 steps: First, after creation of the simulation domain as shown in Figure 2.17a), the top, bottom, right and left walls are loaded until they interact with the particles at the boundaries as shown in Figure 2.17b). Second, the four walls are kept loaded until all polyhedral particles are in contact depicted by red beams as shown in Figure 2.17c). In this part of the simulation the four walls are identically loaded. Figure 2.17d) shows depiction of the unbonded contacts. Third, initialization of bonds is performed by making each contact detected in the previous step a bonded contact which are depicted as black beams as shown in Figure 2.18a). Contacts between particles and surface plates are kept unbonded (represented by the red beams). In this step all forces and stresses are reset to zero as explained in Section 2.3.3. The bonding parameters applied to the model are provided in Table **??**. Depiction of the bonds at this stage is shown in Figure Figure 2.18c). Finally, the top and bottom walls are loaded to perform the actual uniaxial compression simulation test. Figure 2.18b) shows the breakage

of the bonded contacts after 100 time steps, and Figure 2.18d) shows the remaining bonded and broken contacts represented by black and red beams respectively. When particles are no longer in contact, i.e. when contacts are lost, the beams disappear. All of this simulation results are visualized using PARAVIEW. Particle stresses are also depicted using POV-RAY as illustrated in Figure 2.19. The particle stresses were calculated as described in Section 2.4. The DEM input files used for this simulation are in Appendix C.

2.5.3 Four-point bending test

A simply supported rectangular beam loaded in four-point flexure is illustrated in Figure 2.15c). This test is used for the evaluation of ceramics under development, and provides a larger area under stress and a greater sampling of the flaw population over the three-point flexure test. Another advantage of the four-point flexure test over the three-point flexure test is the the former represents pure bending and the latter provides shear stress contributions [31]. The maximum stress in the central portion of the beam between de upper loading points on the opposite surface is:

$$\sigma = \frac{PL_i}{wt^2}$$

where P is the load and L_i is the distance between the outer support and the inner support. Usually $L_i = \frac{L}{4}$ or $L_i = \frac{L}{3}$. It is recommended for most ceramics that the span-to height ratio be between approximately 5:1 and 10:1 to avoid shear stress contributions for the shorter bars and large deflections affecting the calculations for the longer bars [31]. It is expected that failure take the form of a tensile crack from the bottom to the top.

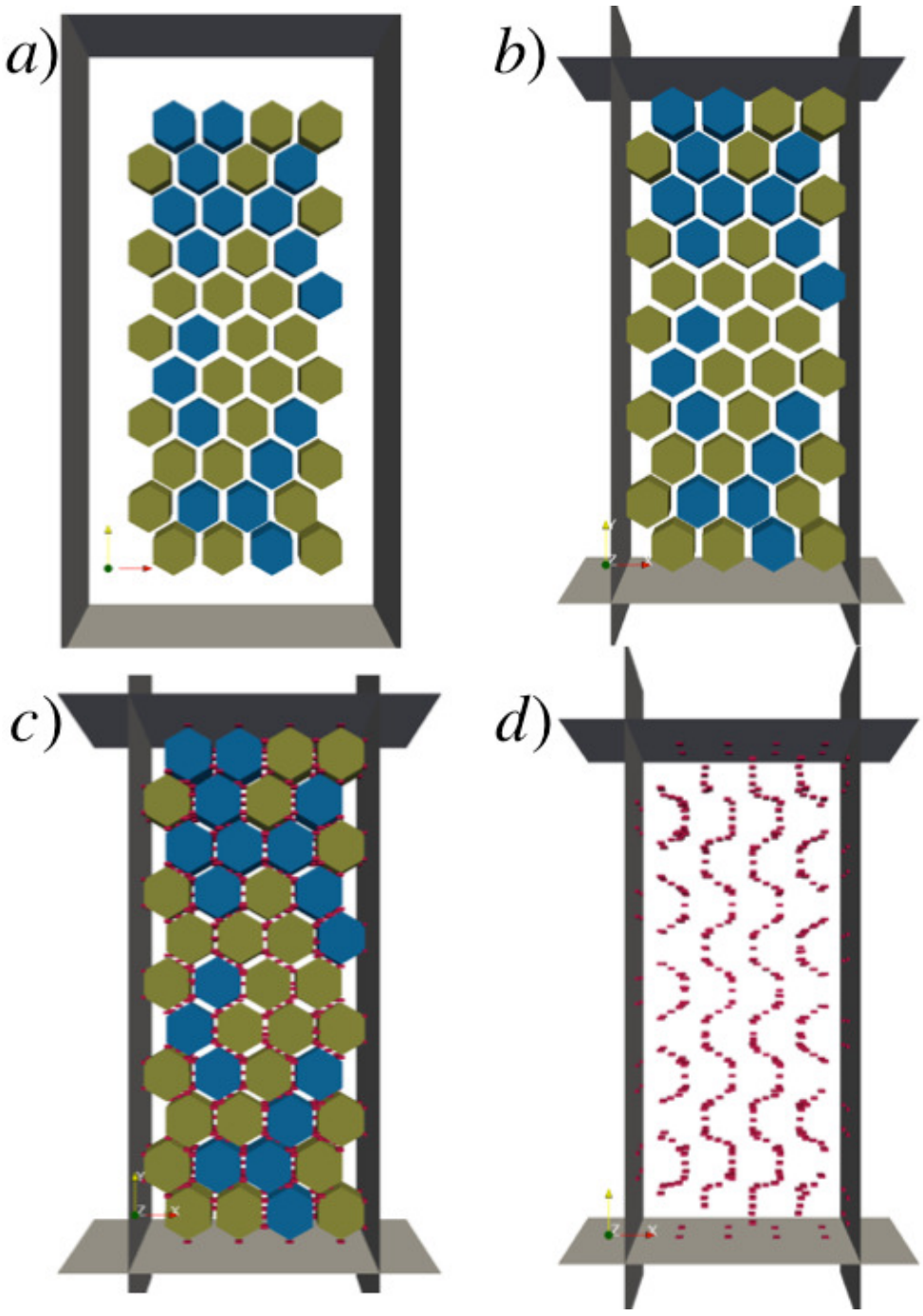

Figure 2.17

Configuration set up of 44 polyhedra at a) Initial configuration, b) after 1000 time steps/seconds when walls get in touch with particles at the boundary, c) after 800 time steps/second when particles are in contact, d) Depiction of contacts (red beams)corresponding to the figure in c)

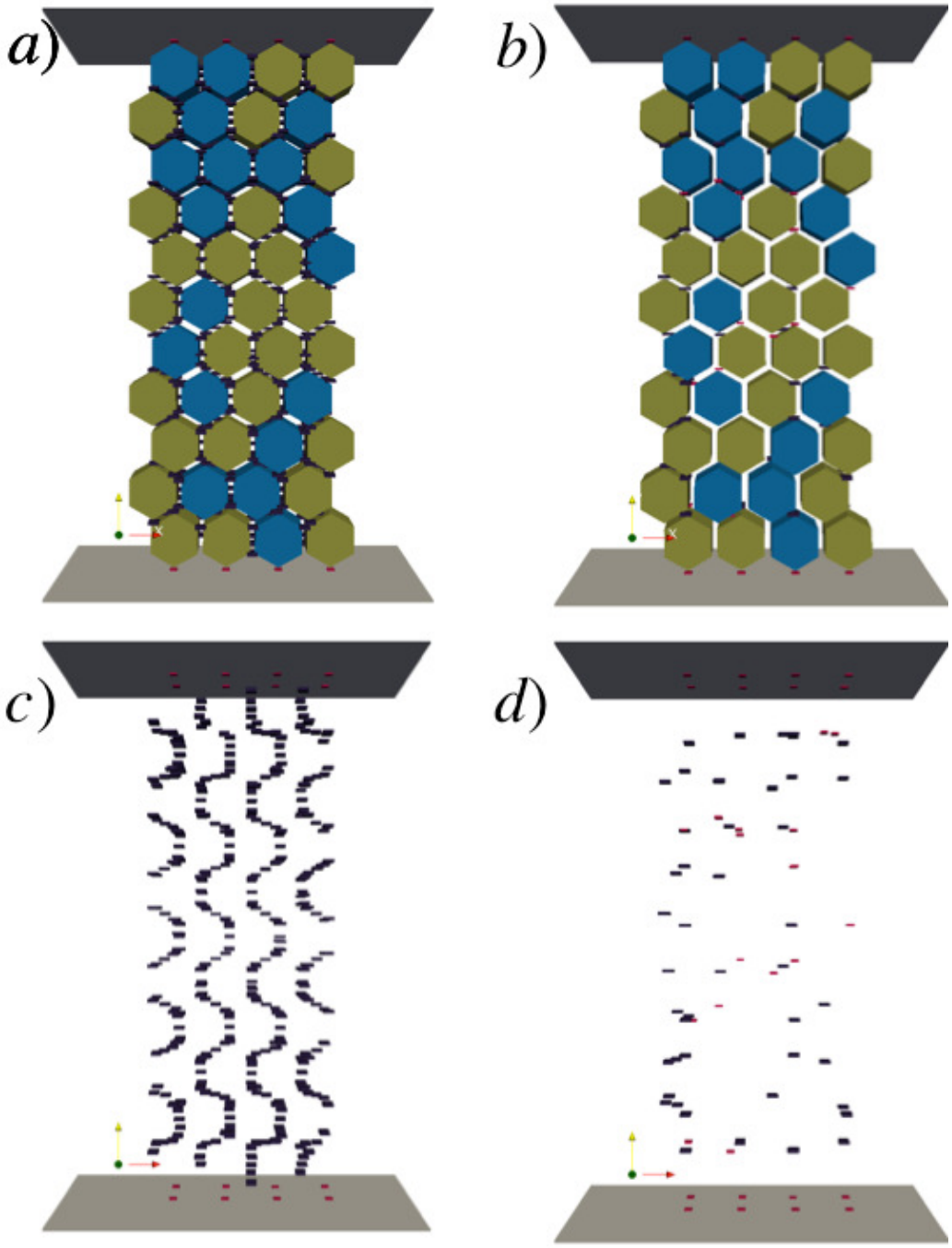

Figure 2.18

Uniaxial test consisting of 44 polyhedra at a) Initial configuration with bonded contacts depicted by black beams, b) after 100 time steps/seconds when load is applied in the vertical direction. c) and d) Depiction of contacts at 0 and 100 time steps/second respectively. Broken bonds are shown in red

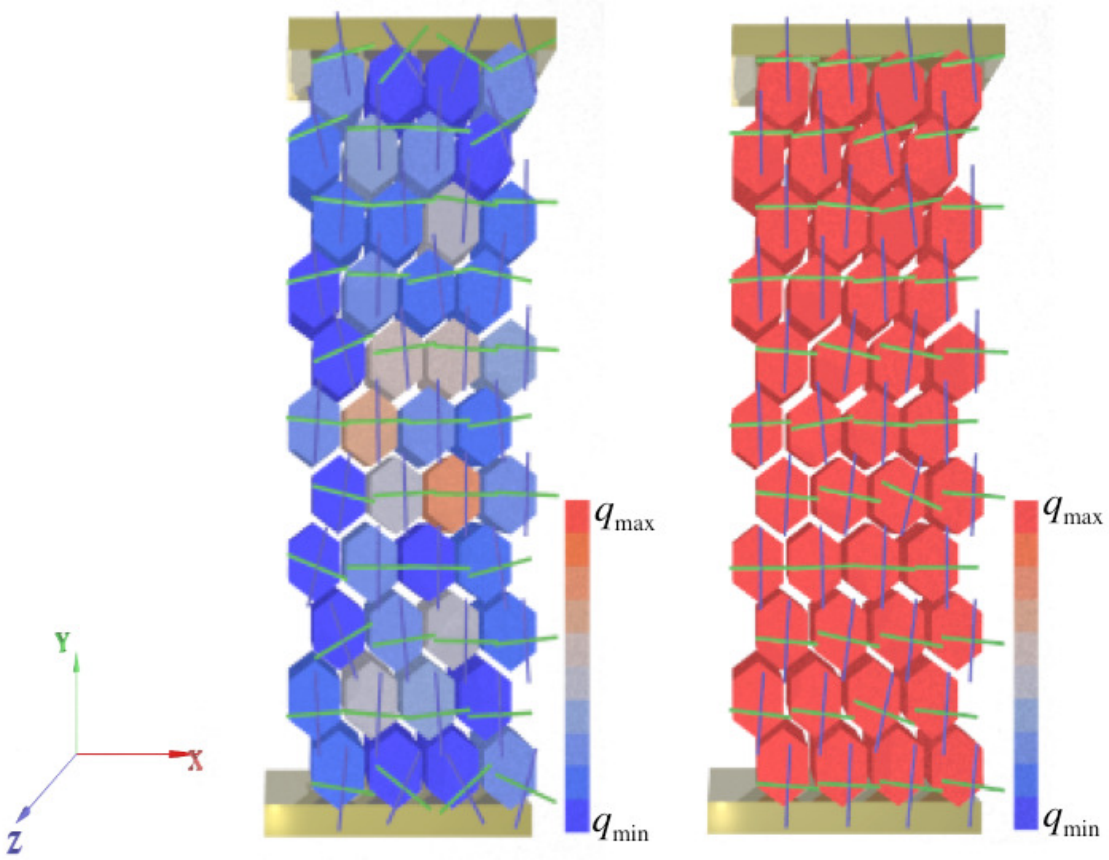

Figure 2.19

Particle stresses at a) first time step b) after 100 time steps/seconds when load is applied in the vertical direction. Blue and green lines represent principal directions

For the four-point bending test, a single plane model consisting of 95 polyhedral particles (Figure 2.20a)), resulting in model specimen size $20\ mm \times 5\ mm \times 5\ mm$ was generated as described in Section 2.2.2. The parameters used in the initial DEM simulation are included in Table **??**. Loading velocity of $30\ mm/s$ was applied on the four wall surfaces using DEM rigid elements to compress the particles until initial contacts between particles were achieved as shown in Figure 2.20b). After the initial contact model was generated, bonds were initialized and only the two upper flexure points were loaded to perform the four-point bending simulation test (Figure 2.20c)). Loading velocity of the two upper plates was $2\ mm/s$ represented by DEM rigid elements to compress the beam at the top as shown in Figure 2.20c) after 500 time steps. Figure 2.20d) shows depiction of the bonded contacts. The bonding forces were activated and dynamic equilibrium was performed until the energy of the system was minimized. A dilation radii of $0.05\ mm$ was used for detection of contacts. the bonding parameters were all set as described in Table 2.5. Figure 2.21a) - Figure 2.21d) shows evolution of the simulations at 150, 250, 400, and 500 time steps. Figure 2.22a) - Figure 2.22d) depic evolution of the contacts at 150, 250, 400, and 500 time steps. It is observed that bonds start to be broken from the bottom up to the top of the beam.

2.5.4 Brazilian test

In this test a circular specimen is loaded in compression along its diameter (at two opposing circumferential points) as shown in Figure 2.15b), producing a tensile stress at the center of the disk. A biaxial stress state is generated in a specimen under diametral

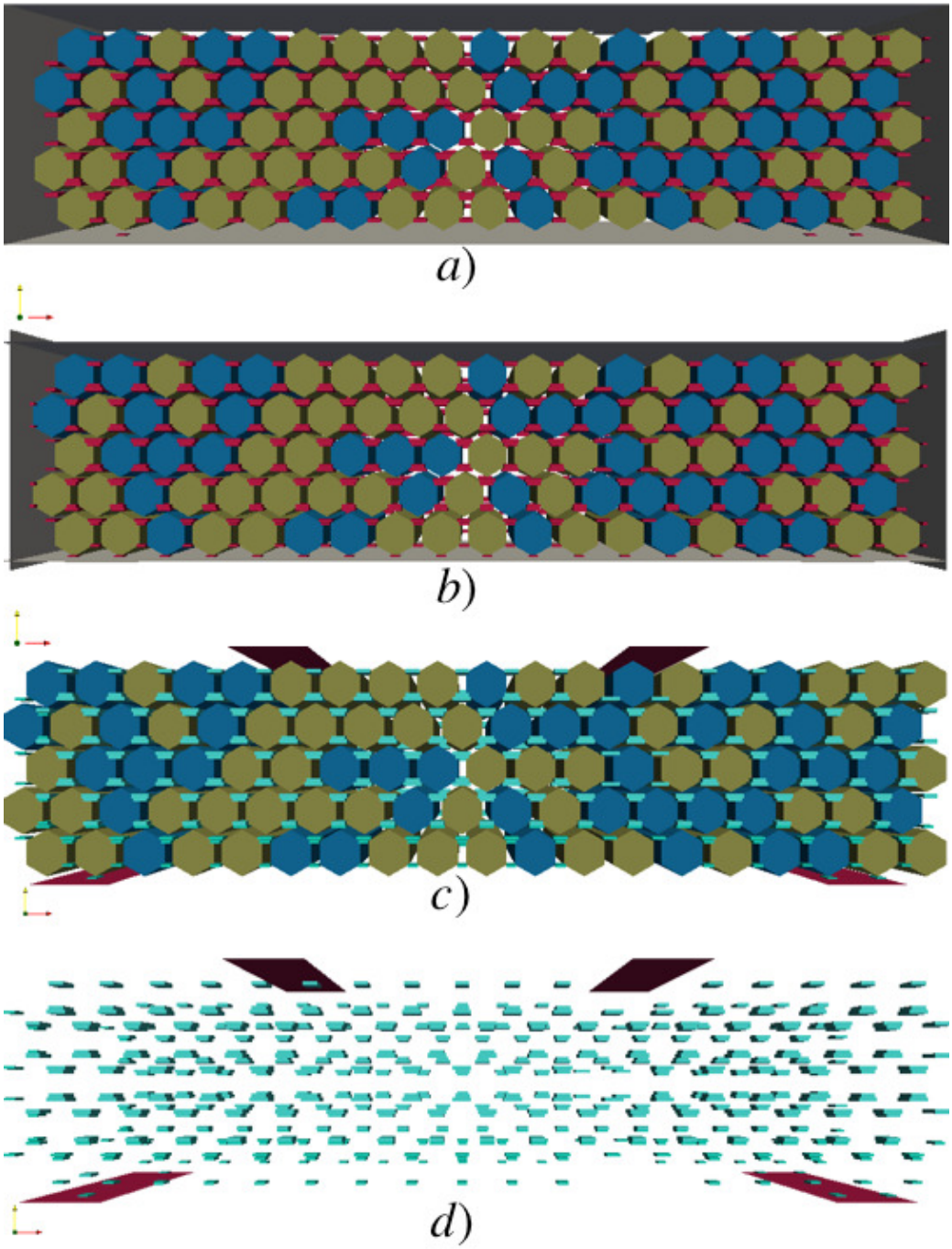

Figure 2.20

Four-point bending test consisting of 95 polyhedral particles at a) Initial configuration, b) after 1500 time steps when initial contacts (red beams) between particles were achieved, c) initialization of bonds and d) depiction of bonded contacts in blue.

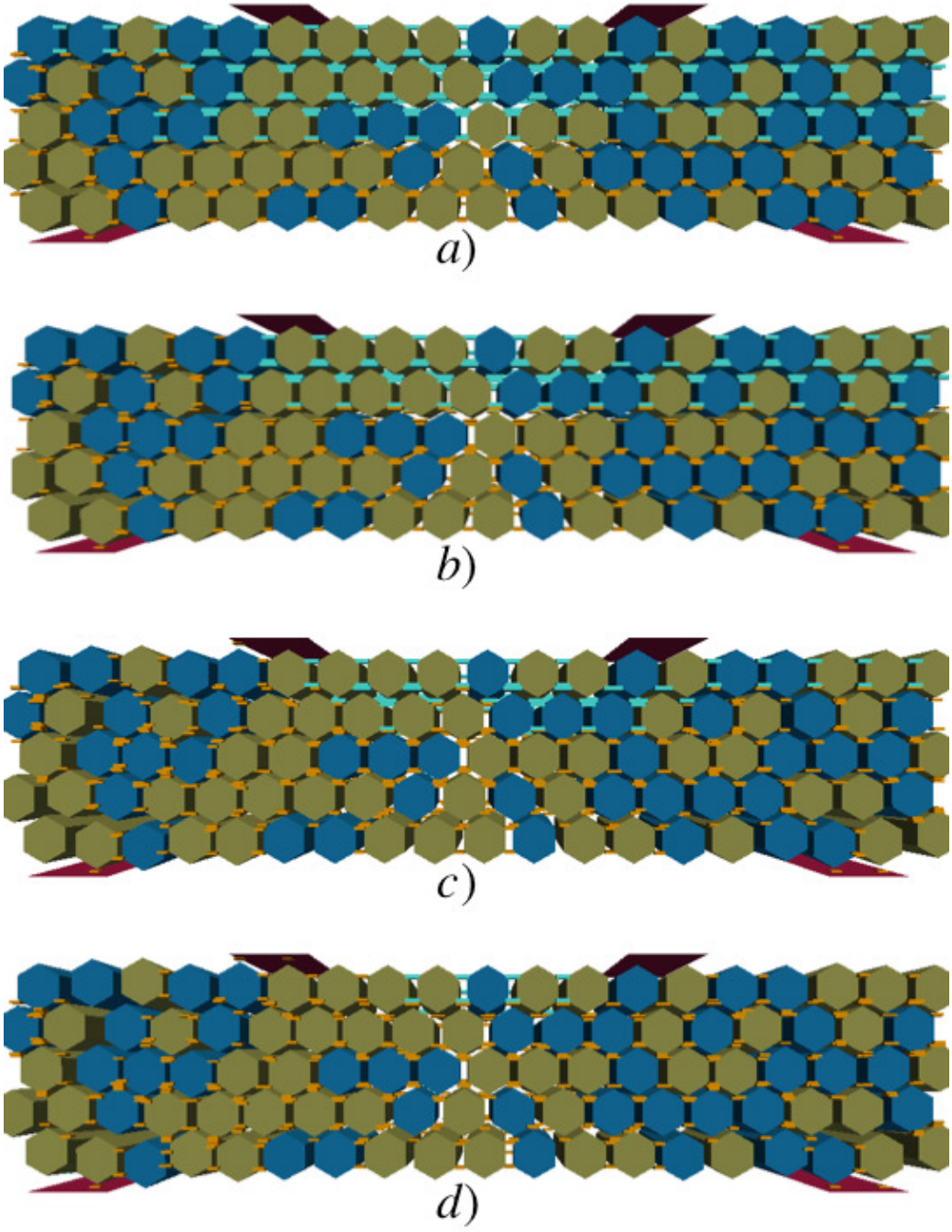

Figure 2.21

Four-point bending test consisting of 95 polyhedral particles at a) after 150 time steps, b) after 250 time steps, c) after 400 time steps d) after 500 time steps

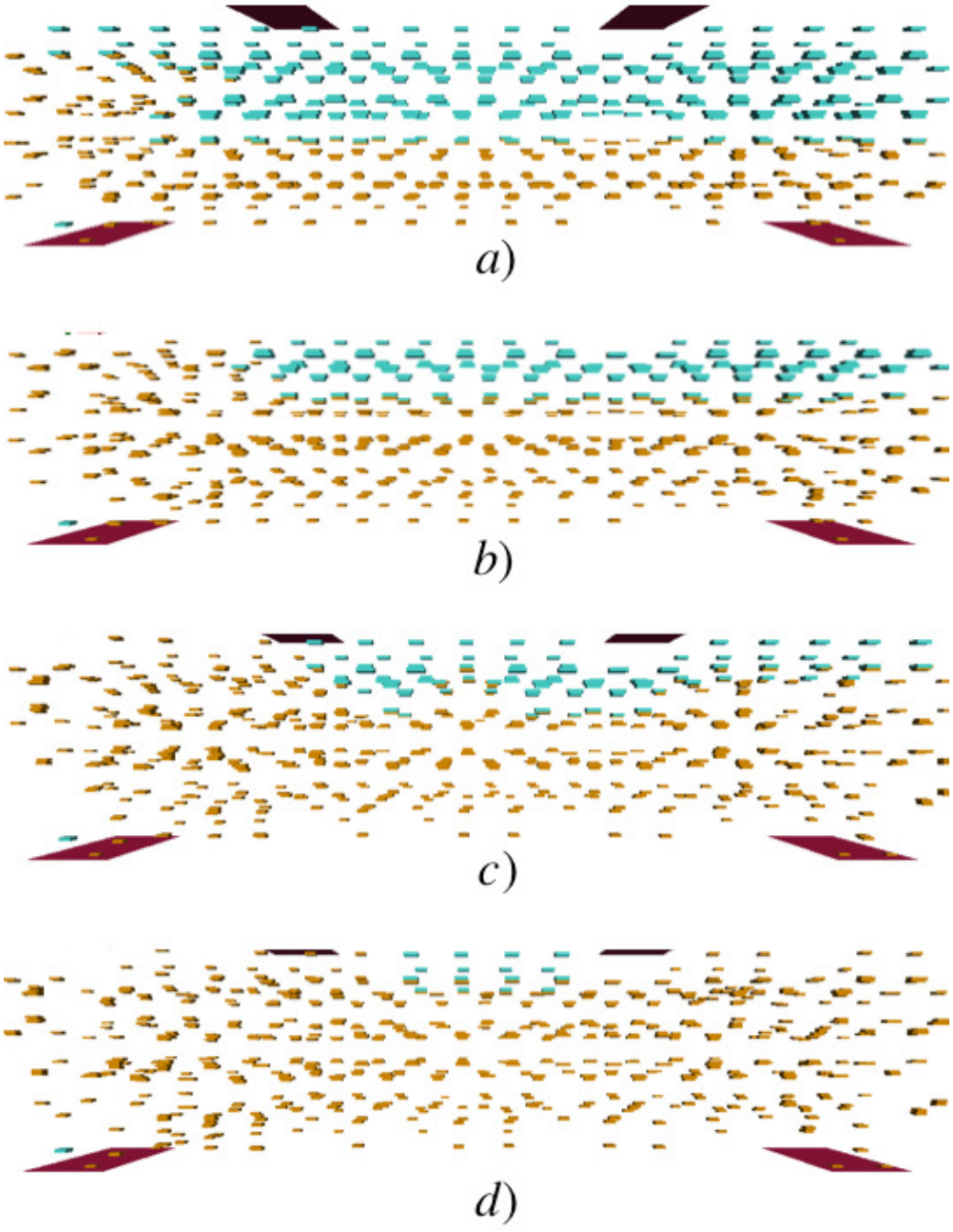

Figure 2.22

Four-point bending test with bonded and broken contacts at a) after 150 time steps, b) after 250 time steps, c) after 400 time steps d) after 500 time steps

Table 2.5

DEM bonding parameters used in four-point bending and Brazilian tests

Bonding Input Parameters	Values
Bond normal stiffness, K_{bn}	5000
Bond shear stiffness, K_{bs}	2000
Bond normal "tensile" strength, t_{bn}	1000
Bond shear strength, t_{bs}	1000

compression, with a compressive stress in the direction of loading and tensile stress in the direction perpendicular to that of the loading [31]. The magnitude of maximum tensile stress is given by:

$$\sigma = \frac{2P}{\pi D t}$$

where P is the load, D is the diameters of the disk and t is the thickness.

For the brazilian test, a single plane model consisting of 187 polyhedral particles, resulting in model specimen size $15\ mm \times 15\ mm \times 5\ mm$ was generated as described in Section 2.2.2. The parameters used in the initial DEM simulation are included in Table **??**. To make particles in contact with each other from the beginning of the simulation, the bonding distance parameter was set to $0.08\ mm$. This allows a reduction on the simulation time. To make the plates be in contact with the particles at the boundary, loading velocities of $400\ mm/s$, $-1000\ mm/s$ to the top and bottom plates respectively. Then, initialization of the bonds was performed. Finally, uniaxial loading was applied to the circular specimen by moving the top and bottom plates at a loading velocity of $0.001\ mm/s$ as shown in Figure 2.23a). Corresponding depiction, at the beginning of the simulation, of the bonded contacts (represented by green beams) and depiction of unbonded contacts (represented by

red beams) is shown Figure 2.23b). Evolution of bond breakage at time steps 300 and 500 are shown in Figure 2.23c) and Figure 2.23e) with corresponding depiction of bonded and unbonded contacts in Figure 2.23d) and Figure 2.23f) respectively. In this simulation the bonding parameters were all set as described in Table **??**. A dilation radii of $0.05\ mm$ was used for detection of contacts.

Particles stresses for the Brazilian test simulation are depicted using POVRAY. Blue colored particles have lower stresses, red colored particles have higher stresses. For a single crystal the average stresses are compressive. If we simulate the cylinder with multiple crystals, we begin to see tensile cracks. When looking at the specimen in detail (as in Figure 2.24c)) we observed the crystals form compressive wedges where contact is made with the top and bottom plates (no depicted in the figure) that forces the particles in the central part of the specimen apart. In the limit where the crystals become vanishingly small and infinitely numerous, this wedge in the contact zone will likewise diminish to zero size, leaving the entire central part of the specimen in tension. In this limit, the contact points are singularities that support infinite compression, thus balancing the tensile stress formed in the remainder of the specimen [102].

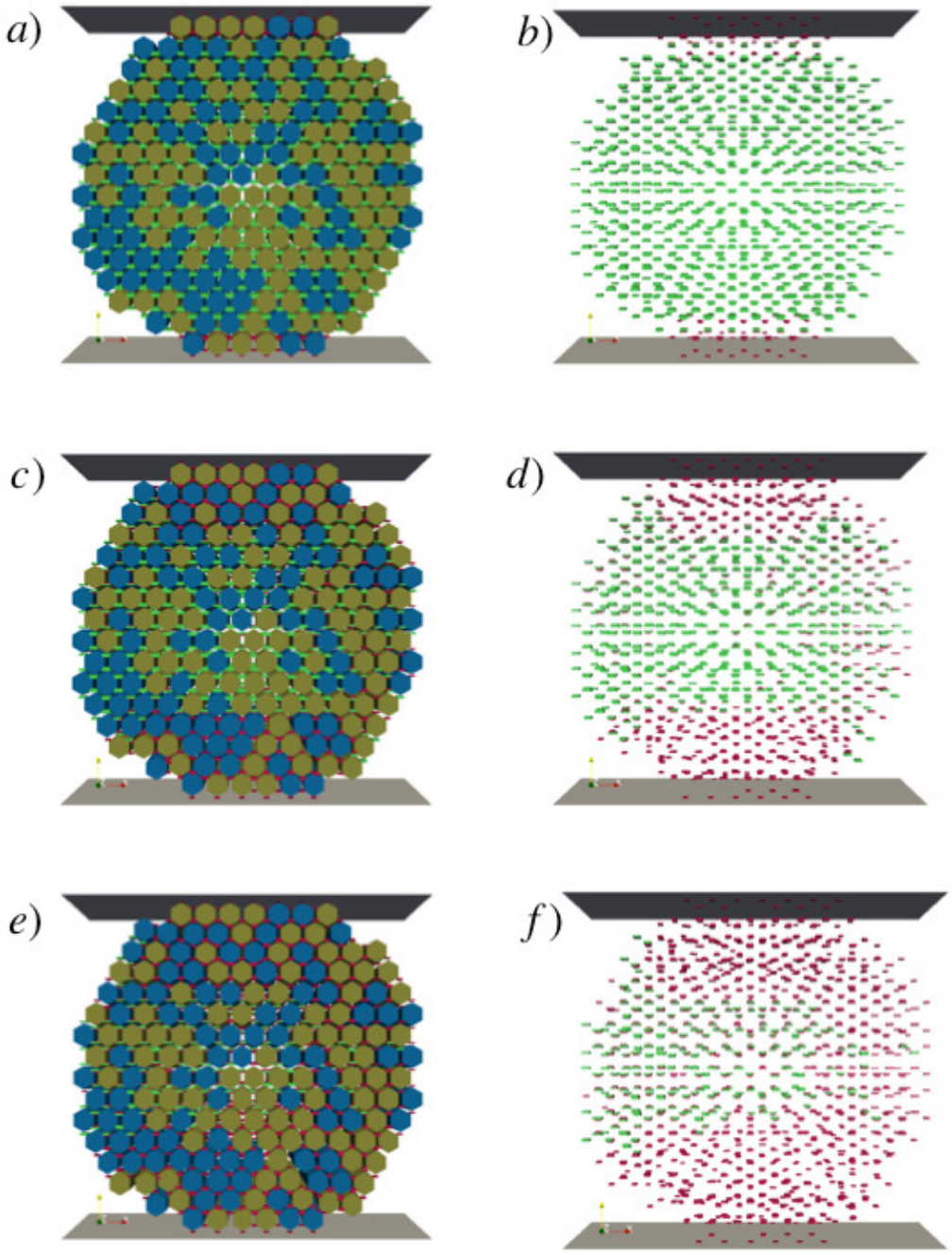

Figure 2.23

Four-point bending test with bonded and broken contacts at a) after 150 time steps, b) after 250 time steps, c) after 400 time steps d) after 500 time steps

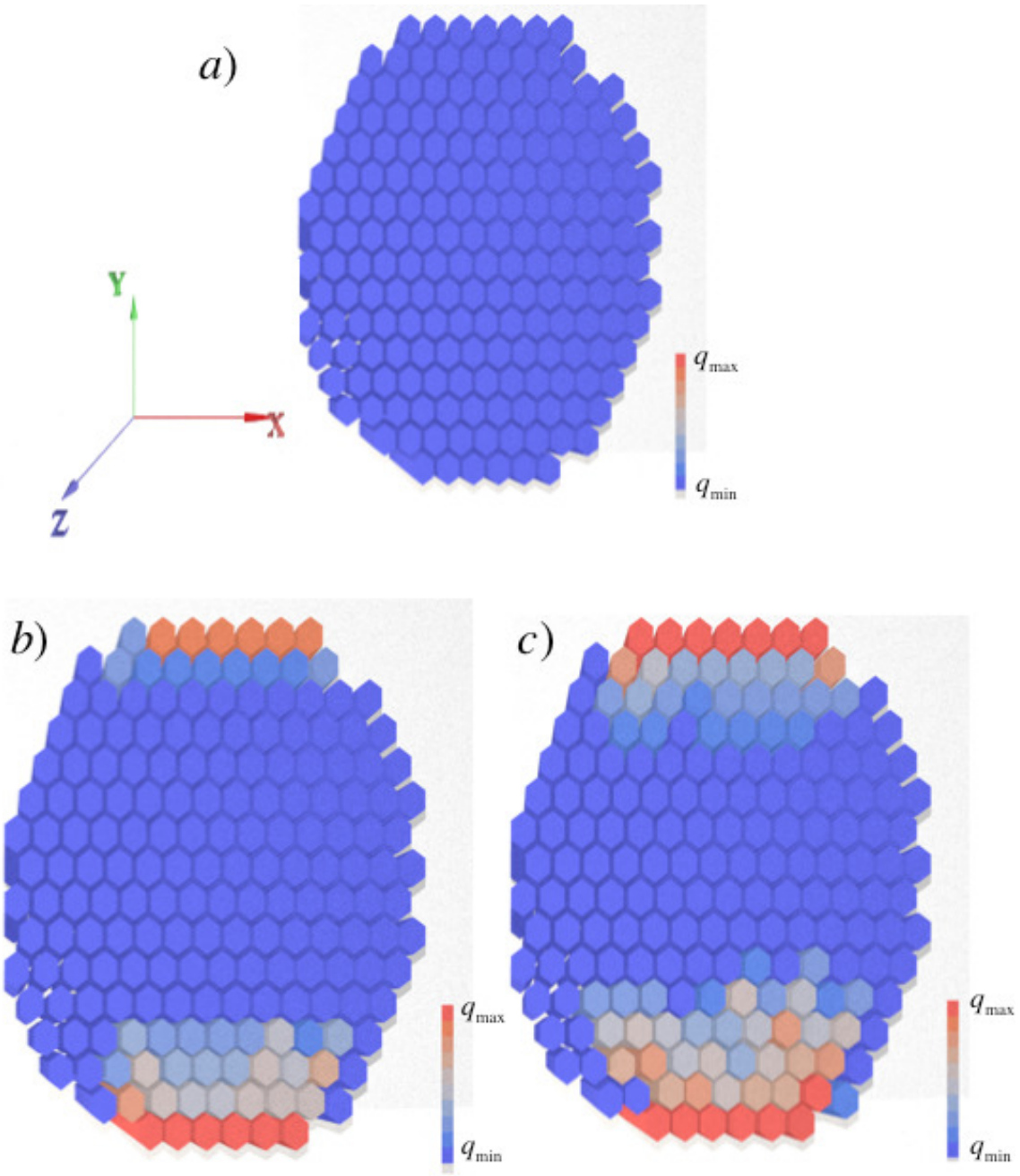

Figure 2.24

Particles stresses for the Brazilian test simulation: a) at time step 0, b) at time step 300 and c) at time step 500. Blue colored particles have lower stresses, red colored particles have higher stresses

CHAPTER 3

TRANSGRANULAR FRACTURE MODELING BASED ON DEM

3.1 Introduction

Performance of polycrystalline materials is to a large extent governed by their microstructure and its evolution under deformation [99]. In these materials, crack propagation can be intergranular (along the grain boundaries) or transgranular (through the grains) as depicted in Figure 1.3. Fracture is generally intergranular at very fine grain sizes but transgranular as the grain size increases. The transgranular fracture occurs if the grain is in a favorable orientation for cleavage.

Since the microstructure of polycrystalline ceramics consist of crystal particles and pores, the ceramic bulk can be treated as an assemblage of discrete particles bonded together randomly. Furthermore, the intergranular fracture of ceramics can be naturally represented by the separation of particles due to breakage of bonds, and the transgranular fracture of ceramics can be represented by the fragmentation of particles due to high stresses acting on the particles.

In this chapter, a transgranular fracture model is presented based on the discrete element method. Fracture within the grains will be performed by replacing a grain (an intact discrete element) with a fractured one (with two intact discrete elements bounded by a fractured surface). The fracture criteria is based on the continuous traction parameters

described in terms of the discrete forces by using the principle of virtual work. The computation of the traction parameters is explained in Section 3.2.

For the fracture of a single discrete element , tractions are computed on all facets of the discrete element . Then by using the equilibrium condition, the tractions are calculated on potential fracture planes at a specified spacing within the discrete element based on its crystallographic orientation. When the fracture criteria is met, the discrete element is separated into two discrete elements along the fracture plane. Two discrete elements created from the fracture of a single discrete element are illustrated in Figure 3.1.

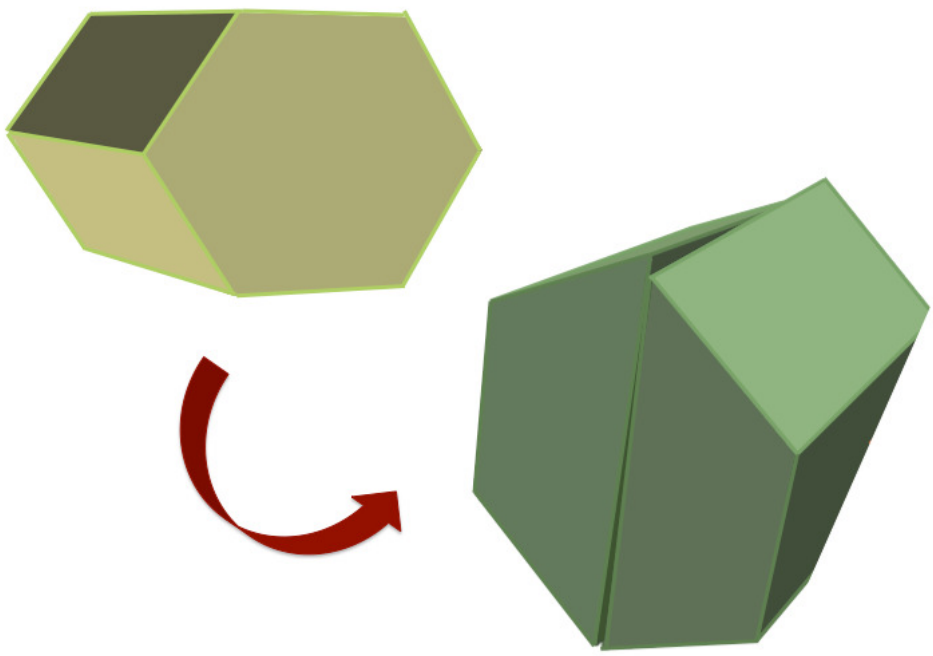

Figure 3.1

A discrete element and its corresponding fragments after transgranular fracture

3.2 Consistent Traction Formulation for Discrete Elements

In a DEM system all compliance occurs at the interface between discrete elements. In this section consistent tractions at the interface between discrete elements are defined to facilitate modeling large discontinuous deformation such as when materials fracture. Two pair of discrete elements in contact are illustrated in Figure 3.2. Prior to fracture, these elements approximate the continuous medium; after fracture, the elements naturally model the collection of interacting fragments. The inter-element continuity at the interface between two discrete finite elements is approximated by contact laws that are usually defined by elastic springs for an unfractured interface. The spring constants are chosen such that the assemblage of elements displays the correct elastic response for the continuum body represented by the assemblage. When the fracture criteria is met at the interface, the elastic contact laws are replaced by a frictional contact with compressive-only normal forces. For both pre-fracture and post-fracture, the kinetics at the interface are defined by discrete forces.

A relationship is derived between the pre-fractured discrete contact forces and the continuous tractions that are assumed to exist across the interfaces. The creation of a fracture between two preexisting discrete elements is straightforward because the element boundary coincides with the fracture plane. For example, element boundaries are useful for modeling grain boundaries in polycrystalline materials. However, where the grains themselves fracture, a criteria for fracture must be included in the model and this is developed in the following section 3.3.

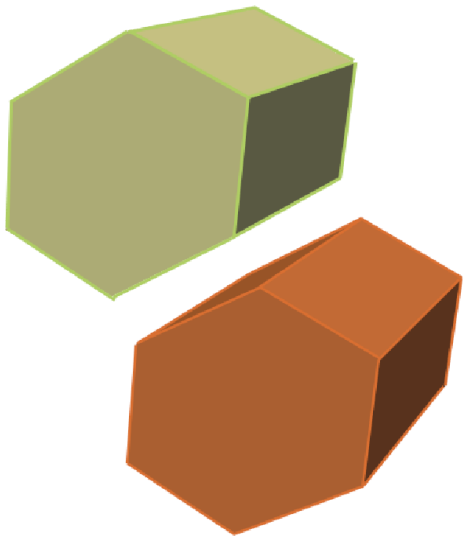

Figure 3.2

Pair of polyhedra-shaped discrete elements

Equivalence between the contact forces (Figure 3.3) and the tractions at the particle's boundary faces (Figure 3.4) is established by using the principle of virtual work, which allows the computations of the tractions that are consistent with the contact forces in the sense that they yield the same virtual work in response to an arbitrary virtual deformation. Since we are dealing with a dynamic system of particles, we apply D'Alembert's principle, a form of Newton's second law, which states that the resultant of the external forces F and the kinetic reaction acting on a body equals zero ($\sum_{n=1}^{N_c} F^n - ma = 0$). For simplicity, gravity is considered to be zero.

In this section, we presented a formulation to compute the consistent tractions at each of the boundary faces of a discrete element which is assumed to be in contact at each of its faces with other discrete elements.

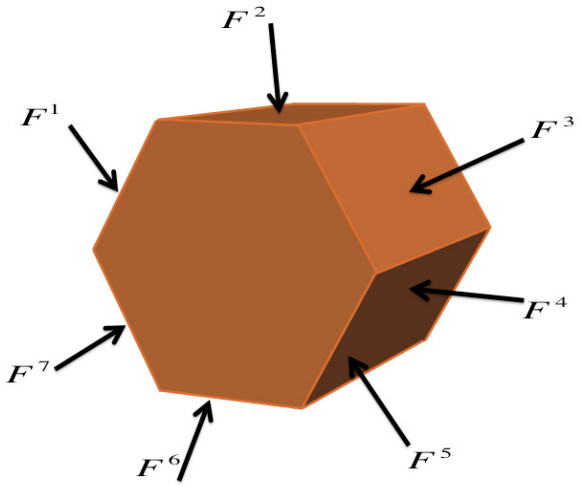

Figure 3.3

Discrete forces acting on a discrete element

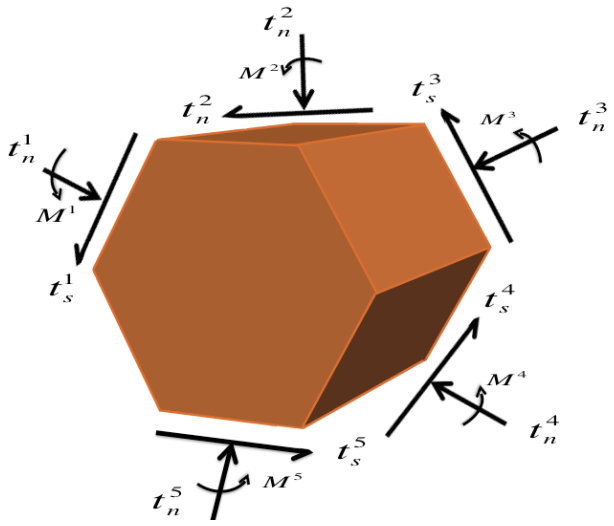

Figure 3.4

Tractions on the discrete element's boundary faces

3.2.1 Coordinate System

Two types of coordinate systems are considered in this work. A global coordinate system (GCS) as defined within DEM (X, Y, Z) to describe the discrete elements collective motions. The global coordinate system is a left-handed coordinate system, where the Z axis acts in the gravitational direction, as shown in Figure 3.5. Local coordinate systems (LCS) (x_i, y_i, z_i) are also defined where i represents the face number, to describe the mechanism involved at each of the discrete elements boundary faces. These local coordinate systems are aligned such that x_i axes and y_i axes lie in the plane face and z_i axes are directed normal to the face i of the discrete element. These directions coincide with the sliding and separation that occurs on these surfaces and are shown in Figure 3.6.

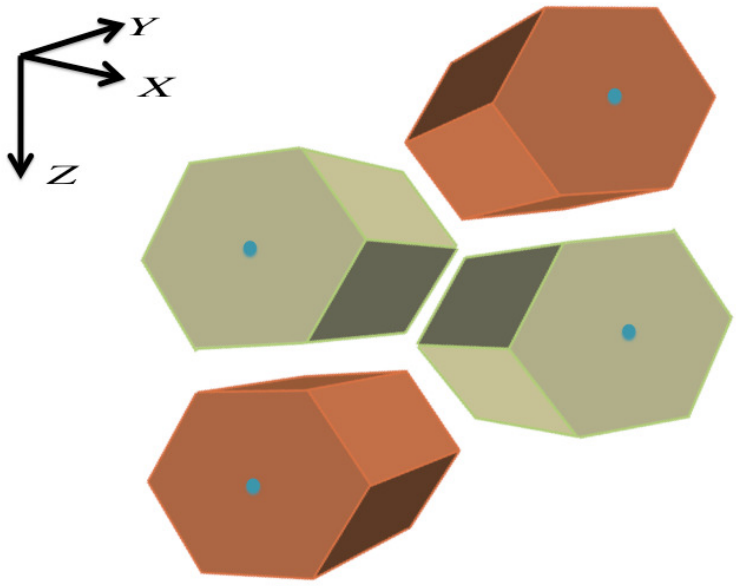

Figure 3.5

Global Coordinate System (GCS)

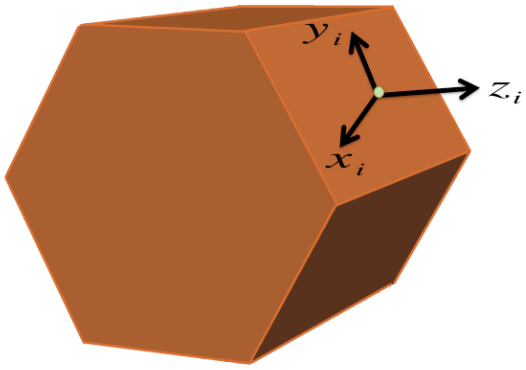

Figure 3.6

Local Coordinate System (LCS) for one of the boundary faces of a discrete element

The tractions are computed in the LCS from the discrete forces acting at each discrete element boundary faces. Also, it is assumed that the x_i- and y_i- axes are placed at the centroid of the boundary face.

3.2.2 Force Vector Coordinate Transformation

The first step in computing the tractions at each discrete element face is to take the discrete forces acting at each face and transform them from the GCS (Figure 3.7) to the corresponding LCS (Figure 3.12).

Suppose $\mathscr{G} = \{\vec{e_1}, \vec{e_2}, \vec{e_3}\}$ is a base for the GCS and $\mathscr{L} = \{\vec{l_1}, \vec{l_2}, \vec{l_3}\}$ is a base for the LCS at one of the faces.

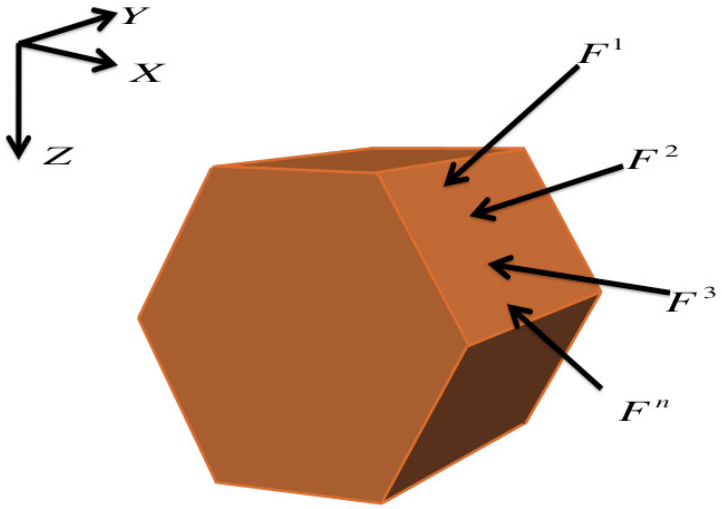

Figure 3.7

Forces in the global system

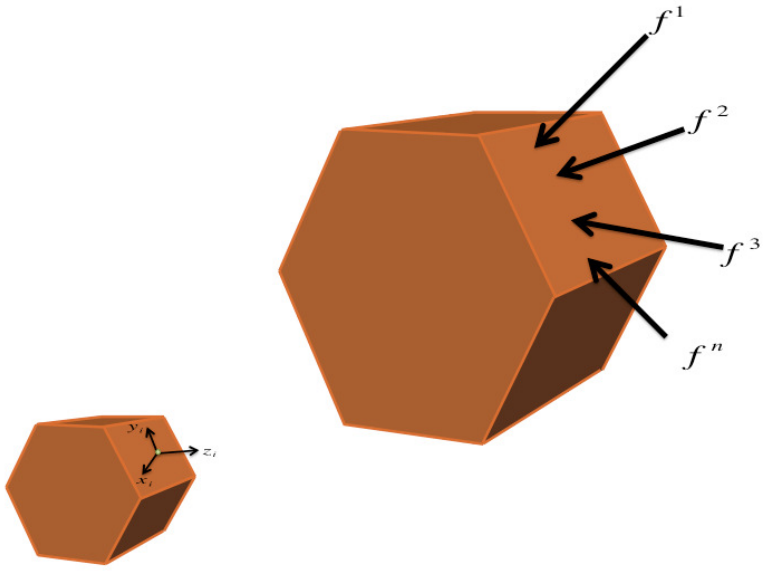

Figure 3.8

Forces in the local system

$$\vec{e_1} = \begin{bmatrix} 1 \\ 0 \\ 0 \end{bmatrix}, \quad \vec{e_2} = \begin{bmatrix} 0 \\ 1 \\ 0 \end{bmatrix}, \quad \vec{e_3} = \begin{bmatrix} 0 \\ 0 \\ -1 \end{bmatrix} \tag{3.1}$$

$$\vec{l_1} = \begin{bmatrix} x_1 \\ y_1 \\ z_1 \end{bmatrix}, \quad \vec{l_2} = \begin{bmatrix} x_2 \\ y_2 \\ z_2 \end{bmatrix}, \quad \vec{l_3} = \begin{bmatrix} x_3 \\ y_3 \\ z_3 \end{bmatrix} \tag{3.2}$$

Each vector of the base $\mathscr{G}$ can be expressed as a linear combination of the elements of the base $\mathscr{L}$:

$$\vec{e_i} = a_i\vec{l_1} + b_i\vec{l_2} + c_i\vec{l_3}, \qquad i = 1, 2, 3 \tag{3.3}$$

where values for $\{a_i, b_i, c_i\}$ are found by solving the linear systems

$$\begin{bmatrix} x_1 & x_2 & x_3 \\ y_1 & y_2 & y_3 \\ z_1 & z_2 & z_3 \end{bmatrix} \begin{bmatrix} a_i \\ b_i \\ c_i \end{bmatrix} = \vec{e_i}, \qquad i = 1, 2, 3 \tag{3.4}$$

Therefore, a vector $\vec{F} = [F_1, F_2, F_3]$ in the global coordinate system, can be transformed into a vector in the local coordinate system by using the following expression:

$$\vec{F} = (F_1a_1 + F_2a_2 + F_3a_3)\vec{l_1} + (F_1b_1 + F_2b_2 + F_3b_3)\vec{l_2} + (F_1c_1 + F_2c_2 + F_3c_3)\vec{l_3} \tag{3.5}$$

3.2.3 Kinematics

The kinematics describe the relative motion between two adjacent discrete elements in the LCS. The location of a point in a discrete element relative to the centroid of the face (x_0, y_0, z_0), to which the point belongs to, can be expressed as

$$\begin{aligned} x &= x_0 + R\cos(\omega) \\ y &= y_0 + R\sin(\omega), \\ z &= z_0 + h_{zx}\sin\theta_x + h_{zy}\sin\theta_y \end{aligned} \tag{3.6}$$

where θ_x, θ_y are the relative rotations with respect to the x-axis, y-axis respectively, and ω is the relative rotation about the z-axis as shown in Figure 3.9, Figure 3.10 and Figure 3.11 respectively.

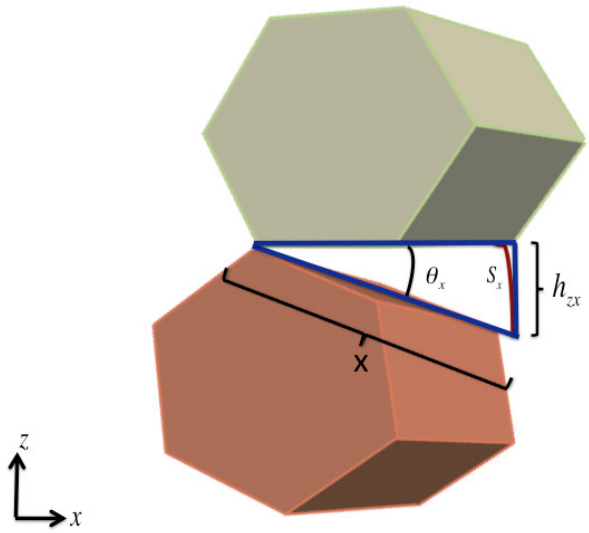

Figure 3.9

Relative rotation about x- axis (θ_x)

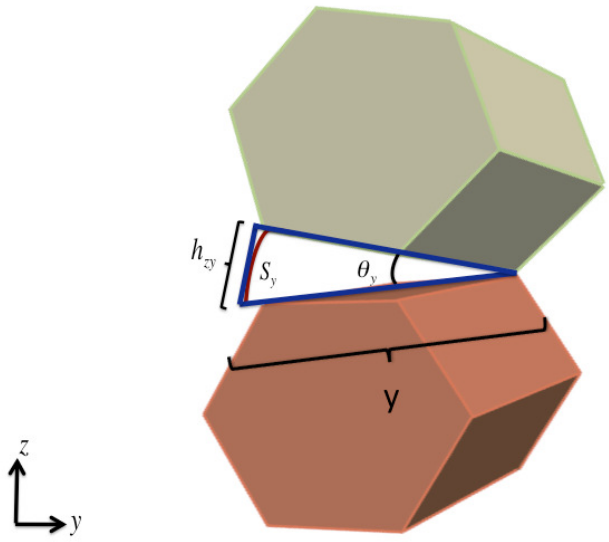

Figure 3.10

Relative rotation about y- axis (θ_y)

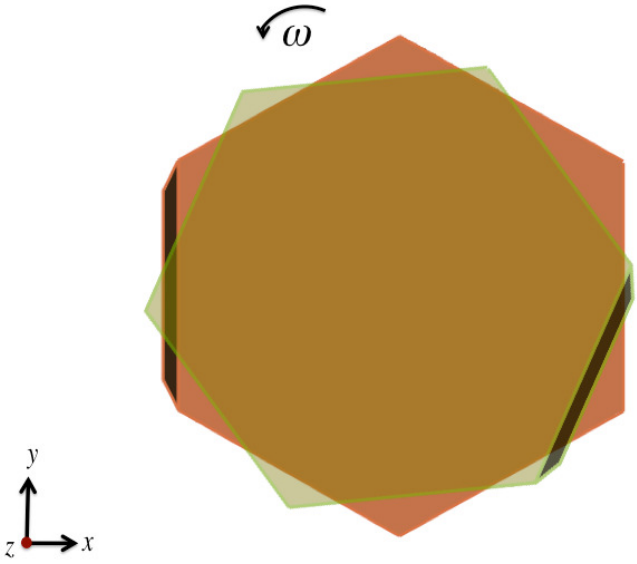

Figure 3.11

Relative rotation about z-axis (ω)

Assuming a small angle approximation, the arc lengths S_x and S_y representing the relative rotations about the x-axis and y-axis, are approximately equal to h_{zx}, h_{zy}, respectively, as shown in Figure 3.9 and Figure 3.10. The motion of a discrete element consists of in-plane movements, δu and δv, and the out-of-plane separation motion normal to the interface plane, δw. Thus, the motion of a particular point (x, y, z) in a discrete element is given in terms of its rigid body motions (δu, δv, δw) and the relative rotations between the contacting surfaces ($\delta\omega$, $\delta\theta_x$, $\delta\theta_y$) as,

$$\begin{aligned} \delta u &= \delta u_o - R\sin(\omega)\delta\omega = \delta u_o - y\delta\omega \\ \delta v &= \delta v_o + R\cos(\omega)\delta\omega = \delta v_o + x\delta\omega \\ \delta w &= \delta w_o + h_{zx}\cos(\theta_x)\delta\theta_x + h_{zy}\cos(\theta_y)\delta\theta_y = \delta w_o + x\delta\theta_x + y\delta\theta_y \end{aligned} \tag{3.7}$$

Note that although $\delta u_o, \delta v_o, \delta w_o$ are constant motion acting across the boundary plane, they are not to be confused with rigid-body motions ($\delta u, \delta v, \delta w$) because they represent motion of one discrete element face relative to the other. These relative displacements are in the x, y, and z directions measured with respect to a convenient location between two contacting surfaces

3.2.4 Virtual Work Principle (VWP)

In this section, the virtual work done by the forces (computed from the contact force laws) acting on the contacting surface is equated to the virtual work done by a set of hypothetical consistent tractions that act uniformly on the surface. To accomplish this, an equivalence between the motions at any particular point on the surface and uniformly varying motions that are thermodynamic conjugates of the tractions is set up.

3.2.4.1 VWP for Discrete Forces

Due to the rigidity of the discrete element, only six kinematics variables $\delta u_o, \delta v_o, \delta w_o$, $\delta\theta_x, \delta\theta_y, \delta\omega$ are required to describe the virtual work done by the forces acting on each the discrete element's face. Suppose there are N_c forces acting on one of the faces, $\mathbf{F}^1, ..., \mathbf{F}^{N_c}$ which are expressed in global coordinates. First, each of those forces has to be transformed to the local coordinate system corresponding to the face they act on. This is done by using Equation (3.5). Thus, we get N_c forces, $\mathbf{f}^1, ..., \mathbf{f}^{N_c}$, in the local coordinate system acting on the face, as shown in Figure 3.12. Next, from the D'Alembert's principle $\sum_{n=1}^{N_c} f^n - ma = 0$, ($m$ and a are the discrete element's mass and acceleration respectively), and the principle of virtual work, the total work done by the forces is:

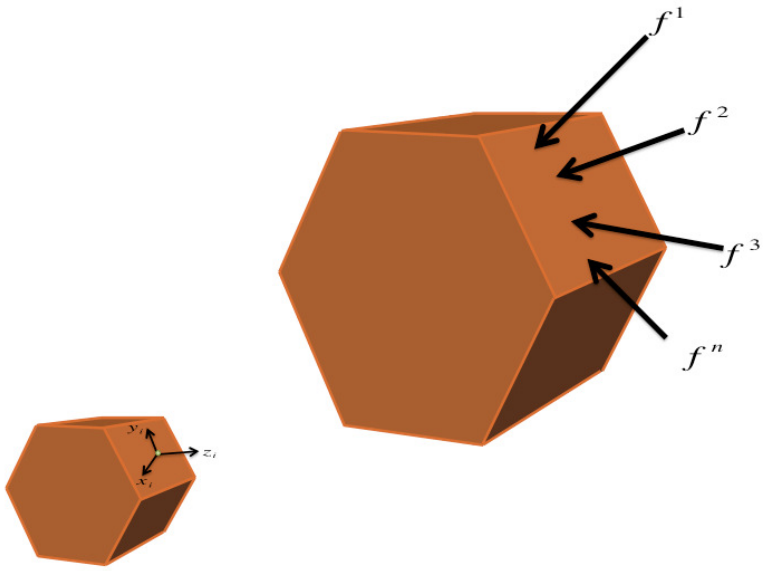

Figure 3.12

$N_c = n$ Discrete forces acting on a discrete element boundary face

$$
\begin{aligned}
\delta W &= \left(\sum_{n=1}^{N_c} f^n - ma\right)\delta U \\
&= \left(\sum_{n=1}^{N_c} f_x^n - ma_x\right)\delta u + \left(\sum_{n=1}^{N_c} f_y^n - ma_y\right)\delta v + \left(\sum_{n=1}^{N_c} f_z^n - ma_z\right)\delta w \\
&\quad + \left(\sum_{n=1}^{N_c} f_x^n - ma_x\right)(\delta u_o - y\delta\omega) + \left(\sum_{n=1}^{N_c} f_y^n - ma_y\right)(\delta v_o + x\delta\omega) \\
&\quad + \left(\sum_{n=1}^{N_c} f_z^n - ma_z\right)(\delta w_o + x\delta\theta_x + xy\delta\theta_y) \\
&= \left(\sum_{n=1}^{N_c} f_x^n - ma_x\right)\delta u_o + \left(\sum_{n=1}^{N_c} f_y^n - ma_y\right)\delta v_o + \left(\sum_{n=1}^{N_c} f_z^n - ma_z\right)\delta w_o \\
&\quad + \left(\sum_{n=1}^{N_c} f_z^n - ma_z\right)x\delta\theta_x + \left(\sum_{n=1}^{N_c} f_z^n - ma_z\right)y\delta\theta_y \\
&\quad + \left[x\left(\sum_{n=1}^{N_c} f_y^n - ma_y\right) - y\left(\sum_{n=1}^{N_c} f_x^n - ma_x\right)\right]\delta\omega
\end{aligned}
\tag{3.8}
$$

3.2.4.2 VWP for Continuous Tractions

Next, the tractions acting on each face of the discrete element are defined in terms of the discrete forces acting on each face. The shear tractions, t_x and t_y, acting on the plane with area *A* of the boundary face are assumed to be constant, whereas the normal stress,

t_n, is assumed to have a linear distribution. Therefore, the tractions acting on the plane S (Figure 3.13) are:

$$\begin{aligned} t_n &= t_o + C_1 x + C_2 y \\ t_s &= \sqrt{t_x^2 + t_y^2} \\ t_x, t_y &= constants \end{aligned} \tag{3.9}$$

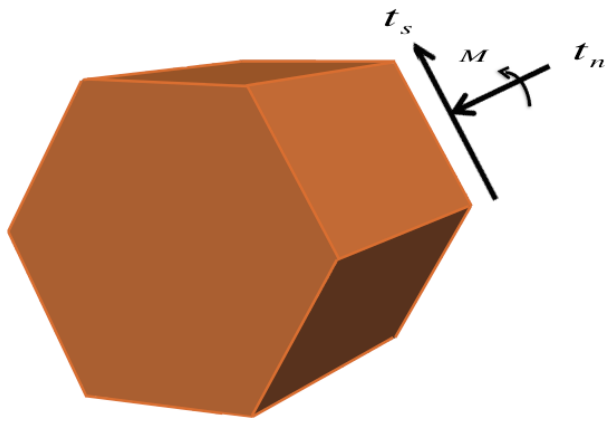

Figure 3.13

Tractions acting on a discrete element boundary face

Thus, the virtual work done by the tractions is

$$\begin{aligned}
\delta W &= \int_A [t_x \delta u + t_y \delta v + t_n \delta w] dA \\
&= \int_A [t_x(\delta u_o - y\delta\omega) + t_y(\delta v_o + x\delta\omega) + t_n(\delta w_o + x\delta\theta_x + y\delta\theta_y)] dA \\
&= \int_A [(\delta u_o - y\delta\omega)t_x + (\delta v_o + x\delta\omega)t_y + (\delta w_o + x\delta\theta + y\delta\theta)t_n] dA \\
&= \left(\int_A t_x dA\right) \delta u_o + \left(\int_A t_y dS\right) \delta v_o + \left(\int_A t_n dA\right) \delta w_o + \left(\int_A x t_n dA\right) \delta\theta_x \\
&\quad + \left(\int_A y t_n dA\right) \delta\theta_y + \left(\int_A (x t_y - y t_x) dA\right) \delta\omega
\end{aligned} \tag{3.10}$$

where A is the face's surface area for which tractions are being computed.

The virtual work equality is set up such that the work done by the discrete forces, moments, displacements and rotations for the contacts (Equation (3.8)) is at one side of the equation and the work done by the uniform motions and the tractions (Equation (3.10)) is on the other side of the equation. Because the virtual motions are independent and arbitrary, the equality of virtual work in Equation (3.8) and Equation (3.10) must be maintained for all values of virtual displacements and rotations. The equality is insured by making each expression multiplying a virtual kinematic variable in Equation (3.8) to be equal to the expression multiplying the respective virtual kinematic variable in Equation (3.10).

Therefore, we obtain:

$$
\begin{aligned}
\int_A t_x dA &= \left(\sum_{n=1}^{N_c} f_x^n - m a_x \right) \\
\int_A t_y dA &= \left(\sum_{n=1}^{N_c} f_y^n - m a_y \right) \\
\int_A t_n dA &= \left(\sum_{n=1}^{N_c} f_z^n - m a_z \right) \\
\int_A x t_n dA &= x \left(\sum_{n=1}^{N_c} f_z^n - m a_z \right) \\
\int_A y t_n dA &= y \left(\sum_{n=1}^{N_c} f_z^n - m a_z \right) \\
\int_A (x t_y - y t_x) dA &= x \left(\sum_{n=1}^{N_c} f_y^n - m a_y \right) - y \left(\sum_{n=1}^{N_c} f_x^n - m a_x \right)
\end{aligned}
\tag{3.11}
$$

After substituting the linear relationship for t_n we obtain

$$\begin{aligned}
\int_A t_x dA &= \left(\sum_{n=1}^{N_c} f_x^n - ma_x \right) \\
\int_A t_y dA &= \left(\sum_{n=1}^{N_c} f_y^n - ma_y \right) \\
\int_A (t_o + C_1 x + C_2 y) dA &= \left(\sum_{n=1}^{N_c} f_z^n - ma_z \right) \\
\int_A (x t_o + C_1 x^2 + C_2 xy) dA &= x \left(\sum_{n=1}^{N_c} f_z^n - ma_z \right) \\
\int_A (y t_o + C_1 xy + C_2 y^2) dSA &= y \left(\sum_{n=1}^{N_c} f_z^n - ma_z \right) \\
\int_A (x t_y - y t_x) dA &= x \left(\sum_{n=1}^{N_c} f_y^n - ma_y \right) - y \left(\sum_{n=1}^{N_c} f_x^n - ma_x \right)
\end{aligned} \tag{3.12}$$

From the above Equation (3.12), we define the following quantities:

$$\begin{aligned}
A &= \int_A dA & Q_y &= \int_A x dA \\
Q_x &= \int_A y dA & M_z &= \int_A (x t_y - y t_x) dA \\
I &= \begin{pmatrix} I_{xx} & I_{xy} \\ I_{xy} & I_{yy} \end{pmatrix} & I_{ab} &= \int_A (ba) dA; \qquad a, b = x, y
\end{aligned} \tag{3.13}$$

where Q_x is the first moment of area about x axis, Q_y is the first moment of area about y axis, I is the second moment of area and M_z, is the moment about z axis; it is sometimes referred as T, is the torque acting on the plane of the surface. Therefore, the parameters $t_o, C_1, C_2, t_x, t_y, M_z$ can be expressed in terms of the discrete forces acting on a discrete element as follows:

$$
\begin{aligned}
t_x &= \frac{1}{A}\left(\sum_{n=1}^{N_c} f_x^n - ma_x\right) \\
t_y &= \frac{1}{A}\left(\sum_{n=1}^{N_c} f_y^n - ma_y\right) \\
t_o A + C_1 Q_y + C_2 Q_x &= \left(\sum_{n=1}^{N_c} f_z^n - ma_z\right) \\
t_o Q_y + C_1 I_{xx} + C_2 I_{xy} &= x\left(\sum_{n=1}^{N_c} f_z^n - ma_z\right) \\
t_o Q_x + C_1 I_{xy} + C_2 I_{yy} &= y\left(\sum_{n=1}^{N_c} f_z^n - ma_z\right) \\
M_z &= x\left(\sum_{n=1}^{N_c} f_y^n - ma_y\right) - y\left(\sum_{n=1}^{N_c} f_x^n - ma_x\right)
\end{aligned}
\tag{3.14}
$$

where explicit expressions for t_o, C_1 and C_2 are found by solving the system of equations from Equation (3.14) $c) - e)$:

$$\underbrace{\begin{bmatrix} A & Q_y & Q_x \\ Q_y & I_{xx} & I_{xy} \\ Q_x & I_{xy} & I_{yy} \end{bmatrix}}_{K} \begin{bmatrix} t_o \\ C_1 \\ C_2 \end{bmatrix} = \begin{bmatrix} 1 \\ x \\ y \end{bmatrix} \left(\sum_{n=1}^{N_c} f_z^n - ma_z \right) \tag{3.15}$$

Note that the system of equations (3.14) $c) - e)$ is solvable since $\det(K) \neq 0$.

$$\begin{bmatrix} t_o \\ C_1 \\ C_2 \end{bmatrix} = \frac{1}{\det(K)} B \begin{bmatrix} 1 \\ x \\ y \end{bmatrix} \left(\sum_{n=1}^{N_c} f_z^n - ma_z \right) \tag{3.16}$$

where

$$B = \begin{bmatrix} \det(I) & Q_x I_{xy} - Q_y I_{yy} & Q_y I_{xy} - Q_x I_{xx} \\ Q_x I_{xy} - Q_y I_{yy} & A I_{yy} - (Q_x)^2 & Q_y Q_x - A I_{xy} \\ Q_y I_{xy} - Q_x I_{xx} & Q_y Q_x - A I_{xy} & A I_{xx} - (Q_y)^2 \end{bmatrix} \tag{3.17}$$

From the above, explicit expressions for the continuous tractions t_n, t_s and the torque M_z in terms of the discrete forces are found, as shown in Figure 3.14.

$$\begin{aligned} t_n &= t_o + C_1 x + C_2 y \\ t_s &= \sqrt{t_x^2 + t_y^2} \\ M_z &= x \left(\sum_{n=1}^{N_c} f_y^n - ma_y \right) - y \left(\sum_{n=1}^{N_c} f_x^n - ma_x \right) \end{aligned} \tag{3.18}$$

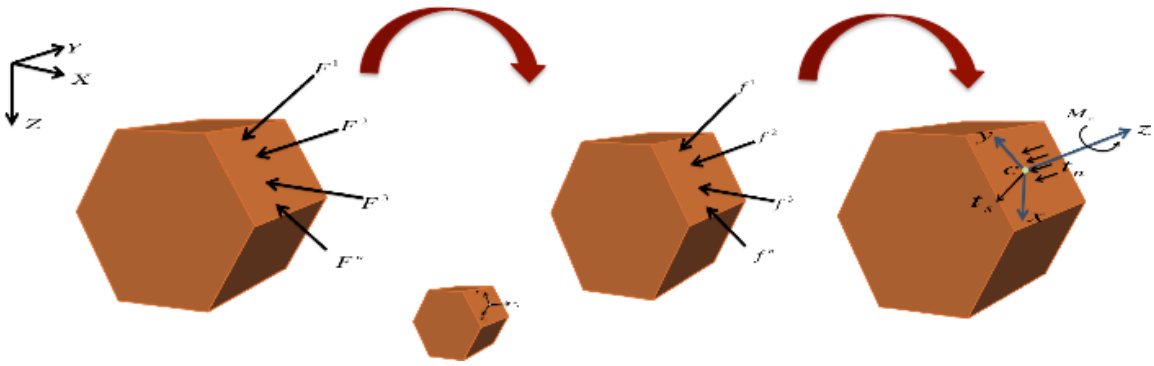

Figure 3.14

Steps to compute tractions from discrete forces

where

$$
\begin{aligned}
t_x &= \frac{1}{A}\left(\sum_{n=1}^{N_c} f_x^n - ma_x\right) \\
t_y &= \frac{1}{A}\left(\sum_{n=1}^{N_c} f_y^n - ma_y\right) \\
t_o &= \frac{\left(\sum_{n=1}^{N_c} f_z^n - ma_z\right)}{\det(K)}\left(\det(I) + x(Q_x I_{xy} - Q_y I_{yy}) + y(Q_y I_{xy} - Q_x I_{xx})\right) \\
C_1 &= \frac{\left(\sum_{n=1}^{N_c} f_z^n - ma_z\right)}{\det(K)}\left((Q_x I_{xy} - Q_y I_{yy}) + x(AI_{yy} - (Q_x)^2) + y(Q_y Q_x - AI_{xy})\right) \\
C_2 &= \frac{\left(\sum_{n=1}^{N_c} f_z^n - ma_z\right)}{\det(K)}\left((Q_y I_{xy} - Q_x I_{xx}) + x(Q_y Q_x - AI_{xy}) + y(AI_{xx} - (Q_y)^2)\right)
\end{aligned}
\tag{3.19}
$$

3.3 Consistent Tractions Formulation for 3D Fractured Discrete Elements

To compute the tractions at a potential fracture plane within the discrete element, the tractions at each of the boundary faces of the discrete element have to be computed from the discrete forces acting on them, as described in the previous Section 3.2 and shown in Figure 3.15. This smoothing step simplifies dealing with contact forces acting on crystal boundaries that are cut by fracture. Each set of tractions at each of the faces is described in the local coordinate system (x, y, z) defined for the face in which the tractions were computed.

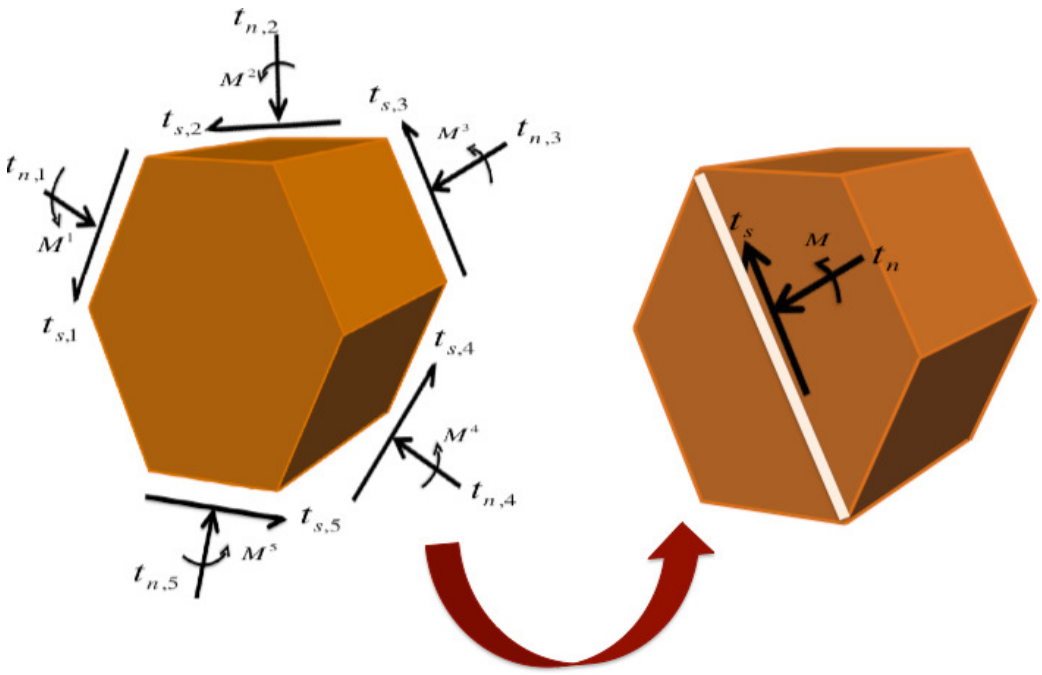

Figure 3.15

Transition from tractions at each particle's faces to tractions at potential crack plane

3.3.1 Tractions at Potential Crack Plane

To compute the tractions at a potential fracture plane, first the total force and total moment acting on each face have to be computed from the previously computed tractions acting on each face as shown in Figure 3.16 and Figure 3.17. the total force and total moment have to be transformed from the local coordinate system to the global coordinate system.

$$F^i = t_n^i * A^i * n^i + t_x^i * A^i * m^i + t_y^i * A^i * l^i \tag{3.20}$$

where $i = 1, ..., N_{faces}$, n^i, m^i and l^i are the normal and tangential vectors for face i respectively and A^i is the surface area of face i.

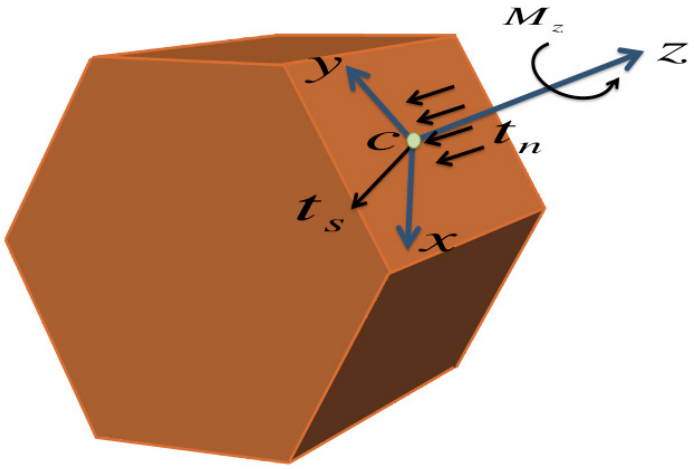

Figure 3.16

Tractions at one discrete element's face in the local coordinate system

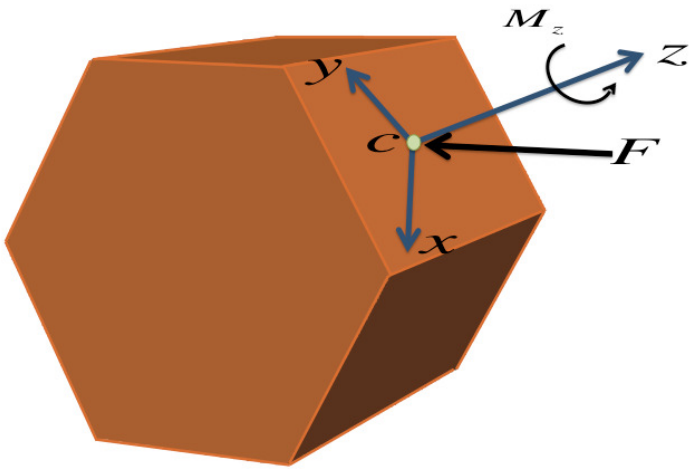

Figure 3.17

Total force and moment for discrete element's face in the global coordinate system

Next, the total forces and moments acting on each of the faces have to be transformed to the global coordinate system (X_g, Y_g, Z_g), since the tractions are defined in the corresponding local coordinate system. To accomplish this, we use the fact that distributed forces within a body can be represented by a statically equivalent system consisting of a force and a moment vector acing at the centroid of a section. Thus, the total force and total moment are computed at the centroid (described in the global coordinate system) for each of the fragments that will result if the discrete element fractures.

$$F_{centroid} = \sum_{i=1}^{N_{faces}} F^i$$

$$M_{centroid} = \sum_{i=1}^{N_{faces}} (M^i + R^i \times F^i)$$

where R^i is the moment arm from the centroid of the fragment to the centroid of the face in which the force F^i is acting on.

The following step is to use the equilibrium condition, to compute the total force F^* and moment M^* acting at the centroid of the potential crack plane:

$$\begin{aligned} F^{crack}_{centroid} &= -F_{centroid} \\ M^{crack}_{centroid} &= -M_{centroid} \end{aligned}$$

The final step is to get the tractions acting on the potential fracture plane from the total force and total moment, which have to be transformed from the global coordinate system to the local coordinate system. Therefore,

$$\begin{aligned} t_x &= \frac{F^{crack}_{centroid}(1)}{Area_{crack}} * m_{local} \\ t_y &= \frac{F^{crack}_{centroid}(2)}{Area_{crack}} * l_{local} \\ t_n &= \frac{F^{crack}_{centroid}(3)}{Area_{crack}} * n_{local} \\ t_s &= \sqrt{t_x^2 + t_y^2} \end{aligned} \tag{3.21}$$

3.4 Microscopic Fracture Criterion

A transgranular fracture criterion at the grain scale, is developed based on the Discrete Element model presented in Chapter 2, the Euler-Bernoulli Bean Theory and the Griffith Fracture Theory. This criterion allows fragmentation of a single discrete element into two discrete element s along its cleavage plane.

The fracture criterion developed consists of two stages: First, an average Cauchy stress tensor, $\bar{\sigma}_i$, is computed for each grain i (represented by a discrete element) from the discrete

contact forces acting on it as described in Section 2.4. In this stage, the criterion assumes that transgranular fracture occurs if the hydrostatic stress is higher than a threshold value σ_f^{hyd}, Damien et. al [7]

$$\frac{1}{3}\mathrm{tr}(\bar{\sigma}_{\mathrm{i}}) \geq \sigma_{\mathrm{f}}^{\mathrm{hyd}} \tag{3.22}$$

If this stress criterion is reached, then second stage consists of the calculation of the tractions at the potential crack plane from the tractions at the boundary of the grain. The potential crack plane orientation is chosen according to the crystallographic orientation of the grain. Next, the stress intensity factors (K_I, K_{II}) are computed based on the traction values and the normal and shear stresses computed using the Euler-Bernoulli beam theory.

$$K_I = \sigma\sqrt{a\pi} \qquad K_{II} = \tau\sqrt{a\pi} \tag{3.23}$$

where a is the crack length and

$$\sigma = \frac{t_n}{A} \pm \frac{M_z y}{I} \qquad \tau = \frac{t_s Q}{Ib} \tag{3.24}$$

t_n and t_s are the normal and shear tractions at the crack plane computed by the expressions in (3.21), y is the distance from the neutral axis, A is the area of the fracture surface, M_z is the bending moment around the $z-$axis, Q and I are the first and second area moment of inertia respectively.

Transgranular fracture occurs if

$$\left(\frac{K_I}{K_{Ic}}\right)^2 + \left(\frac{K_{II}}{CK_{Ic}}\right)^2 \geq 1 \tag{3.25}$$

where $C = 0.816$, as originally suggested by Palaniswamy and Knauss in 1978.

The trasgranular fracture approach was implemented into the *DEM* code so polyhedra particles can fragment according to the fracture criteria described in 3.22 and 3.25. The algorithm below contains the steps on how the fragmentation process is performed.

Transgranular Fracture Algorithm

Step 1. Compute contact forces and moments as described in Chapter 2

Step 2. Compute stresses for each particle as described in Equation (2.17)

Step 3. Check Stress Criterion 3.25. If the criterion is met, then for each particle:

- **3.1.** Compute tractions for each of the six rectangular faces of the polyhedron representing the particle as described in Equation (3.19)
- **3.2.** Compute tractions at the potential "crack plane" as described in Equation (3.21)
- **3.3.** Check Stress Intensity Factor Criterion 3.25. If criterion is met, proceed to fragment particle by replacing it with two discrete elements. I criterion is not met, continue to examine the next particle.

Step 4. Continue computation for next time step.

3.5 DEM Simulations

3.5.1 Drop test on unbonded particles

The drop test model consists of 44 close packed hexagonal prismatic particles of random crystallographic orientation. After generating the microstructure, and completing the DEM simulation, the results were visualized using PARAVIEW. Starting from their initial positions, as shown in Figure 3.18a), the particles were affected only by gravitational forces and started immediately to move towards the bottom of the box as shown in Figure 3.18b). Once the particles come into contact with each other and with the bottom

wall (Figure 3.18c) - Figure 3.18e)), they started to repel each other and fragment. Unbonded contacts are indicated by the small red spheres visible in the simulation results. As particles are no longer in contact, the red spheres disappear. The particle fragments will bounce up and down until all particles finally settle due to the dissipated energies through the collisions as shown in Figure 3.18f). This simulation was run for 10000 time steps. The parameters used in this DEM simulation are included in Table **??**.

3.5.2 Uniaxial compression test

For the uniaxial compression tests, a single plane models consisting of 44 hexagonal prismatic particles, resulting in a model size of $5\ mm \times 10\ mm \times 2\ mm$ was generated as described in Section 2.2.2. The parameters used in the initial DEM simulation are included in Table **??**. Loading velocity of $0.001mm/s$ was applied on the upper and lower surfaces using DEM rigid elements to compress the particles until initial contact was achieved. After the initial contact model was generated, the bonding forces were activated. The initial bonding parameters applied to the models are provided in Table **??**. Polyhedra particles fragment according to the stress criteria 3.22 and the stress intensity fracture criteria 3.25 both describe in Section 3.4. Figure 3.19a) - Figure 3.19d) show the evolution of transgranular fracture at time steps 0, 100, 300 and 500 respectively.

3.5.3 Brazilian test simulation

For the Brazilian tests, a single plane models consisting of 160 polyhedral particles, resulting in a model size of $156\ mm \times 156\ mm \times 18\ mm$ was generated as described in Section 2.2.2. The parameters used in the initial DEM simulation are included in Table

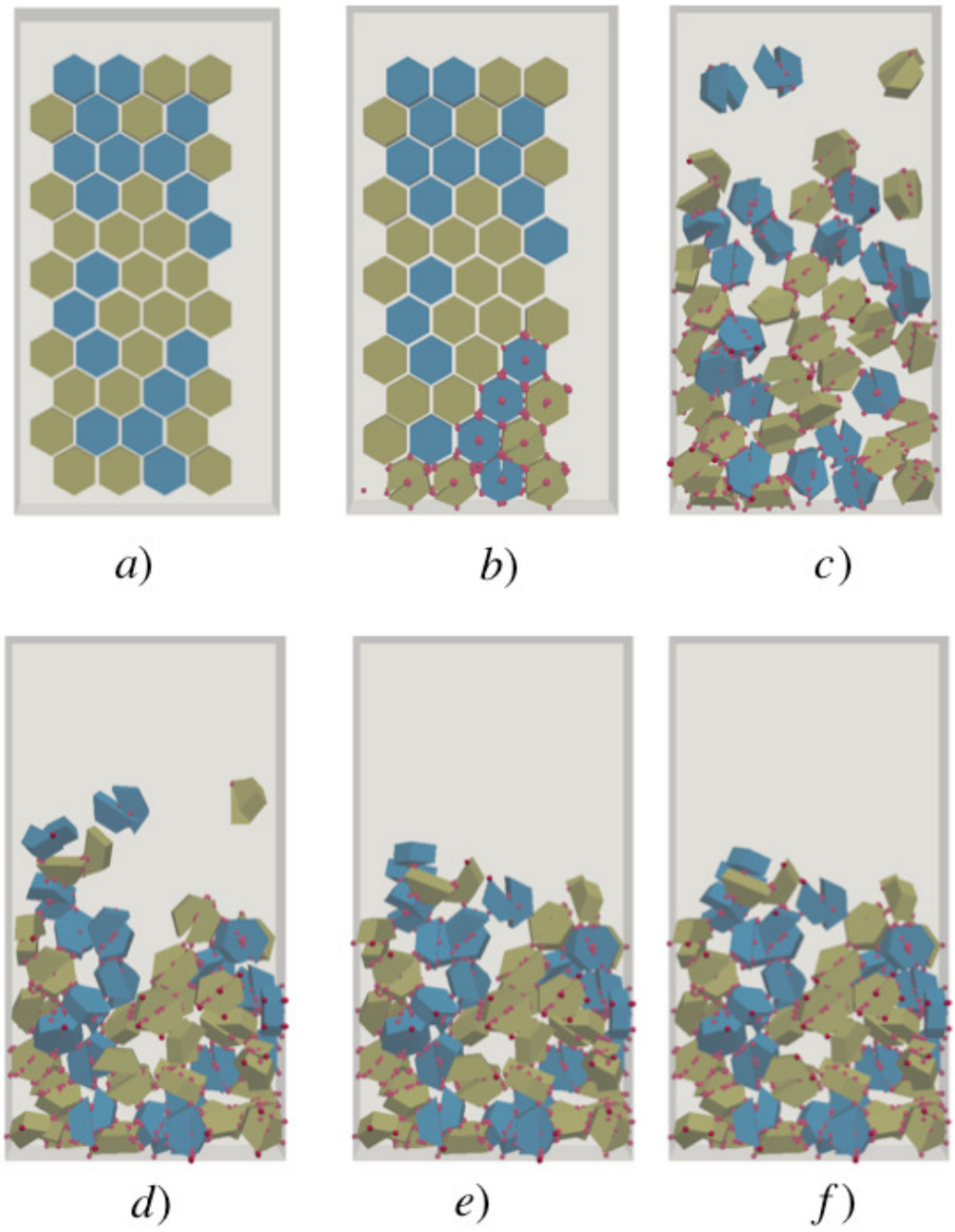

Figure 3.18

Simulation of falling polyhedral particles which fragment when touching the ground. Contacts are represented by red spheres. Particle colors represent crystallographic orientations of the grains. a) initial step, b) - e) intermediate steps, and f) final step

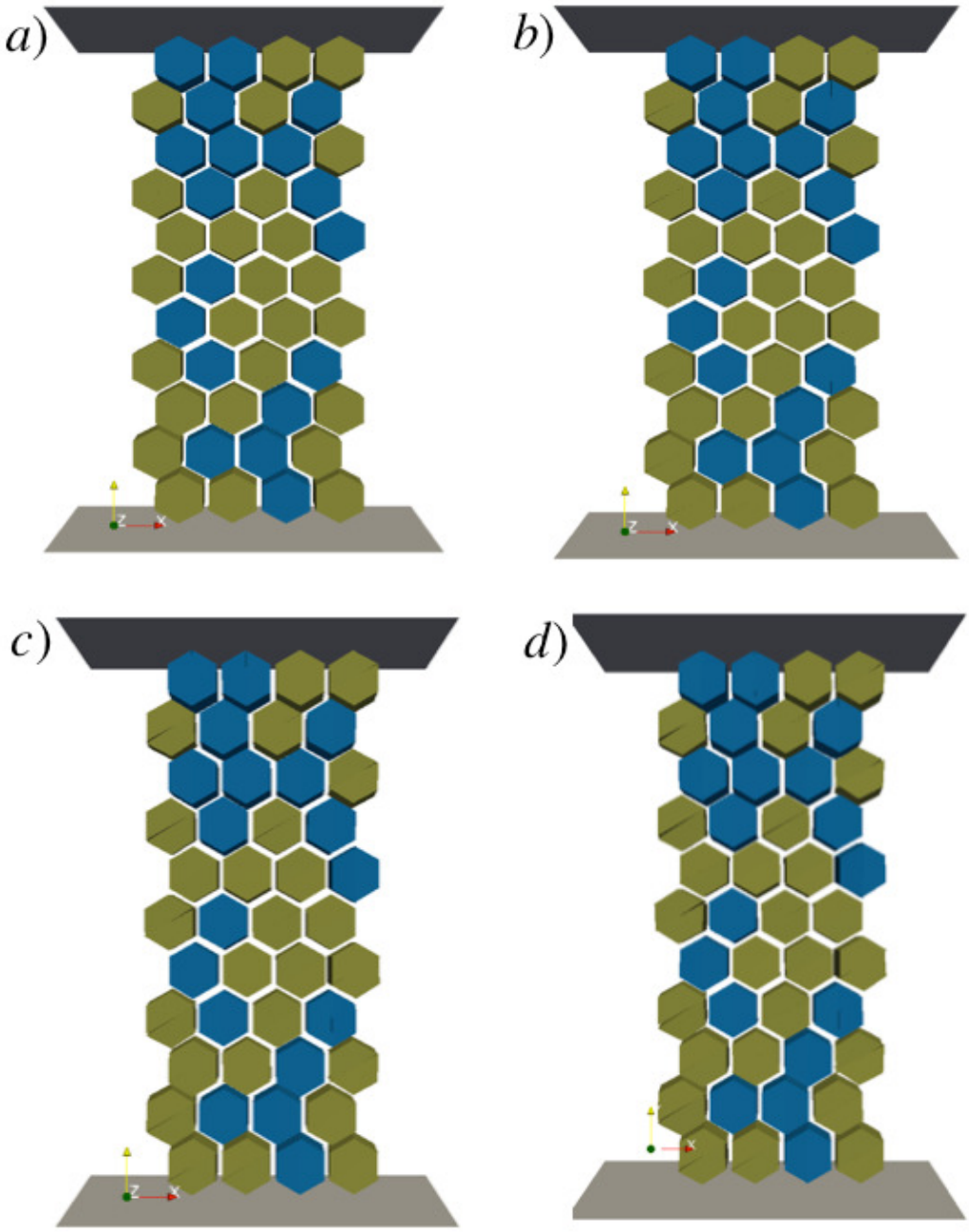

Figure 3.19

Uniaxial compression test with transgranular fracture a) initial step, b) at 100 step, c) at 300 step and d) at 500 step

??. Loading velocity of $0.001mm/s$ was applied on the upper and lower surfaces using DEM rigid elements to compress the particles until initial contact was achieved. After the initial contact model was generated, the bonding forces were activated. The initial bonding parameters applied to the models are provided in Table **??**. Polyhedra particles fragment according to the stress criteria 3.22 and the stress intensity fracture criteria 3.25 both described in Section 3.4. Figure 3.20a) - Figure 3.20d) show the evolution of transgranular fracture at time steps 0, 100, 500 and 2000 respectively.

A transgranular fracture model was developed based on the discrete element method. Fracture within the grains was be performed by replacing a grain (an intact discrete element) with a fractured one (with two intact discrete elements bounded by a fractured surface). The fracture criteria is based on the continuous traction parameters described in terms of the discrete forces by using the principle of virtual work. The model was implemented into the ERDC DEM code and it was tested by performing three types of simulations tests: drop, uniaxial compression and Brazilian.

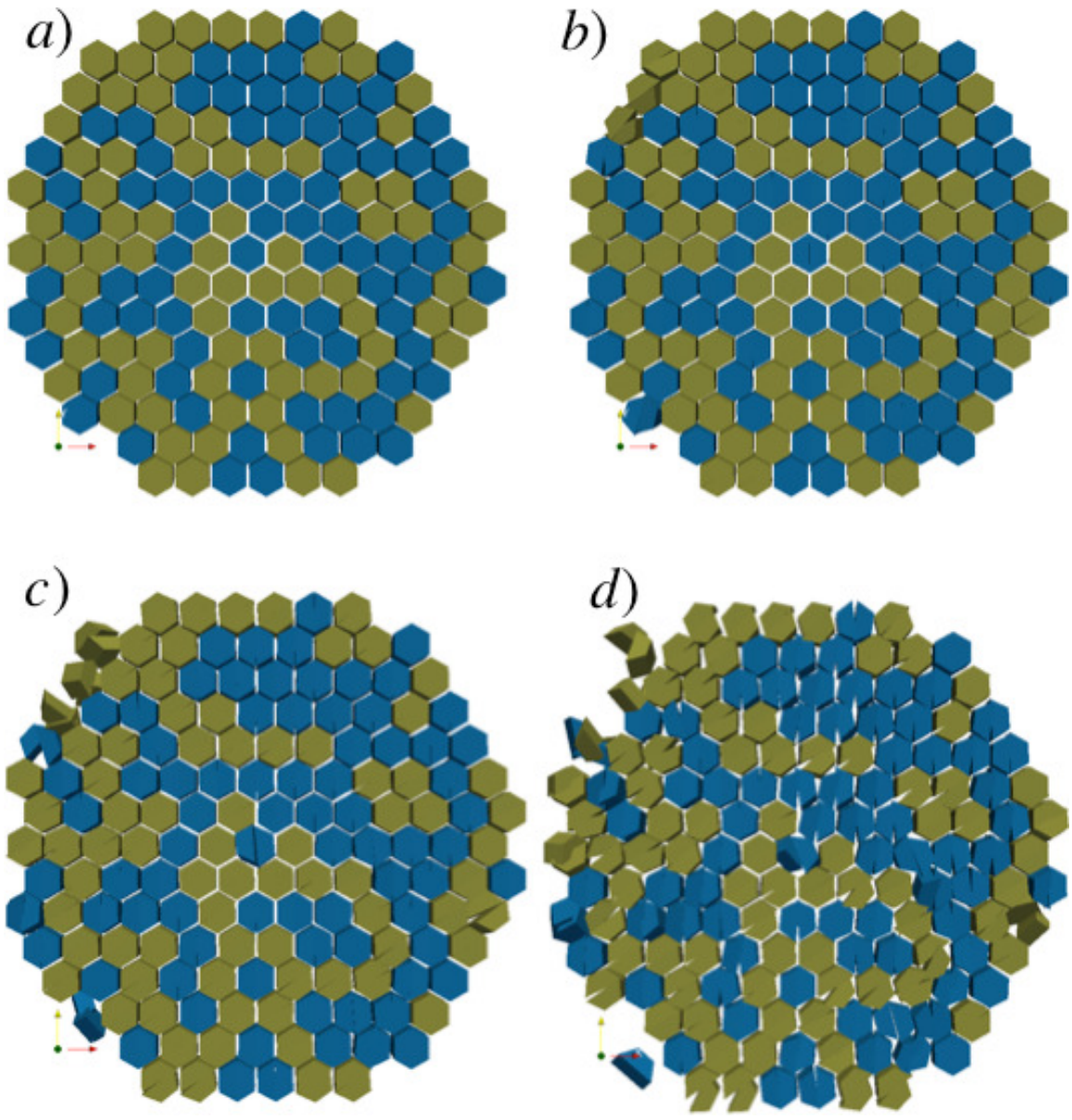

Figure 3.20

Brazilian test with depiction of transgranular fracture at a) time step 0, b) time step 100, c) time step 500 and d) time step 2000

CHAPTER 4

CONCLUSIONS

4.1 Summary

The main goal of this dissertation was to develop a fracture model for brittle polycrystalline materials based on a discrete element method. In this work, the development, implementation, verification and validation of a bonded particle model for the study of cohesive particles and brittle structures using a discrete element method were presented. The developed model has been successfully implemented into the initial USACE-ERDC DEM code. The most important features of our DEM are the way in which bonded contacts are treated and the way in which discrete elements are fragmented based on the tractions acting at the discrete elements surfaces.

In Chapter 1 an overview of the fundamental theory and fracture behavior of brittle polycrystalline materials was presented as well as an overview on the current state on the development of discrete element methods to simulate the brittle fracture. In Chapter 2 a detailed explanation of the main features in the development and implementation of the bonded polyhedra DEM model, such as discrete element geometry, contact detection algorithms, contact law and bonded contacts were provided. The model was implemented for a brittle, polycrystalline material consisting of two crystallographic orientations for the grains. The new formulation has the capability of capturing intergranular fracture within

the particle model on the basis of bonding properties and forces acting on each discrete element. The contact detection was verified in a drop test case to observe motion of individual particles.

In Chapter 3 a transgranular fracture model for brittle polycrystalline materials was described. These type of materials are composed of grains separated incompatibly by grain boundary regions, in this work we describe the material as an assemblage of grains modeled as discrete elements whereby the grain and grain boundaries have distinct fracture criteria. The discrete elements used to represent the grains were assumed to be rigid, making the stress state statically indeterminate. To tackle this, we used the virtual work principle to determine statically equivalent stress states in the forms of average stresses (within the grains) and tractions (on grain boundaries) from which continuos fracture criteria can be employed. Specifically, the transgranular fracture criterion was based on the continuous tractions parameters calculated in terms of the discrete forces by using the principle of virtual work.

4.2 Contributions

In the current work, we expand a basic discrete element model for non-cohesive spherical and cylindrical particle assemblies to include polyhedral-shaped bonded particles to better represent intergranular fracture of a brittle polycrystalline microstructure. Although a basic contact-bonding law was implemented in the initial ERDC DEM code, further tests were needed. In this work several modifications/improvements were made to the polyhedra particle model and to the bonded contact definitions:

- Implemented a technique for generating a synthetic polycrystalline microstructure with random crystallographic orientation for the DEM model.
- Changed prismatic particle "sectioning" for fracture implementation.
- Added subroutine to DEM code to visualize frictional contacts using color-coded beams and bonded contacts using beams in the simulation.
- Added particle stress output subroutine based on magnitude and orientation for visualization in POV-RAY.
- Verified the contact detection procedure using a drop test model.
- Tested the implementation of the bonded-contact model using uniaxial compression, four-point bending test, and Brazilian test.
- Development of a framework based on a discrete element method is presented to model the behavior of polycrystalline grains and grain boundaries.
- Failure of the model material was simulated as a combination of intergranular and transgranular modes depending on the specific material properties and loading configurations.
- Use of the virtual work method to link discrete contact forces to equivalent continuous tractions allows the creation of any number of statically equivalent load distributions as might be needed to create realistic fracture criteria.
- Development of a fracture criterion for the rigid discrete elements which are statically indeterminate.

4.3 Further Research

A fracture model based on a discrete element method to model the mechanical behavior of brittle polycrystalline materials has been presented in this dissertation. Although a new approach has beed developed to account for transgranular fracture of discrete elements representative of polycrystalline grains, several issues have been left for future work:

- A particle size effect study.
- Optimization of contact search approach.
- Improvement of the contact law by means of the implementation of an orthotropic cohesive contact law.

- Calibration of the model proposed in this work using dimensional analysis and the principle of similitude.
- Validation of the model for ceramic materials using experimental data from the literature.
- Implementation of more types of crystallographic orientations.
- Paralellization of the DEM code.

From the author's point of view, all the above mentioned issues should be addressed to gain better understanding of the fracture behavior of brittle polycrystalline materials. The author is aware of the computational challenges in terms of computational resources and implementation of the approaches that might help in this regard but the author is hopeful that the contributions made in this dissertation can help in the advancement on the development of discrete elements methods to model the fracture behavior of brittle polycrystalline materials.

REFERENCES

[1] "POV-Ray,".

[2] F. Abraham, D. Brodbeck, W. Rudge, J. Broughton, D. Schneider, B. Land, D. Lifka, J. Gerner, M. Rosenkrantz, J. Skovira, and H. Gao, "Ab initio dynamics of rapid fracture," *Modelling and Simulation in Materials Science and Engineering*, vol. 6, 1998, pp. 639–670.

[3] G. A. A'ddetta, F. Kun, E. Ramm, and H. J. Herrmann, "From solids to granulates - Discrete element simulations of fracture and fragmentation processes in geomaterials," *Continuous and Discontinuous Modelling of Cohesive-Frictional Materials*, P. A. Vermeer, ed., vol. 568 of *Lecture Notes in Physics*, Springer Berlin Heidelberg, 2001, pp. 231–258.

[4] F. Adessio and J. Johnson, *A constitutive model for the dynamic response of brittle materials*, Tech. Rep. LA-UR-89-2651, Los Alamos National Laboratory, 1999.

[5] O. Adewoye, "Anisotropic behavior of etched hardness indentations," *Journal of Material Science*, vol. 11, no. 5, 1976, pp. 981–984.

[6] T. L. Anderson, *Fracture mechanics: Fundamentals and applications*, 3rd edition, CRC Press is an imprint of Taylor & Francis Group, 2005.

[7] D. André, M. Jebahi, I. Iordanoff, J.-L. Charles, and J. Néauport, "Using the discrete element method to simulate brittle fracture in the indentation of a silica glass with a blunt indenter," *Computer Methods in Applied Mechanics and Engineering*, vol. 265, 2013, pp. 136 – 147.

[8] R. Barbosa, *Discrete element models for granular materials and discrete element models for granular materials and rock masses*, doctoral dissertation, University of Illinois at Urbana-Champaing, 1990.

[9] Z. Bazant and B. Oh, "Microplane model for progressive fracture of concrete and rock," *Journal of Engineering Mechanics ASCE 111*, vol. 4, 1985, p. 559.

[10] T. Belytschko, Y. Krongauz, D. Organ, M. Fleming, and P. Krysl, "Meshless methods - An overview and recent developments," *Computer Methods in Applied Mechanics and Engineering*, vol. 139, 1996, pp. 3–47.

[11] T. Belytschko and M. Tabbara, "Dynamic fracture using element-free galerkin methods," *International Journal for Numerical Methods in Engineering*, vol. 39, 1996, pp. 923–938.

[12] N. Bićanić, "Discrete element methods," *Encyclopedia of Computational Mechanics*, vol. 1, John Wiley and Sons, 2007.

[13] R. C. Bradt et al., eds., *Mixed-mode fracture of ceramics*, vol. 8. Plenum Press. New York - London, 1986.

[14] J. Bruchmüller, B. G. M. van Wachem, S. Gu, and K. H. Luo, "Modelling discrete fragmentation of brittle particles," *Powder Technology*, 2011, pp. 731 – 739.

[15] G. Camacho and M. Ortiz, "Computational modeling of impact damage in brittle materials," *International Journal of Solid and Structures*, vol. 33, 1996, pp. 2899–2938.

[16] H. Carmona, F. K. Wittel, and F. Kun, "From fracture to fragmentation: Discrete element modeling. Complexity of crackling noise and fragmentation phenomena revealed by discrete element simulations," *The European Physical Journal Special Topics*, vol. 223, no. 11, 2014, pp. 2369–2382.

[17] A. Carrillo, J. West, D. A. Horner, and J. F. Peters, "Interactive large-scale soil modeling using distributed high performance computing environments," *The International Journal of High Performance Computing Application*, vol. 13, no. 1, 1999, pp. 38–48.

[18] L. Y. Chao and D. K. Shetty, "Reliability analysis of structural ceramics subjected to biaxial flexure," *Journal of the American Ceramic Society*, vol. 74, 1991, pp. 333–344.

[19] K. S. Cho, "R-Curve behavior of layered silicon carbide ceramics with surface fine microstructure," *Journal of Material Science*, vol. 36, 2001, pp. 2189–2193.

[20] B. Cotterell and Y. W. Mai, *Fracture mechanics of cementitious materials*, 1 edition, Blackie Academic and Professional, 1996.

[21] A. G. Crocker, P. E. J. Flewitt, and G. E. Smith, "Computational modeling of fracture in polycrystalline materials," *International Materials Reviews*, vol. 50, no. 2, 2005, pp. 99 – 124.

[22] P. A. Cundall, "Formulation of a three-dimensional distinct element model - Part I. A scheme to detect and represent contacts in a system composed of many polyhedral blocks," *International Journal of Rock Mechanics and Mining Sciences*, vol. 25, no. 3, 1988, pp. 107 – 116.

[23] P. A. Cundall and O. D. L. Strack, "A discrete numerical model for granular assemblies," *Géotechnique*, vol. 29, 1979, pp. 47–65.

[24] D. Curran, L. Seaman, T. Cooper, and D. Shockey, "Micromechanical model for comminution and granular flow of brittle material under high strain rate application to penetration of ceramic targets," *International Journal Impact Engineering*, vol. 13, 1990, pp. 53–83.

[25] L. A. Dergaputskaya et al., "Introduction of industrial production of polycrystalline oxide fibers," *Refractories and Industrial Ceramics*, vol. 31, no. 3, 1990, pp. 231–233.

[26] E. N. Devorkin, A. M. Cuitino, and G. Gioia, "Finite elements with displacement interpolated embeded localization lines insentive to mesh size and distortions," *International Journal for Numerical Methods in Engineering*, vol. 30, 1990, pp. 541–564.

[27] F. Donzé, V. Richefeu, and S. A. Magnier, "Advances in discrete element method applied to soil, rock and concrete mechanics," *The Electronic Journal of Geotechnical Engineering*, vol. Bouquet 08.

[28] S. Esedoglu, "Large-scale simulations of grain boundary motion in polycrystals," *SIAM News*, vol. 43, no. 8, 2010.

[29] H. Espinosa, "On the dynamic shear resistance of ceramic composites and its dependence on applied multiaxial deformation," *Internation Journal of Solid and Structures*, vol. 32, no. 3105, 1995.

[30] H. Espinosa, P. Zavattieri, and Dwivedi, "A finite deformation continuum/discrete model for the description of fragmentation and damage in brittle materials," *Journal of the Mechanics and Physics of Solids*, vol. 46, no. 10, 1998, pp. 1909 – 1942.

[31] S. Freiman and J. M. Jr., *The fracture of brittle materials. Testing and analysis*, John Wiley and Sons Inc., 2012.

[32] H. Gao, "A theory of local limiting speeds in dynamic fracture," *Journal of the Mechanics and Physics of Solids*, vol. 44, 1996, pp. 1453–1474.

[33] S. R. Geer, *Discrete element and homogenization based approaches for determining the mechanical properties of geomaterials*, doctoral dissertation, Colorado School of Mines, 2014.

[34] W. T. Geng, A. J. Freeman, R. Wu, and G. B. Olson, "Effect on Mo and Pd on the grain-boundary cohesion of Fe," *Physical Review B: Covering Condensed Matter and MAterials Physics*, vol. 62, no. 6208, 2000.

[35] A. A. Griffith, "The phenomena of flow and rupture in solids," *Philosophical Transactions of the Royal Society*, vol. A, no. 221, 1921.

[36] M. Groeber, S. Ghosh, M. D. Uchic, and D. M. Dimiduk, "A framework for automated analysis and simulation of 3d polycrystalline microstructures. Part 2: Synthetic microstructure generation," *Acta Materialia*, vol. 56, 2008, pp. 1274–1287.

[37] M. Groeber and M. Jackson, "DREAM.3D: A digital representation environment for the analysis of microstructure in 3D," *Integratin Materials and Manufacturing Innovation*, vol. 3, no. 5, November 2014.

[38] P. Gumbsch, B. Zhou, and S. J. Holian, "Molecular dynamics of dynamic crack stability," *Physical Review B: Condensed Matter*, vol. 55, no. 6, 1997, pp. 3445–3455.

[39] E. O. Hall, "The deformation and ageing of mild steel: III Discussion of results," *Proceedings of the Physical Society. Section B*, vol. 64, no. 9, 1951, pp. 747–753.

[40] S. Hentz, F. V. Donzé, and L. Daudeville, "Discrete element modeling of concrete submitted to dynamic loading at high strain rates," *Computers and Structures 82*, vol. 29-30, 2004, pp. 2509–2524.

[41] C. Hogue, "Shape representation and contact detection for discrete element simulations of arbitrary geometries," *Engineering Computations*, vol. 15, no. 3, 1998, pp. 374 – 390.

[42] T. Holmquist and G. Johnson, "A computational constitutive model for bbrittle materials subjected to large strains, high strain rates and high pressures," *Journal of Applied Mechanics*, vol. 78, no. 5, 2011.

[43] M. A. Hopkins, *Numerical simulation of systems of multitudinous polygonal blocks*, Tech. Rep., The United States Army Corps of Engineers Cold Regions Research and Engineering Laboratory, 1992.

[44] M. A. Hopkins, "discrete element modeling with dilated particles," *Engineering Computations*, vol. 21, no. 2/3/4, 2004, pp. 422 – 430.

[45] M. A. Hopkins, "Polyhedra on the cheap," *Discrete Element Methods Simulations of Discontinua: Theory and Applications. Queen Mary University of London*, 2010, pp. 46–50.

[46] D. Horner, A. R. Carrillo, J. F. Peters, and J. E. West, "High resolution soil vehicle interaction modeling," *Mechanics of Structures and Machines*, vol. 26, no. 3, 1998, pp. 305–318.

[47] H. Huang, J. D. Hales, B. W. Spencer, and J. E. Dolbow, "Discrete modeling of early-life thermal fracture in ceramic nuclear fuel,", 2015.

[48] A. Ibrahimbegovic and A. Delaplace, "Microscale and mesoscale discrete models for dynamic fracture of structures built of brittle material," *Computers and Structures*, vol. 81, 2003, pp. 1255–1265.

[49] C. E. Inglis, "Stresses in a plate due to the presence of cracks and sharp corners," *Transactions of the Royal Institution of Naval Architects*, vol. 55, no. 219, 1913.

[50] G. F. M. IV, *Developments for the advancement of the discrete element method*, doctoral dissertation, Univeristy of South Carolina, 2015.

[51] A. Jacobson, "Sphere packing lattice generation,", 2007.

[52] S. Ji, S. Sun, and Y. Yan, "Discrete element modeling of rock materials with dilated polyhedral elements," *Procedia Engineering*, vol. 102, 2015, pp. 1793–1802.

[53] J. J.Kruzic, R. M. Cannon, and R. O. Ritchie, "Effects of moisture on grain-boundary strength, fracture and fatigue properties of alumina," *Journal of the American Ceramic Society*, vol. 88, no. 8, 2005, pp. 2236 – 2245.

[54] T. Kazerani, *Micromechanical study of rock fracture and fragmentation under dynamic loads using discrete element method*, doctoral dissertation, École Polytechnique Fédérale De Laussane, 2011.

[55] T. Kazerani and J. Zhao, "Micromechanical parameters in bonded particle method for modeling of brittle material failure," *International Journal for Numerical and Analytical Methods in Geomechanics*, vol. 34, 2010, pp. 1877 – 1895.

[56] Kitware, "Paraview repository. http://www.paraview.org/Wiki/ParaView,".

[57] P. A. Klerck, E. J. Sellers, and D. R. J. Owen, "Discrete fracture in quasi-brittle materials under compressive and tensile stress states," *Computer Methods in Applied Mechanics and Engineering*, vol. 193, 2004, pp. 3035 – 3056.

[58] R. Kraft, J. Molinari, K. Ramesh, and D. Warner, "Computational micromechanics of dynamic compressive loading of a brittle polycrystalline material using a distribution of grain boundary properties," *Journal of the Mechanics and Physics of Solids*, vol. 56, 2008, pp. 2618 – 2641.

[59] F. Kun and H. J. Herrmann, "A Study of fragmentation process using a discrete element method," *Computer Methods in Applied Mechanics and Engineering*, vol. 138, 1996, pp. 3–18.

[60] C. Kunka, A. Trachet, and G. Subhash, "Interaction of indentation-induced cracks on single-crystal silicon carbide," *Journal of the American Ceramic Society*, vol. 98, no. 6, 2015, pp. 1891–1897.

[61] B. R. Lawn and T. R. Wilshaw, *Fracture of brittle solids*, Cambridge Solid State Science Series, 1993.

[62] B. D. Le, G. Koval, and C. Chazallon, "Discrete element approach in brittle fracture mechanics," *Engineering Computations*, vol. 30, no. 2, 2013, pp. 263–276.

[63] B. D. Le, G. Koval, and C. Chazallon, "Discrete element model for crack propagation in brittle materials," *International Journal for Numerical and Analytical Methods in Geomechanics*, vol. 40, 2016, pp. 583 – 595.

[64] P. Lejček and S. Hofmann, "Thermodynamics and structural aspects of grain boundary segregation," *Critical Reviews in Solid State and Materials Sciences*, vol. 20, no. 1, 1995, pp. 1 – 85.

[65] A. Lisjak and G. Grasselli, "A review of discrete modeling techniques for fracturing processes in discontinuous masses," *Journal of Rock Mechanics and Geotechnical Engineering*, vol. 6, 2004, pp. 301 –314.

[66] S. Mariani and U. Perego, "Extended finite element method for quasi-brittle fracture," *International Journal for Numerical Methods in Engineering*, vol. 58, 2003, pp. 102–126.

[67] C. Martin, H. C. Montes, L. Olmos, D. Bouvard, and K. Bordia, "Evolution effects during sintering: discrete element simulations," *Journal of the American Ceramic Society*, vol. 92, no. 7, 2009, pp. 1435 – 1441.

[68] O. Miller, L. B. Freund, and A. Needleman, "Modeling and simulation of dynamic fragmentation in brittle materials," *International Journal of Fracture*, vol. 96, no. 2, 1999, pp. 101–125.

[69] E. Mitra, P. J. Hazell, and M. Ashraf, "A discrete element model to predict the pressure-density relationship of blocky and angular ceramic particles under uniaxial compression," *Journal of Material Science*, vol. 50, 2015, pp. 7742–7751.

[70] A. Munjiza, *The combined finite-discrete element method*, John Wiley and Sons Inc., 2004.

[71] T. Y. nd T. Kwasaki and J. L. Swedlow, eds., *An examination of the fracture mechanics energy balance from the point of view of continuum mechanics*, vol. I. Japanese Society of Strength and Fracture of Materials, 1966.

[72] S. Nishitani, K. Togase, Y. Yamamoto, H. Fujiwara, and T. Kaneko, "Metastable solvent epitaxi of Sic, the other diamond synthetics," *Silicon Carbide - Materials, Processing and Applications in Electronic Devices, Dr. Moumita Mukherjee (Ed.), ISBN: 978-953-307-968-4*, M. Mukherjee, ed., InTech, 2011.

[73] P. G. Nittur, S. Maiti, and P. H. Geubelle, "Grain-level analysis of dynamic fragmentation of ceramics under multi-axial compression," *Journal of the Mechanics and Physics of Solids*, vol. 56, 2008, pp. 993 – 1017.

[74] M. Oda and K. Iwashita, *Mechanics of granular material*, A. A. Balkema Publishers, 1999.

[75] M. Ortiz, Y. Leroy, and A. Needleman, "A finite element method for localized failure analysis," *Computer Methods in Applied Mechanics and Engineering*, vol. 61, 1987, pp. 189–214.

[76] A. Palaniswamy and W. G. Knauss, "On the probem of crack extension in brittle solids under general loading," *Mechanics Today*, vol. 4, 1978, pp. 87–148.

[77] A. Paluzsny, X. H. Tang, and R. W. Zimmerman, "Fracture and impulse based finite-discrete element modeling of fragmentation," *Computational Mechanics*, P. Wriggers, ed., Springer, 2013.

[78] J. F. Peters, *Private communication with author*, The United States Army Corps of Engineers Engineer Research and Development Center (USACE- ERDC), February 28^{th} 2013.

[79] J. F. Peters, *A note on particle-scale definition of stress*, Tech. Rep. ERDC/CRREL SR-05-78, Engineering and Research Develoment Center, April 2014.

[80] J. F. Peters, R. Kala, and R. Maier, "A hierarchical search algorithm for DEM of greatly differing particle sizes," *Engineering Computations*, vol. 26, no. 6, 2009, pp. 621–634.

[81] J. F. Peters, R. Kala, R. Maier, and L. Walizer, *Draft for beta review: User guide for DEM*, The United States Army Corps of Engineers Engineer Research and Development Center (USACE- ERDC), 2011.

[82] D. O. Potyondy and P. A. Cundall, "A bonded particle model for rock," *International Journal of Rock Mechanics and Mining Sciences*, vol. 41, 2004, pp. 1329 – 1364.

[83] G. D. Quinn, *Nist recommended practice guide: Fractography of ceramics and glasses*, Special Publication 960-16, National Institute of Standarts and Technology, 2007.

[84] F. Radja$\ddot{i}$ and F. Dubois, *Discrete element modeling of granular materials*, John Wiley and Sons, Inc, 2011.

[85] M. Rajagopalan, M. A. Tschopp, and K. N. Solanki, "Grain boundary segregation of interstitial and substitution impurity atoms in alpha-iron," *The Journal of The Minerals, Metals & Materials Society (TMS)*, vol. 66, no. 1, 2014, pp. 129 – 138.

[86] J. R. Rice, "Solid Mechanics Course. School of Engineering and Applied Sciences, and Department of Earth and Planetary Science,", Harvard University, 2010.

[87] D. Roylance, "Modules in mechanics of materials, a web-based collection of educational modules developed under the auspices of the National Science Foundation,", Department of Material Science and Engineering. Massachussetts Institute of Technology, 2000.

[88] K. Saleme and T. Stone, *Method for digitally generating the microstructure for brittle and layered biomaterials*, ERDC Interim Report 1, Mississippi State University: Center for Advanced Vehicular Systems, 2012.

[89] R. Senapati, *Discrete element modeling of silicon nitride ceramics: Crack formation and propagation in indentation test and four point bending test*, master's thesis, The University of Texas at El Paso, 2009.

[90] M. Sharafisafa and M. Nazem, "Application of the distinct element method and the extended finite element method in modelling cracks and coalescence in brittle materials," *Computational Material Science*, vol. 91, 2014, pp. 102 –121.

[91] X. Shi and A. A. Polycarpou, "Measurement and modeling of normal contact stiffness and contact damping at the meso scale," *Transactions of the ASME*, vol. 127, 2005, pp. 52–60.

[92] N. Sukumar, D. J. Srolovitz, T. J. Baker, and J. H. Prevost, "Brittle fracture in polycrystalline microstructures with the extended finite element method," *International Journal for Numerical Methods in Engineering*, vol. 56, 2003, pp. 2015–2037.

[93] M. Szelwis, *Particle-reinforced composites simulated by cohesive discrete elements*, doctoral dissertation, Technische Universität Hamburg-Harburg, 2011.

[94] Y. Tan, D. Yang, and Y. Sheng, "Discrete element method (DEM) modeling of fracture and damage in the machining process of polycrystalline SiC," *Journal of the European Ceramic Society*, vol. 29, no. 6, 2009, pp. 1029–1037.

[95] A. Tarokh and A. Fakhimi, "Discrete element simulation of the effect of particle size on the size of fracture process zone in quasi-brittle materials," *Computers and Geotechnics*, vol. 62, 2014, pp. 51 – 60.

[96] J. Wachtman et al., *Mechanical properties of ceramics*, John Wiley and Sons, 2009.

[97] L. Walizer and J. F. Peters, "A bounding box search algorithm for DEM simulation," *Computer Physics Communications*, vol. 182, 2011, pp. 281–288.

[98] E. Wang and N. Shrive, "Brittle fracture in compression: Mechanism, models and criteria," *Engineering Fracture Mechanics*, vol. 52, no. 6, 1995, pp. 1107–1126.

[99] L. Wang, L. Meimei, J. Almer, T. Bieler, and R. Barabash, "Structural characterization of polycrystalline materials by synchrotron X-rays," *Frontiers of Material Science*, vol. 7, no. 2, 2013, pp. 156–169.

[100] Y. Wang and P. Mora, "The ESyS-Particle: A new 3-D discrete element model with single particle rotation," *Advances in Geocomputing, Computer and Mathematical Applications*, H. Xing, ed., vol. 119 of *Lecture Notes in Earth Sciences*, Springer, 2008, pp. 183–222.

[101] T. Watanabe and S. Tsurekawa, "The control of brittleness and development of desirable mechanical properties in polycrystalline systems by grain boundary engineering," *Acta Materialia*, vol. 47, no. 15-16, 1999, pp. 4171–4185.

[102] P. C. with Author, *J. F. Peters*, Mississippi State University, June 29^{th} 2016.

[103] M. F. H. Wolff, V. Salikov, S. Antonyuk, S. Heinrich, and G. A. Schneider, "Three-dimensional discrete element modeling of micromechanical bending test of ceramic-polymer composite materials," *Powder Technology*, vol. 248, 2013, pp. 77–83.

[104] X.-P. Xu and A. Needleman, "Numerical simulation of dynamic interfacial crack growth allowing for crack growth away from the bond line," *International Journal of Fracture*, vol. 74, 1995, pp. 253–275.

[105] Z. Yan, C. L. Martin, O. Guillon, D. Bouvard, and C. S. Lee, "Microstructure evolution during co-sintering of Ni/BaTiO3 multilayer ceramic capacitors modeled by discrete element simulations," *Journal of the European Ceramic Society*, vol. 34, 2014, pp. 3167–3179.

[106] B. Yang, Y. Jiao, and S. Lei, "A Study on the Effects of Microparameters on Macroproperties for Specimens Created by Bonded Particles," *Engineering Computations*, vol. 23, no. 6, 2006, pp. 607 – 631.

[107] C. Yao, Q. H. Jiang, J. F. Shao, and C. B. Zhou, "A discrete approach for modeling damage and failure in anisotropic cohesive brittle materials," *Engineering Fracture Mechanics*, vol. 155, 2016, pp. 102 –118.

[108] P. Zavattieri and H. Espinosa, "An examination of the competition between bulk behavior and interfacial behavior of ceramics subjected to dynamic pressure-shear loading," *Journal of the Mechanics and Physics of Solids*, vol. 51, 2003, pp. 607–635.

[109] W. Zhang, *Dynamic modeling of crack propagation in ceramic laminate-toughened composites with weak interfaces by using discrete element method*, doctoral dissertation, Rheinisch -Westfälischen Technischen Hochschule Aachen University, 2013.

[110] C. Zhao, T. Nishiyama, and A. Murakami, "Numerical modelling of spontaneous crack generation in brittle materials using the particle simulation method," *Engineering Computations*, vol. 23, no. 5, 2006, pp. 566–584.

[111] J. W. Zimmermann, G. E. Hilmas, and W. G. Fahrenholtz, "Thermal shock resistance and fracture behavior of ZrB2-based Ffbrous monolith ceramics," *Journal of the American Ceramic Society*, vol. 92, no. 1, 2009, pp. 161–166.

APPENDIX A

HCP LATTICE GENERATION

The hexagonal prismatic honeycomb lattice used to create DEM prismatic particles is created by defining the coordinates of lattice points for two different types of planes (A and B) as shown in Figure A.1.

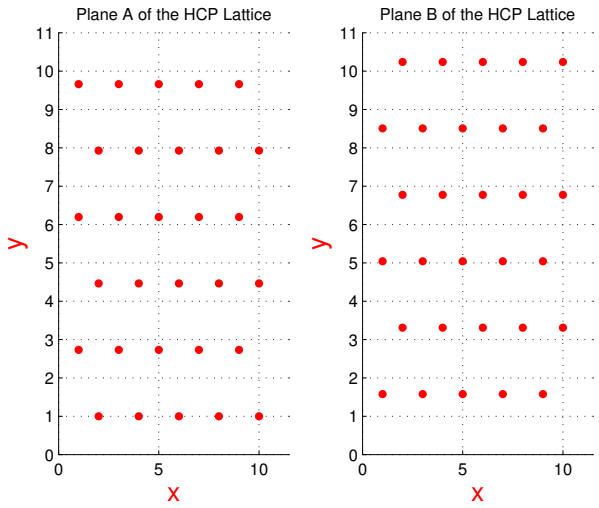

Figure A.1

Coordinate centers of the lattice points for Plane A and B of the HCP Lattice to fill a box with dimensions $12\times12\times1$

The planes are placed in a simple pattern of $A-B-A-B-A$.... Also, it is assumed that each lattice point will be non-negative to easily transform and translate the grain's positions using the HCP lattice points to fill any 3D space. Thus, the best location for the 3D space we aim to fill is with one corner at the origin as indicated in Figure 2.4.

A.1 Generation of Plane A

Plane A is generated by following the steps below:

a) Begin by making one row of grains.

Start with a hypothetical grain with side length r and center at $(0,\text{r},\frac{1}{2}\text{t})$ on the xyz space. Some of this grain's volume will be outside the box, so its center will not end up on the lattice; but it will be used as starting point. While keeping the $y-$ and $z-$ coordinates the same, add another grain so that the two grains touch. Continue by adding more grains in this row, along this line, until the $x-$ coordinate boundary of the box $\left(\left\lfloor\frac{2a}{\sqrt{3}r}\right\rfloor-2\right)$ is reached, see Figure A.2.

The coordinates for the lattice points of the first row will be

$$\left(\sqrt{3}ir, r, \frac{1}{2}t\right), \qquad for\ \ 1 \leq i \leq \left\lfloor\frac{2a}{\sqrt{3}r}\right\rfloor - 2.$$

b) To form the next row of grain centers on this plane, place a grain in the same $z-$ coordinate plane as the first row, but with a different $y-$ coordinate so that it will touch the first two grains of that first row.

As shown in Figure **??**, the three centers of these grains form an equilateral triangle with base $\sqrt{3}r$ and a height equals the $y-$ pitch from the first row to the second row, i.e.,

$$h = \sqrt{(\sqrt{3}r)^2 - \left(\frac{\sqrt{3}}{2}r\right)^2} = \frac{3}{2}r.$$

The $x-$ coordinate of the new grain is the same as the $x-$ coordinate of the point of contact between the grains in the first row, such that all the grains in the second row will have shifted a distance $\frac{\sqrt{3}}{2}r$.

Next, place the grains in a row with this new $y-$ coordinate, $r+h$, and the same $z-$ coordinate until the $x-$ coordinate boundary of the box is reached.

Lattice points (grain's center) coordinates of the second row will be given by:

$$\left(\frac{\sqrt{3}}{2}(2i-1)r, r+h, \frac{1}{2}t\right), \qquad for\ \ 1 \leq i \leq \left\lfloor\frac{2a}{\sqrt{3}r}\right\rfloor - 2.$$

c) Continuing this process of making new rows by adding the $y-$ pitch and shifting the rows in the $x-$ direction a distance $\frac{\sqrt{3}}{2}r$ until reaching the $y-$ coordinate boundary of the box $\left(\left\lfloor\frac{\frac{2}{3}(b+\frac{r}{2})}{r}\right\rfloor-1\right)$. This completes the generation of plane A for the lattice.

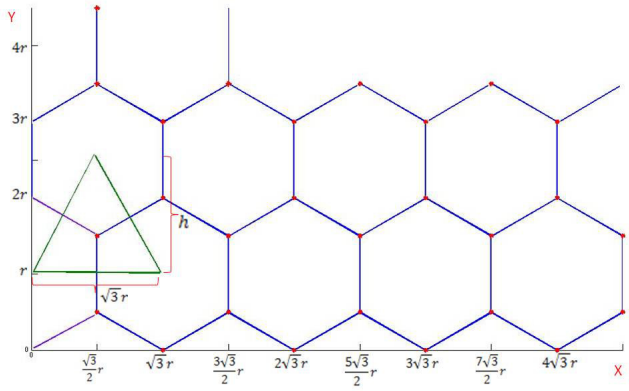

Figure A.2

Construction of Plane A of the hexagonal prismatic honeycomb lattice

A.2 Generation of Plane B

Plane B is generated in the same way as plane A by only changing the $\mathrm{z}-$coordinate. In this case, for each lattice point we need:

- The $x-$ coordinate varies from 1 to $\left\lfloor \frac{2a}{\sqrt{3}r} \right\rfloor - 2$.
- The $y-$ coordinate varies from 1 to $\left\lfloor \frac{\frac{2}{3}(b+\frac{r}{2})}{r} \right\rfloor - 1$.
- The $z-$ coordinate requires the addition of the $z-$ pitch $\frac{1}{2}t + t$.

A.3 Generation of Additional Planes

Continue the process as in step b) (page 16) alternating A and B planes and rows 1 and 2 within each plane until the $z-$ coordinate boundary $\left(\left\lfloor \frac{c+\frac{t}{2}}{t} \right\rfloor - 1\right)$ is reached. The $z-$ coordinates are given by

$$z = \frac{t}{2} + (k-1)t, \qquad \textit{for } 1 \leq k \leq \left\lfloor \frac{c + \frac{t}{2}}{t} \right\rfloor - 1.$$

Table **??** summarizes the xyz coordinates for each lattice point and Table **??** summarizes the xyz coordinates for each grain's vertex.

The steps to generate the coordinates of each HCP lattice point and the coordinates of their corresponding vertices that form an hexagonal prism with center at each lattice point are described in Algorithm A.3 and example is shown in Figure 2.6. This algorithm was implemented in several MATLAB subroutines, $HCP\_LatticePoints.m$ and $Grain\_Vertices.m$, included at the end of this appendix.

Algorithm for HCP packing of Hexagonal Grains.

Step 1. Define the dimensions a, b, and c for the 3D space to be filled.

Step 2. Define side length r.

Step 3. Compute the coordinates for each lattice point at each plane as described in Table 2.1.

Step 4. For each lattice point, compute its corresponding vertices to form the hexagonal prism as described in Table 2.2.

Step 5. Write files with center coordinates and vertices coordinates.

HoneycombLattice.m

```
function [Lattice]=HoneycombLattice(x,y,z,r,t)


% %This program will create a hexagonal lattice that fills a
three
% %  dimensional space with xyz dimensions.
```

```
% %  This lattice will give a honeycomb arrangement for the grains,
% %  which have hexagonal prisms shape
% %  Inputs:
% %      Box dimensions = x,y and z
% %       Grain dimensions = r (side length), t (thickness)
% %  Output:
% %      Lattice points coordinates = Lattice
% %  Copyright (c) 2013 Katerine SalemeRuiz.  All rights reserved.



m = fix(x/(sqrt(3)*r));
n = ceil(((2/3).*(y+(1/2)*r))./r)-1;
l = ceil((z + t/2)/t);
planeA = zeros(m*n,3);
Lattice = zeros(m*n*l,3);
i=zeros(m,1);
cont = 1;
for k=1:m
i(k)=k;
end
% %  compute lattice points
for k =1 :  l
for j = 1 :  n
```

```
if cont == 1
planeA((j-1)*m+1:j*m,1) = sqrt(3).*i.*r;
planeA((j-1)*m+1:j*m,2) = r.*ones(m,1) + (j-1).*(3/2).*r.*ones(m,1);
planeA((j-1)*m+1:j*m,3) = (t/2).*ones(m,1) + (k-1)*t*ones(m,1);
cont = 0;
else
planeA((j-1)*m+1:j*m,1) = (((sqrt(3)/2)*(2*i-1)).*ones(m,1)).*r;
planeA((j-1)*m+1:j*m,2) = r.*ones(m,1) + (j-1).*(3/2).*r.*ones(m,1);
planeA((j-1)*m+1:j*m,3) = (t/2).*ones(m,1) + (k-1)*t*ones(m,1);
cont = 1;
end
end
Lattice((k-1)*m*n+1:k*m*n,:)= planeA;
end
```

GrainVertices.m

```
function [Vertices] = GrainVertices(n,r,t, center)
% %  This subroutine reads the center's coordinate of a
% %  hexagonal prism and computes its 12 vertices.
% %  for each finite element of each wall of the box.
% %  Inputs:
% %      Number of sides = r
```

```
% %       Grain dimensions = r (side length), t (thickness)
% %       Grain center coordinates = center
% %  Output:
% %   Vertices = 12x3 matrix with the 12 vertices coordinates

% %  Copyright (c) 2013 Katerine SalemeRuiz.  All rights reserved.

%% Auxiliar data
theta = (360/n)*(pi/180);
Vertices = zeros(2*n,3);
aux = zeros(n,1);
auxc = zeros(n,1);
for i = 1:n
aux(i) = i-1;
auxc(i) = 1;
end
%% vertices
% front face
Vertices(1:n,1) = r * sin(theta.*aux(:))  + auxc(:).*center(1);
Vertices(1:n,2) = r * cos(theta.*aux(:))  + auxc(:).*center(2);
Vertices(1:n,3) = -(t/2) + auxc(:).*center(3);
% back face
```

```
Vertices(n+1:2*n,1) = r * sin(theta.*aux(:))  + auxc(:).*center(1);

Vertices(n+1:2*n,2) = r * cos(theta.*aux(:))  + auxc(:).*center(2);

Vertices(n+1:2*n,3) = (t/2) + auxc(:).*center(3);
```

APPENDIX B

CONTACT DETECTION ALGORITHMS

B.1 Coarse Contact Detection

The *coarse* search is performed to detect which particles might be in contact by using either a *basic* or *bounding-box* algorithm depending on the distribution of particle size.

1. ***Basic Spatial Discretization Algorithm.***

   This algorithm is simple to implement and requires that all cells be larger than the diameter of the largest particle in the system.

   Basic Search Algorithm.

   Step 1. Discretize the simulation space into cells of equal size.

   Step 2. Place each particle in a single cell based on the location of the particle's center. The particle's placement is based on converting the real coordinates of the particle center to integer coordinates. The integer coordinates correspond to the cell indices.

   Step 3. Perform a particle-based search for potential contacts. Loop the contact search over the particles. Select a particle, identify which cell the particle's center resides in, and search for potential contacts over the central cell and the 26 neighboring cells (in a three dimensional space).

   Performance of the algorithm degrades when particles in the simulated system are not of similar size.

2. ***Bounding Box Algorithm.***

   This search algorithm is an extension of the Algorithm 1. However, the cell size is based on the diameter of the smallest particles, rather than the largest particles. Therefore, for systems in which particle sizes are nonuniform, performance is not degraded as it would be in the basic search algorithm [97].

   Bounding Box Search Algorithm.

   Step 1. Discretize the simulation space into cells of equal size.

   Step 2. Identify all cells which any part of a target particle may occupy.

   - Locate the particle center.
   - Add and subtract the particle radius to determine the maximum and minimum bounds, respectively, in all dimensions.

   Step 3. List the target particle as present in those cells identified in Step 2.

   Step 4. Search for potential contacts over the same set of cells (the "bounding box") obtained in Step 2.

B.2 Fine Contact Detection

The *fine* search is performed to find which pairs of particles, identified in the previous stage, are actually in contact and to determine the degree of contact, i.e. the distance of penetration or closure. The algorithm loops over each pair of particles listed in the coarse search stage and proceeds according to the types of particles participating in the contact.

Fine Contact Algorithm.

Step 1. Identify the contact case for each pair of particles identified in the coarse search stage. The polyhedra particles (grains) considered in this research are clusters composed of three primitive particles: Facet, Sphere, and Cylinder, as shown in Figure **??**.

Therefore there are five contact cases, but only four are consider here:

- Sphere - Sphere
- Sphere - Facet
- Cylinder - Cylinder
- Sphere - Cylinder
- Cylinder - Facet is not geometrically possible.

Step 2. Apply correct contact detection algorithm based on the contact case. The goal is to compute penetration between particles depending on contact case. Formulas to compute penetration for each contact case are provided below:

- **Sphere - Sphere**:
  Compute the distance between the centers of the spheres, D, and compute penetration:

$$penetration = (R_{S1} + R_{S2}) - D$$

  where R_{S1} and R_{S2} are the radii of the two spheres.
- **Sphere - Facet**:
  Compute the distance from the center of the sphere to the plane containing the three nodes of the facet, D. Then compute penetration:

$$penetration = R_S - D$$

  where R_S is the radii of the sphere.

- **Cylinder - Cylinder**
  Compute the closest approach between the two principal axes of the cylinders , D. Then compute penetration:

$$penetration = (R_{C1} + R_{C2}) - D$$

  where R_{C1} and R_{C2} are the radii of the two cylinders.

- **Sphere - Cylinder**
  Compute the distance from the center of the sphere to the principal axis of the cylinder, D. Then compute penetration:

$$penetration = (R_S + R_C) - D$$

  where R_S and R_C are the radii of the sphere and cylinder respectively.

Details on how each case is treated can be found in [45]. Many other algorithms to compute distance between the class types mentioned above can be found online.

Step 3. Depending of the contact type, determine if contact is made. Then, proceed to update contact list.

- For non-bonded contact, if penetration is greater than 0, then contacts is made.
- For bonded contacts, if $D \leq (1+bonding\_distance)(R_A+R_B)$, i.e. $penetration \leq 0$, then contact is made.

APPENDIX C

DEM INPUT FILES

C.1 Initial DEM input files

C.1.1 Biaxial compression to get walls closer to particles

```
UNIAX.SCP
RNEW
9807.00
1.00
1.0
0.002
1.0
1
3.10
1
2
1 1 1
2 1 2
2 2 1
2 2 2
2
5000.0
2.0
2000.0
0.0
```

```
0.0

0.0

0.0

0.0

0.0

0.0

0.0

10000.0

10.0

2000.0

0.0

0.0

0.0

0.0

0.0

0.0

0.0

0.0

139.14

100.10

0.0 5.5 0.0 10.5 0.0 2.5 1.0

44
```

```
0.05000
1 1 2 14 1.0392 0.6000 0.6500 0
1 0.0000 0.5000 -0.5000
2 0.4330 0.2500 -0.5000
3 0.4330 -0.2500 -0.5000
4 0.0000 -0.5000 -0.5000
5 -0.4330 -0.2500 -0.5000
6 -0.4330 0.2500 -0.5000
7 0.0000 0.5000 0.5000
8 0.4330 0.2500 0.5000
9 0.4330 -0.2500 0.5000
10 0.0000 -0.5000 0.5000
11 -0.4330 -0.2500 0.5000
12 -0.4330 0.2500 0.5000
13 0.0000 0.0000 -0.5000
14 0.0000 0.0000 0.5000
24
1 13 2
2 13 3
3 13 4
4 13 5
5 13 6
```

```
6 13 1

1 2 8

1 8 7

2 3 9

2 9 8

3 4 10

3 10 9

4 5 11

4 11 10

5 6 12

5 12 11

6 1 7

6 7 12

7 8 14

8 9 14

9 10 14

10 11 14

11 12 14

12 7 14

2 1 2 14 2.0785 0.6000 0.6500 0

.

.
```

```
.
44 1 2 14 4.1569 9.6000 0.6500 0
1 0.0000 0.5000 -0.5000
2 0.4330 0.2500 -0.5000
3 0.4330 -0.2500 -0.5000
4 0.0000 -0.5000 -0.5000
5 -0.4330 -0.2500 -0.5000
6 -0.4330 0.2500 -0.5000
7 0.0000 0.5000 0.5000
8 0.4330 0.2500 0.5000
9 0.4330 -0.2500 0.5000
10 0.0000 -0.5000 0.5000
11 -0.4330 -0.2500 0.5000
12 -0.4330 0.2500 0.5000
13 0.0000 0.0000 -0.5000
14 0.0000 0.0000 0.5000
24
1 13 2
2 13 3
3 13 4
4 13 5
5 13 6
```

```
6 13 1

1 2 8

1 8 7

2 3 9

2 9 8

3 4 10

3 10 9

4 5 11

4 11 10

5 6 12

5 12 11

6 1 7

6 7 12

7 8 14

8 9 14

9 10 14

10 11 14

11 12 14

12 7 14

32 0 16 8 0

1 -1.0000 -1.0000 -1.0000

2 -1.0000 11.5000 -1.0000
```

```
3 5.5000 -1.0000 -1.0000

4 5.5000 11.5000 -1.0000

5 5.5000 -1.0000 3.5000

6 -1.0000 -1.0000 3.5000

7 5.5000 -1.0000 -1.0000

8 -1.0000 -1.0000 -1.0000

9 5.5000 11.5000 3.5000

10 -1.0000 11.5000 3.5000

11 5.5000 11.5000 -1.0000

12 -1.0000 11.5000 -1.0000

13 -1.0000 -1.0000 3.5000

14 -1.0000 11.5000 3.5000

15 5.5000 -1.0000 3.5000

16 5.5000 11.5000 3.5000

17 5.5000 -1.0000 -1.0000

18 5.5000 -1.0000 3.5000

19 5.5000 11.5000 3.5000

20 5.5000 11.5000 -1.0000

21 -1.0000 -1.0000 -1.0000

22 -1.0000 -1.0000 3.5000

23 -1.0000 11.5000 3.5000

24 -1.0000 11.5000 -1.0000
```

```
25 -1.1000 12.0000 -1.5000
26 -1.1000 12.0000 4.0000
27 5.4000 12.0000 -1.5000
28 5.4000 12.0000 4.0000
29 -1.1000 -1.5000 -1.5000
30 -1.1000 -1.5000 4.0000
31 5.4000 -1.5000 -1.5000
32 5.4000 -1.5000 4.0000
0
2
1 2 1 2 4
2 2 1 4 3
2
3 2 5 6 8
4 2 5 8 7
2
5 2 9 12 10
6 2 9 11 12
2
7 2 13 16 14
8 2 13 15 16
2
```

```
9 2 17 19 18

10 2 17 20 19

2

11 2 21 22 23

12 2 21 23 24

2

13 2 25 26 28

14 2 25 28 27

2

15 2 32 30 29

16 2 32 29 31

10

0.00 0.00 0.00

0 0 0 2.2500 5.2500 -1.0000

10

0.00 0.00 0.00

0 0 0 2.2500 -1.0000 1.2500

10

0.00 0.00 0.00

0 0 0 2.2500 11.5000 1.2500

10

0.00 0.00 0.00
```

```
0 0 0 2.2500 5.2500 3.5000

10

0.00 0.00 0.00

0 0 0 -1.0000 5.2500 1.2500

10

0.00 0.00 0.00

0 0 0 5.5000 5.2500 1.2500

10

0.00 0.00 0.00

0 0 0 2.7500 12.0000 1.2500

10

0.00 0.00 0.00

0 0 0 2.7500 -1.5000 1.2500

TIME 0.01001 0.000010 0.100

OBJE 1 ON

OBJE 2 ON

OBJE 3 ON

OBJE 4 ON

OBJE 5 ON

OBJE 6 ON

OBJE 7 OFF

OBJE 8 OFF
```

```
OBJV 1 0.00 0.00 +0.00

OBJV 2 0.00 +100.00 0.00

OBJV 3 0.00 −130.00 0.00

OBJV 4 0.00 0.00 −0.00

OBJV 5 −85.00 0.00 0.00

OBJV 6 +100.00 0.00 0.00

GRAV OFF

WBND OFF

WPSN OFF

WROT OFF

WKNE OFF

WSTR OFF

ENDT

ENDF
```

C.1.2 Biaxial compression to get particles in contact

UNIAXR2.SCP

```
RSTR

uniax_rstart.rst_new

TIME 0.008 0.00001 0.1

OBJE 1 ON

OBJE 2 ON
```

```
OBJE 3 ON

OBJE 4 ON

OBJE 5 ON

OBJE 6 ON

OBJE 7 OFF

OBJE 8 OFF

OBJV 1 0.00 0.00 +0.00

OBJV 2 0.00 +25.00 0.00

OBJV 3 0.00 -25.00 0.00

OBJV 4 0.00 0.00 -0.00

OBJV 5 -25.00 0.00 0.00

OBJV 6 +25.00 0.00 0.00

GRAV OFF

WBND OFF

WPSN OFF

WROT OFF

WKNE OFF

WSTR OFF

ENDT

ENDF
```

C.2 Bond Initialization input file

UNIAXR3.SCP

```
RSTR

uniaxr2_rstart.rst_new

TIME 0.0001 0.0001 0.1

OBJE 1 ON

OBJE 2 ON

OBJE 3 ON

OBJE 4 ON

OBJE 5 ON

OBJE 6 ON

OBJE 7 OFF

OBJE 8 OFF

OBJV 1 0.00 0.00 +0.00

OBJV 2 0.00 +00.00 0.00

OBJV 3 0.00 -00.00 0.00

OBJV 4 0.00 0.00 -0.00

OBJV 5 -00.00 0.00 0.00

OBJV 6 +00.00 0.00 0.00

BDON

GRAV OFF

WBND OFF
```

```
WPSN OFF

WROT OFF

WKNE OFF

WSTR OFF

ENDT

ENDF
```

C.3 Uniaxial compression input file

UNIAXR4.SCP

```
RSTR

uniaxr3_rstart.rst_new

TIME 0.0050 0.00001 0.1

OBJE 1 OFF

OBJE 2 ON

OBJE 3 ON

OBJE 4 OFF

OBJE 5 OFF

OBJE 6 OFF

OBJE 7 OFF

OBJE 8 OFF

OBJV 2 0.00 +0.001 +0.00

OBJV 3 0.00 -0.001 +0.00
```

```
GRAV OFF

WBND OFF

WPSN OFF

WROT OFF

WKNE OFF

WSTR OFF

ENDT

ENDF
```